FLORIDA INTERNATIONAL UNIVERSITY

Miami, Florida

MILLIMETER WAVE IMAGING CAMERA SYSTEM IN OPTICAL DOMAIN

A dissertation submitted in partial fulfillment of

the requirements for the degree of

DOCTOR OF PHILOSOPHY

in

ELECTRICAL & COMPUTER ENGINEERING

by

Abe Akhiyat

2023

To: Dean John L. Volakis
College of Engineering and Computing

This dissertation, written by Abe Akhiyat, and entitled Millimeter Wave Imaging Camera System in Optical Domain, having been approved in respect to style and intellectual content, is referred to you for judgment.

We have read this dissertation and recommend that it be approved.

_____
Elias Alwan

_____
Andres Tremante

_____
Nezih Pala, Co-Major Professor

_____
John Volakis, Co-Major Professor

Date of Defense: March 24, 2023

The dissertation of Abe Akhiyat is approved.

_____
Dean John L. Volakis
College of Engineering and Computing

_____
Andrés G. Gil
Vice President for Research and Economic Development
and Dean of the University Graduate School

Florida International University, 2023

ABSTRACT OF THE DISSERTATION

MILLIMETER WAVE IMAGING CAMERA SYSTEM IN OPTICAL DOMAIN

by

Abe Akhiyat

Florida International University, 2023

Miami, Florida

Professor John Volakis, Co-Major Professor

Professor Nezih Pala, Co-Major Professor

The scientific objective of this dissertation is to develop and advance a passive millimeter wave imaging system that has high-sensitivity to detect natural mm-wave radiation emissions at 94 GHz. Due to the unique capability of millimeter-wave radiation to penetrate atmospheric obscuration such as dust, fog, rain, as well as thin dielectrics, passive millimeter-wave imaging has a wealth of potential applications that have long been recognized. However, although millimeter-wave imaging systems have evolved and improved, they have not lived up to their potential, primarily due to limitations in sensor sensitivity, resolution, cost, and size.

The goal of this interdisciplinary dissertation research is to introduce a novel passive millimeter wave imaging system that operates at 94 GHz, viz. at the low atmospheric absorption window. The proposed system makes use of an optical up conversion process that encodes the naturally emitted black body radiation onto an optical beam for imaging using standard NIR camera. We developed a unique design of a photonic integrated chip in the form of antenna integrated electro-optic modulator. The focus of this dissertation is mainly on the front-end of the system that dictates the overall performance. The back end is based on existing commercial off-the shelf imaging optics components.

The main components of an electro-optical modulator are sensing elements such as an antenna or electrodes, the active optical region, and the passive signal medium, viz the optical waveguide/fiber. Our design is an on-chip antenna integrated modulator that is ultra-sensitive and can readily accommodate interferometric passive millimeter wave imaging, where the sensing element is a millimeter wave antenna. For this purpose, we propose a unique design architecture and its associated microfabrication process using standard UV lithography. This unique design integrates a planar antenna directly onto the electro-optic modulator that promotes efficiency and compactness.

The developed millimeter imaging system has improved sensitivity and spatial resolution while concurrently eliminating bulky millimeter wave lenses, normally used in "all electronic" traditional systems. The received millimeter signals from the interferometric sparse array are coded on an optical beam that is subsequently imaged using standard near-infrared lenses and electronics.

TABLE OF CONTENTS

LIST OF TABLES

LIST OF FIGURES

FIGURE PAGE

ABBREVIATIONS AND ACRONYMS

AL	Aluminum
ATR	Attenuated total reflection
Au	Gold
AWG	Arrayed waveguide grating
BB	Black Body
BB	Black Body
EM	Electromagnetic
EM	Electromagnetic
EMI	Electromagnetic interference
EMI	Electromagnetic interference
EO	Electro-optic

EOM	Electro-optic modulator
EOM	Electro-optic modulator
FOM	Figure of merit
FOM	Figure of merit
FPA	Focal plane array
FPA	Focal plane array
FPR	Free propagation region
FT	Fourier Transform
IC	Integrated Circuit
IC	Integrated Circuit
ICP-RIE	Inductively Coupled Plasma reactive ion etching
LNA	Low Noise Amplifier

LNA	Low Noise Amplifier
mm-Wave	Millimeter wave
NEP	Noise Equivalent Power
NEP	Noise equivalent power
NEP	Noise Equivalent Power
NETD	Noise Equivalent Temperature Difference
NETD	Noise equivalent temperature difference
NETD	Noise Equivalent Temperature Difference
NIR	Near infra-red
PD	Photodiode
PIC	Photonic integrated circuit
PMMW	Passive millimeter wave

PMMW	Passive millimeter wave
ROIC	Read out circuit
SWAP	Size, weight, and power
SWAP	Size, weight, and power

CHAPTER 1

INTRODUCTION

1.1 BACKGROUND

Millimeter-wave (mm-Wave) imaging is an enabling technology for imaging and mm-wave radiation detection in degraded visual environments. The large range of applications for this technology include astronomy, medical and environmental diagnostics; aerial reconnaissance, stand-off threat detection, portal screening, persistent surveillance, situational awareness, video imaging navigation in the absence of GPS signals, scientific research, medical field, and environment study to list a few. Millimeter wave radiation occupies the electromagnetic spectrum between the microwave and Terahertz (THz) frequencies. As a result, mm-Wave imaging is uniquely positioned for both high resolution and the ability to see through many particle concentrations, such as smoke, fog, sandstorms, and clouds, providing pilots with valuable situational awareness during hover, takeoff, and landing operations. Furthermore, mm-Wave radiation penetrates thin dielectric materials including plastic and clothing and is strongly reflected by metallic materials. All these properties make mm-Wave imaging an invaluable technology for a wide range of imaging and detection applications.

Other applications for passive mm-Wave imaging (PMMW) camera, since it has the capability to “see” through obscurants and reveal hidden objects, it can be used as a complimentary sensing in the emerging field of multi-sensor data fusion. As such, data fusion of multiple sensors, such as visible camera, IR cameras, LADAR (Laser Radar), and RFIDs (illustrated in Figure 1-1) to be combined with the mm-Wave images to achieve

inferences not normally obtained from a single modality. Indeed, reduction of visibility is a hindrance in many applications, including automated guidance and nighttime operations. Conversely, radio frequency/mm-Wave imaging is largely immune to obscurants. As can be expected, a compact high sensitivity passive mm-Wave camera can serve critical needs for guidance of various mobile platforms, assist pilots and UAVs in hovering, landing, and takeoff, and where most sophisticated infrared cameras fail.

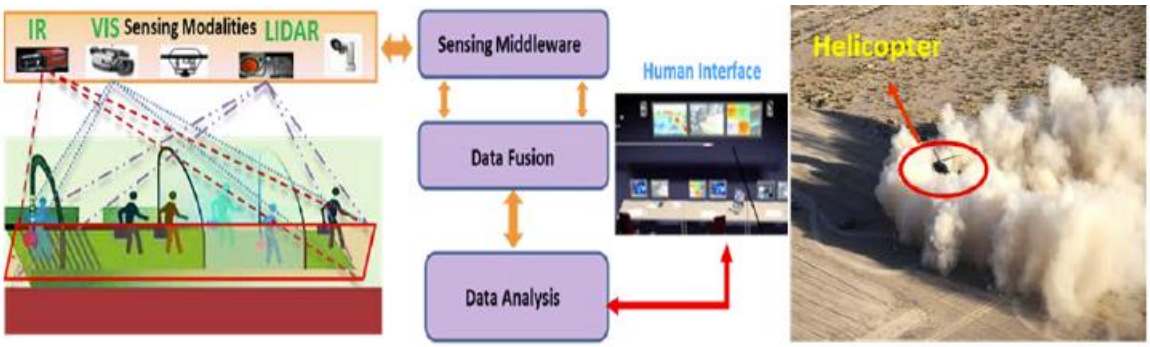

Figure 1-1. Conceptual multimodalities sensing for screening and surveillance (right). Helicopter brownout landing (left)

Millimeter-wave imaging systems are broadly classified as either passive or active. Active imaging sensors require a source to illuminate the interrogated scene, and the image is constructed by measuring phase and amplitude of the illumination reflected electromagnetic wave. On the other hand, passive imaging systems do not require an illuminating source. Rather, they detect Black Body (BB) radiation emitted by the target itself. Two typical types of these detection systems are shown in figure 1-1. These systems were first known as radiometers, their first use was in the field of astronomy as radio receivers (operating at microwave frequencies) to measure the average power of noise coming from radio telescopes. Although passive and active imaging systems have many

blocks and concepts in common, PMMW detection is most sought after at mm-Wave frequencies due to reduction in hardware requirements, power, and ease of deployment.

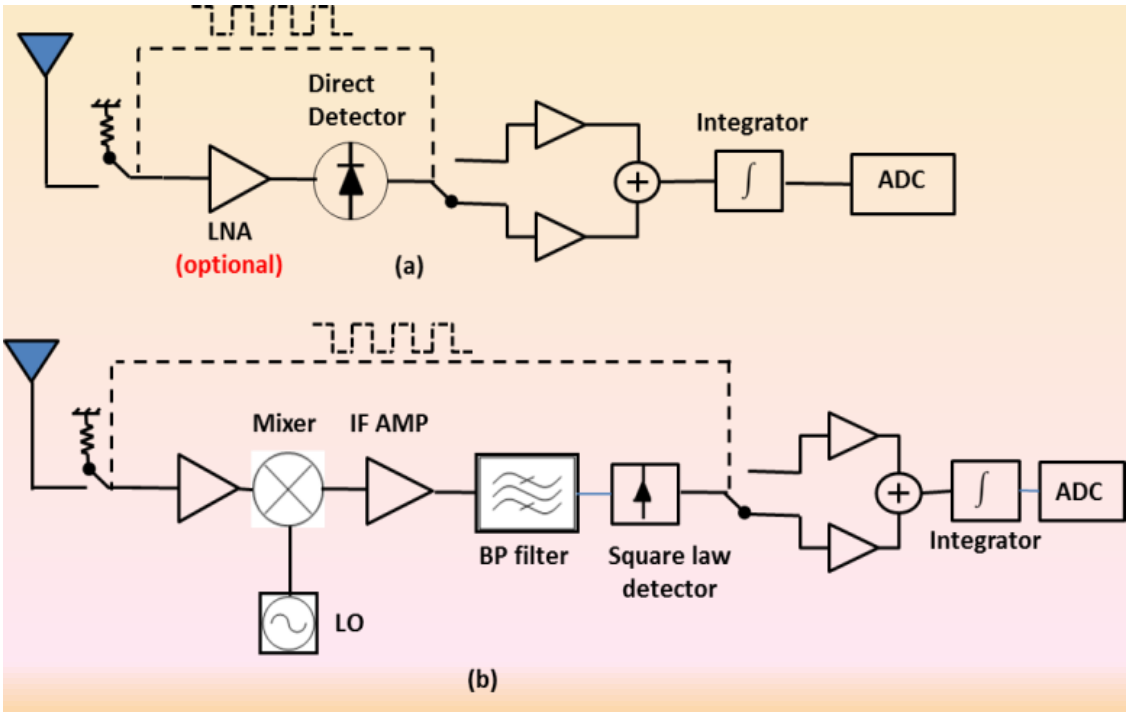

Figure 1-2. All electronic radiometric detector used in mm-Wave Passive Millimeter Wave Imaging System. For direct detection (a) and indirect detection (b).

In the realm of mm-Wave imaging and detection, active systems make use of active an illuminating radiation source, usually of predetermined high-power mm-wave radiation and frequency spectrum. With the advances of electronic IC in the mm-Wave regime such as low noise amplifiers, oscillator, and power amplifiers, mixers and multipliers, etc. Active imaging systems at mm-wave are strait forward, although not without challenges in terms of cost and performance. Passive mm-Wave imaging on the other hand operates without an active source as the imaging of the scene scheme depends on the detection of the blackbody radiation emitted by all terrestrial objects. Although passive mm-wave imaging systems do away with active sources to better performance in many aspects, they put stringent

requirement on the detector sensitivity such as the detection systems depicted in figure 1-2. This is mainly due to the availability and strength of BB radiation (BB detectors are sometimes referred to as radiometers).

BB radiation or thermal electromagnetic radiation are emitted by all objects whose temperatures are above absolute zero. The amount of radiated energy is maximum at mid-infrared region (~10-micron) and rapidly decreases at a longer wavelength as depicted in figure 1-3. This figure also describes the enabling phenomenology for detection in terms radiance and spectral exitance.

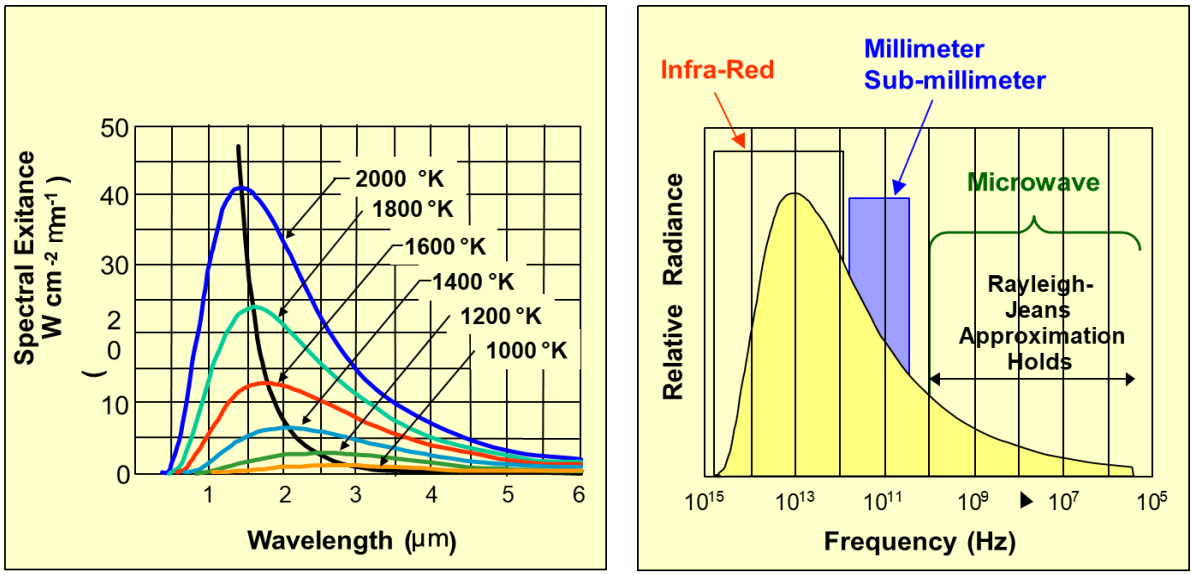

Figure 1-3. Black Body radiation spectral. Spectral exitance (a); relative radiance across frequency spectrum (b).

As noted earlier, all objects above absolute zero radiate energy. This constitutes the underlying principle behind passive millimeter wave imaging (PMMW) imaging or radiometric imaging (Objects emissivity and brightness (temperature)). There are two

extreme cases: one which is a perfect radiator that has emissivity equal to one, also refer to as a perfect radiator or BB. And the other that has emissivity of zero or a perfect absorber. The value of emissivity of an object is a function of its dielectric constant and its surface roughness. The radiometric temperature of an object is defined as its emissivity times its thermodynamic temperature. It is the variation in object radiometric emissivity in a given scene that makes radiometric imaging possible. In simple terms, this variation of objects temperature variation of object's temperature within the scene that is measured and mapped to form an image. However, objects will also have associated reflectivity and the corresponding radiometric temperature will be a function of reflectivity as well. Highly reflective objects will have the temperature of that it is reflecting. This leads to an effective radiometric temperature defined as:

$$T_E = T_S + T_{SC} \tag{1.1}$$

Where T_E and T_{SC} are the Radiometric temperature time its emissivity and scattered Radiometric temperature respectively. T_S of an object is defined as:

$$T_S = \varepsilon T \tag{1.2}$$

Figure 1-4 summarizes all radiometric signals arriving at the antenna and table 1-1 lists [1] lists examples material emissivity for three different frequencies 44, 94 and 140 GHz.

When imaging at mm-wave, the choice of frequency of operation is paramount due to the attenuation occurring in atmospheric medium during propagation. A well-known attenuation curve is depicted in Figure 1-5 [2] that spans from 0.3 μm to 3 cm in wavelength.

The atmospheric attenuation level is critical when deciding on the design frequency. In the mm-Wace regime (30-300 GHz) low attenuation frequency windows are limited to a

handful useful bands, namely 35, 94, 135 and 220 GHz. This is mainly due to the resonant absorption of the atmosphere constituents as water vapor and oxygen.

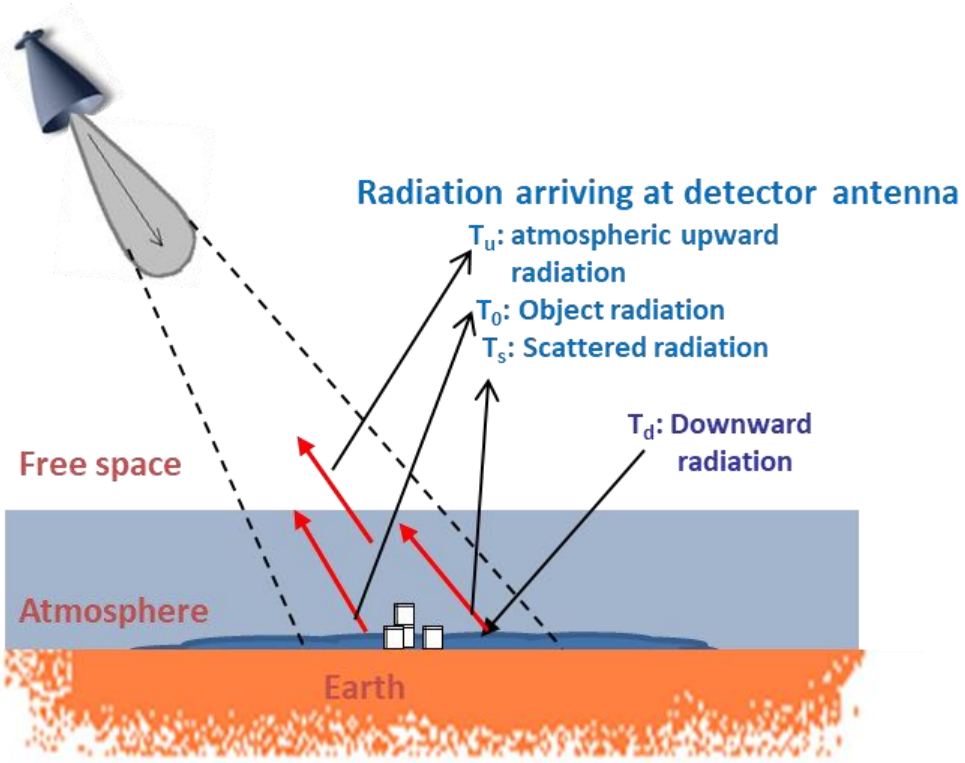

Figure 1-4. Radiation arriving at the antenna from terrestrial objects [2].

As can be noticed from in figure 1-4 very little attenuation takes effect and can propagate for very long distance, however in the presence of fog and rain it drastically attenuates to un undetectable level making the infra-red band unusable for imaging in contrast to the above mentioned low atmospheric attenuation frequency windows mentioned above.

Although the peak emission of Black Body radiation occurs around 10 μm, that is orders of magnitude higher that emission available at mm-Wave, at mm-Wave much more effective (lower attenuation) than infrared in poor weather conditions such as fog, clouds,

snow, dust-storms and rain. Also, images produced by passive millimeter-waves have natural manifestations. And current millimeter-wave receivers have at least 10^5 times better noise performance than infrared detectors and better temperature contrast.

Table 1-1. Effective Emissivity of common materials

	Effective Emissivity		
Surface	**44 GHz**	**94 GHz**	**140 GHz**
Bare metal	0.01	0.04	0.06
Painted metal	0.03	0.10	0.12
Painted metal under canvas	0.18	0.24	0.30
Painted metal under camouflage	0.22	0.39	0.46
Dry gravel	0.88	0.92	0.96
Dry asphalt	0.89	0.91	0.94
Dry concrete	0.86	0.91	0.95
Smooth water	0.47	0.59	0.66
Rough or hard-packed dirt	1.00	1.00	1.00

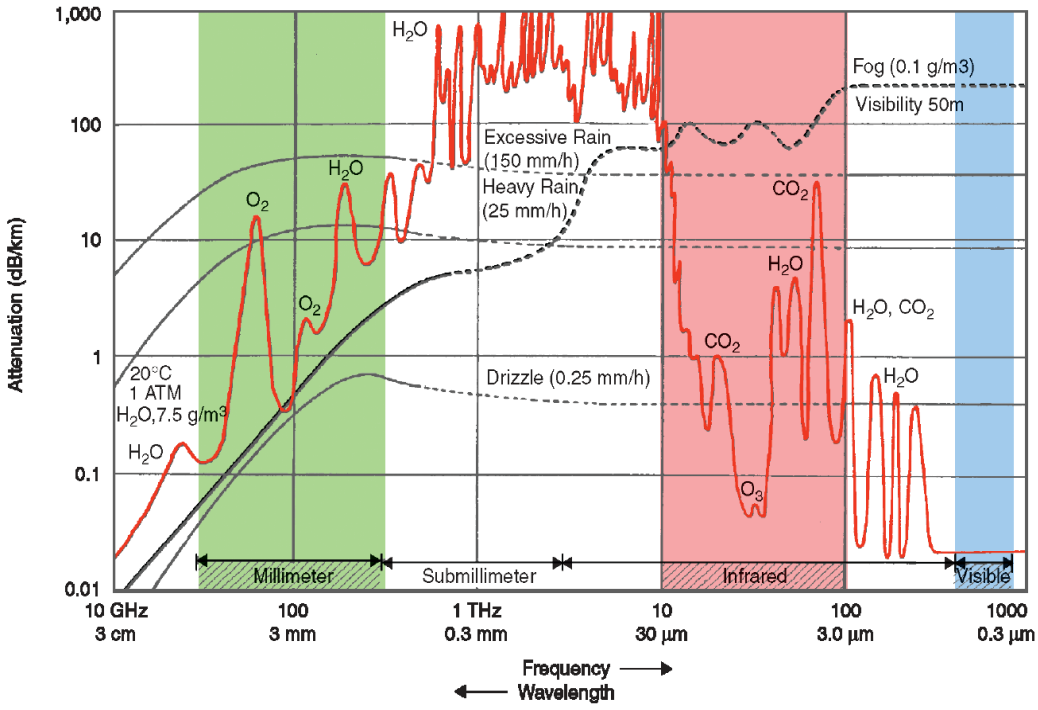

Figure 1-5. Atmospheric attenuation and attenuation of propagation for different weather conditions over the electromagnetic spectrum [2].

Radiometer receivers are at the heart of the mm-wave imaging systems. They measure the thermal electromagnetic radiation and discern it from the background withing the imaged scenery. This is accomplished by detecting the temperature gradient. For passive imaging purposes, due to low radiometric power (pico-watts level). Stringent requirements are put on the receiver performing radiation detection. The radiometric receiver chain is therefore required to have an optimum 100 dB gain or more to be viable. Additionally, to differentiate small temperature difference withing a given imaged scene, radiometric receivers are required to have high sensitivity and low noise.

In Essence radiometric receivers are similar in their architecture to the common electronic receivers used in communication receiver systems and have circuit components such as low noise amplifiers (LNA), Oscillator, mixer, switch, filter, etc. (see Figure 1-1). Proven radiometric receivers for PMMW imaging systems utilize direct detection or heterodyne architecture. They are however limited, especially at higher frequencies, by the cost and the available technology of the integrated circuit (IC) performance to achieve ultra-low noise (needed for high sensitivity radiometric detectors), although achieving high gain is no longer an issue due to the advances in IC technology utilizing III-V semiconductor materials. Both heterodyne and direct radiometric receivers have been demonstrated and deployed in the realm of passive millimeter wave imaging systems in a single frame using focal Plane arrays (FPA) and/or mechanically rotating scanners and phase array beam formers [3]. Examples of images taken using mm-wave imaging systems are shown in figures (5-7).

1.1 MOTIVATION

Millimetre wave imaging systems, to date have not lived up to the long-standing expectation. Those in the field are “all-electronic.” To date, the higher cost and large size of existing systems makes pixel array designs cumbersome and prohibitive for most applications. This research will enable and advance passive millimeter imaging systems in areas where improvement is needed the most. Substantial sensitivity improvement is predicted though adaptation of optical up-conversion scheme, choice of high optic effect EO polymer material as the modulating medium, and low loss polymer passive optical waveguide and better fiber coupling efficiency. A new Integrate Photonic Circuit (PIC) devices that can integrate a millimeter wave antenna and perform an optical modulation has the potential not only drastically contribute to reduction in size, but also tremendous potential in increase in sensitivity performance. In essence mm-Waver wave imaging system adapted to operate in the optical regime has the potential to be designed for high sensitivity, at lower cost and considerable reduction in size. When a breakthrough in sensitivity is reached, these imaging systems will be more practical and will find their way into a whole host of new applications because of added features otherwise not available or possible in all electronic RF based systems. Some of these added features attributed the optical approach are: Higher bandwidth capability which critical for radiation detection and system sensitivity, immunity to electromagnetic interference, it can leverage existing EO technologies, capabilities such as stand-off focal plane array systems in compact formats, beam forming and/or steering can readily be applied to millimeter wave imaging pixel array, it will enable an ideal platform for distributed or synthetic apertures imaging systems

where signals from a fiber bundle can be collimated using lenses and projected to a near-infrared .

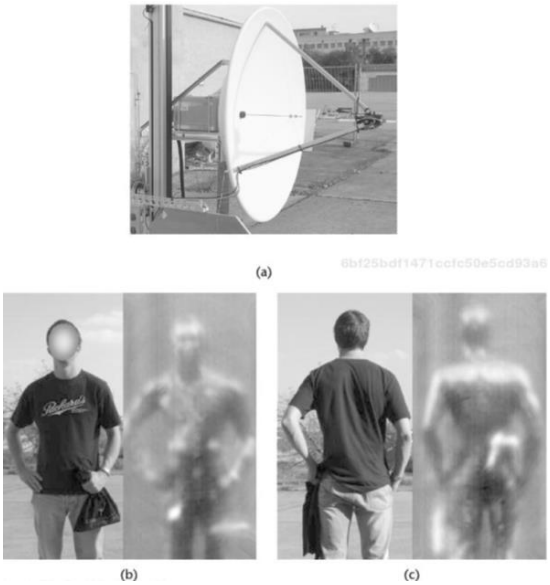

Figure 1-6. (a) 90GHz Radiometric imaging system using a Cassegrain antenna system with a rotating sub-reflector. (b) and (c) radiometer images of a carrying various optically non-visible objects under its clothing. [4].

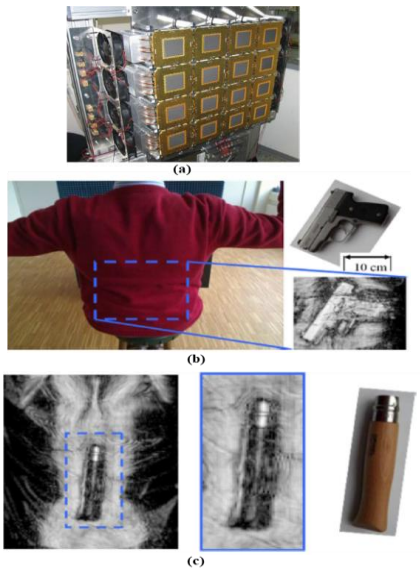

Figure 1-7. (a) Fully electronic imaging system with 736 Tx and 736 Rx antennas operating from 72 to 80 GHz. (a) Array of 16 clusters. (b) Image of a person concealing a small pistol (c) Image of a person concealing a knife. [5].

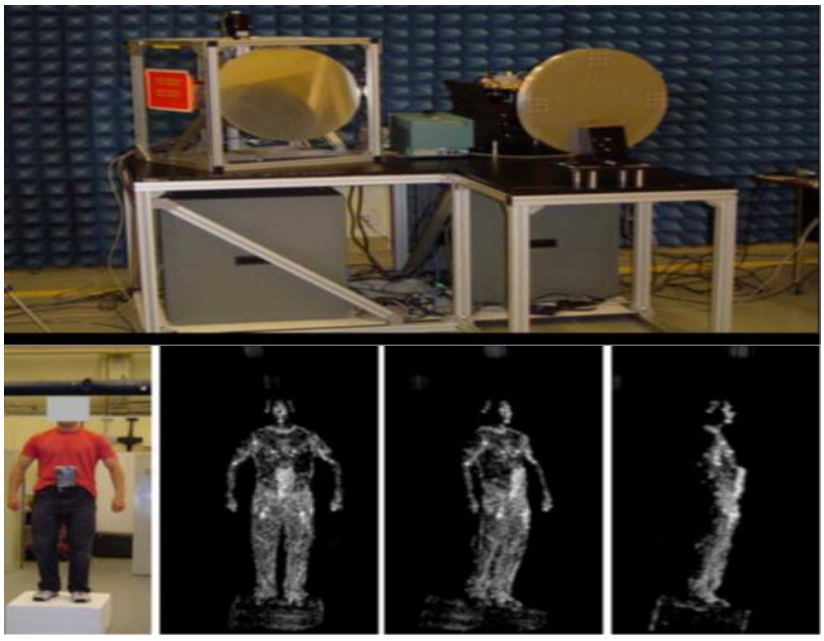

Figure 1-8. (Top) Radiometric prototype standoff imaging system (bottom) resulting images [6].

CHAPTER 2

PMMW IMAGING USING OPTICAL UP-CONVERSION

2.1 INTRODUCTION

mm-Wave imaging as an enabling technology for imaging and detection in degraded visual environments. And other range of applications for this technology that such as the field of astronomy, aerial reconnaissance, stand-off for threat detection, portal screening, persistent surveillance, situational awareness, video imaging navigation in the absence of GPS signals, scientific research, medical field, and environment study to list a few.

Millimeter wave radiation occupies the electromagnetic spectrum between the microwave and Terahertz *(THz)* frequencies. As a result, mm-wave imaging is uniquely positioned for both high resolution and the ability to see through many particle concentrations, such as smoke, fog, sandstorms, and clouds, providing pilots with valuable situational awareness during hover, takeoff, and landing operations. Furthermore, mm-wave radiation penetrates thin dielectric materials including plastic and clothing and is strongly reflected by metallic materials. All these properties make mm-wave imaging an invaluable technology for a wide range of imaging applications.

Due to the tremendous potential applications mentioned above, PMMW imaging systems operating at millimeter-wave were first investigated a few decades ago [7-9], and they are still evolving along with the advances in semiconductor integrated circuit (IC) technology. These imaging systems capture naturally emitted thermal radiation from objects in the scene and its surroundings. Blackbody radiation is emitted at almost constant power density (from all objects) that is proportional to the temperature and emissivity of radiating

object (Rayleigh Law). At high frequencies, these radiations are severely attenuated by oxygen and water vapor in the air; however, in the millimeter-wave range there exist low atmospheric attenuation windows at of 35, 94, 140 and 220 GHz as shown in figure 1-5. The choice of frequency band for mm-wave imagers is application-specific, available supporting technology and imaging scheme employed.

PMMW imaging systems detect millimeter-wave radiation emitted from a scene incident on a receiver's antenna. It records the relative intensity at each pixel from which an image is constructed. The underlying concept is not new; in fact, astronomers have been using microwave receptors to detect faint stars lightyears of distance away. To date, fielded millimeter wave imaging systems and radiometers, whether they are direct or in direct (superheterodyne) as depicted in figure 1-1, are "all -electronic" and most of their front-end circuit components are required to operate at the frequency of detection (30 to 300 GHz). A great deal of research has been done in this regard [10-13].

Passive imaging systems have been built to be used for a variety of applications. Metal screening at the airport is one of the most encountered examples. The choice of frequency range for a passive millimeter wave imaging system is application specific, these mm-wave imaging camera systems are cost, and form factor driven.

However, the higher the design frequency range the larger the available radiation flux, bandwidth, and the favorable scaling of antenna size, the more complex and expensive these systems quickly become. Nevertheless, because of the diffraction limit, the higher frequency of operation the better will be the resolution for a given aperture size.

Although all electronic approach design to PMMW imaging system designs have produced well-functioning systems, on many fronts, they have not lived up to expectations and potential in terms of sensitivity performance, cost and size. Applications that require high sensitivity and high speed tend to be extremely complex with a substantial increase in cost and size. Most current systems are a single pixel detector that makes use mechanical scanning that slows down images acquisition speed, and large focusing lens in the front-end that increases the form factor. And the large pixel count exacerbates the form factor issue further and does complicates and increases cost of the imaging system electronics and mechanical hardware.

The complexity of these imaging systems and their size are currently the limiting factor for many applications. These constraints have led the research community to consider other approaches, one such approach is the implementation of optical up-conversion in the imaging system front-end. The potential benefits are versatility, performance and reduction in complexity, cost, and size [14-19]. A representative block diagram of a PMMW imaging single pixel using optical up conversion is shown in Figure 2-1. Its functionality is somewhat identical to the architecture used in all RF systems with the distinction that the radiated signals received by the antenna are up converted and processed in the optical domain.

Upconverting the detected mm-wave radiation to an optical frequency makes an array of radiometric detectors compact and less cumbersome. For each detector of the array, BB radiation seen by the corresponding antenna modulates an optical signal source such as a laser operating at one of the communication frequencies or Near-Infrared (NIR). For the case where a phase modulation is used, the output of the modulator has the original optical signal source and sidebands at antenna resonant frequency away from optical source

frequency. After modulation, a bandpass filter is used to single out one of the first side-band antenna encrypted received mm-wave BB radiation. This first sideband is then transmitted via an optical waveguide or fiber to a low noise and high-quality photo-detector photo detector, where its relative intensity is measured. Figure 2-1. Illustrates a functional block diagram and frequency domain signal representation along the different stages of signal path. For such PMMW imaging system the theoretical temperature detection resolution limit is 20 milli-Kelvins.

2.2 MILLIMETER WAVE OPTICAL UP-CONVERSION SCHEME

PMMW imaging employing optical up-conversion scheme and using high performance optical devices, coupled with high level of integration, can now take advantage of the mature enough optical technology and advances in EO material device technology. Optical up-conversion has the potential to be a viable option to further advances in

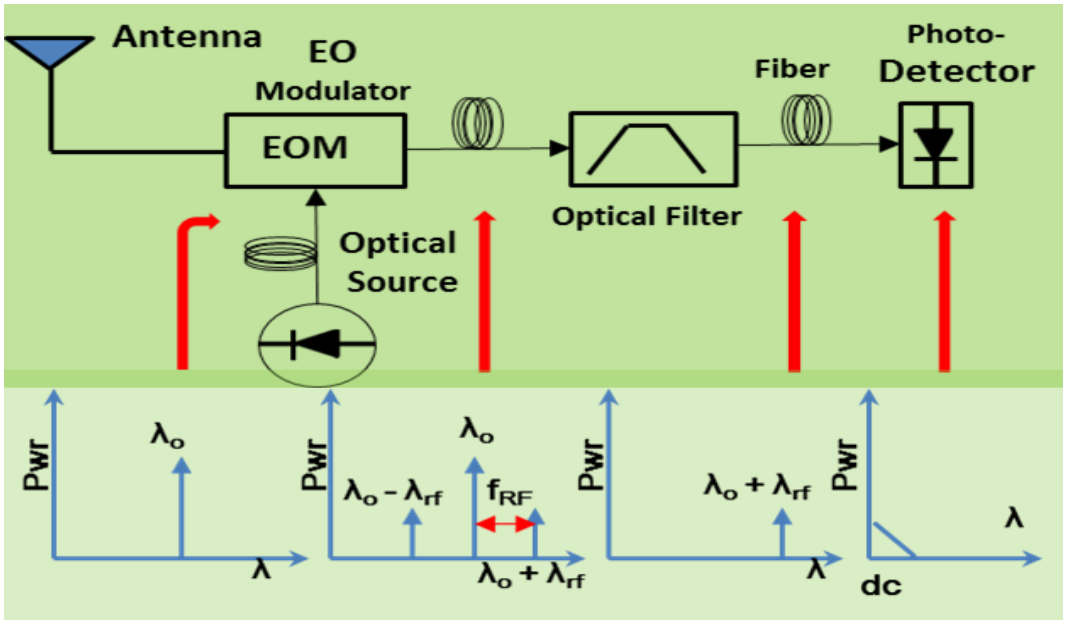

Figure 2-1. Generic single pixel system block diagram for PMW imaging using optical up-conversion.

millimeter-wave imaging system operating way into W-band and terahertz frequencies, and has the potential to produce unprecedented sensitivity performance, lower cost, and considerable reduction in size. Despite the vast array of potential applications, there is very little published work in this regard. A few studies have investigated functionality and viability. These feasibility studies mainly used off-the-shelf discrete components and Lithium Niobate (LiNbO3) as EO material medium. The functionality has been confirmed with promising performance at best. The lack in performance was attributed mainly to unavailability of high efficiency EO modulator operating at millimeter wave at and the discrete nature of front-end system components that substantially affects sensitivity performance of the system.

PMMW imaging system adapted to operate in the optical regime can and has the potential to be designed for high sensitivity, at lower cost and considerable reduction in size. When a breakthrough in sensitivity is reached, these imaging systems will be more practical and will find their way into a whole host of new applications because of added features otherwise not available or possible in all electronic RF based systems. Some of these added features attributed the optical approach are: Higher bandwidth capability which critical for radiation detection and system sensitivity, immunity to electromagnetic interference, it can leverage existing EO technologies, capabilities such as stand-off focal plane array systems in compact formats, beam forming and/or steering can readily be applied to millimeter wave imaging pixel array, it will enable an ideal platform for distributed or synthetic apertures imaging systems where signals from a fiber bundle can be collimated using lenses and projected to a near-infrared camera for image processing.

The sensitivity performance of a PMMW imaging system is expressed in terms of Noise Equivalent Power (NEP). NEP set the noise floor of the system and is required to be extremely low for the system to be able to detect sub-pico-watt power for a reasonable frame rate. NEP and the sensitivity of a passive millimeter wave imaging system are evaluated at the system level. NEP provides the measure of the noise floor of the system, and it is system specific.

PMMW imaging systems using optical up-conversion without amplification have advantages over all electronic systems. For these types of systems, NEP is mainly a function of the photo detector dark current, thermal noise in the system and unsuppressed optical carrier. NEP directly affects the Noise Equivalent Temperature Difference (NETD) which is the overall sensitivity of the system. Noise sources affecting NEP can be mitigated in the system level design. The dark current of the photo detector can be minimized using a proper detector device choice such zero bias detector operating at low speed. Shot noise due to spontaneous emission of a laser source could also be mitigated using proper filtration.

Other factors affecting sensitivity of passive imaging system using optical up-conversion scheme are optical source power, attenuation in the optical link, photo detector responsivity, effective detection bandwidth, and conversion efficiency of the EO modulator. Increasing the electro optical modulator bandwidth and efficiency and minimizing excess loss of the optical link are identified as the most pressing issues needing to be addressed to considerably improve and achieve a breakthrough in sensitivity performance. This proposed research addresses these two main sensitivities limiting factors.

2.3 UPCONVERTING OPTICAL MODULATOR

The demand for optical devices has mainly been driven by the demand for RF over fiber communication system needs. A host of materials and hybrids are being used for discrete and multifunctional optical circuits [20]. However, no single material has all the properties for all purpose applications. Table 2 lists key properties of most used materials.

2.4 OPTICAL MODULATOR MATERIALS

Optical modulators are required in almost all areas of optical technology. The leading high frequency EO modulators in the market are ferro-crystalline based. Currently, the dominant electro optical material is Lithium Niobate ($LiNbO_3$); electro optic modulators made of this crystalline ferroelectric material cover a bandwidth of 10-70 GHz, a V_π of ~5 Volts and an insertion loss that reaches 5 dB at high frequency. Few attempts at pushing performance into higher frequency have produced an unmatched conversion efficiency of 1.04 W^{-1} [21] of its kind, a great stride indeed, but still come short for the required performance needed for implementation into a millimeter wave imaging system relying on optical up conversion. One of the most limiting factors affecting EO modulators performance using $LiNbO_3$ at high frequency is the large difference in refractive index, for which it has values 2.14 and 5.6 at 1550 nm and millimeter wave respectively. This large difference makes velocity match of the two frequency band difficult and hinders modulation efficiency and bandwidth. Adding to this difficulty is the complexity in device processing using $LiNbO_3$ that drives the cost higher.

One alternative to Lithium Niobate that showed a tremendous advantage in terms of electro optical properties that would circumvent Lithium Niobate shortcomings at high

frequencies is to use electro optical polymer material. A great deal of research has been done in this regard in the past 20 years [22-26]. And high performance using off-the-self copolymer have been demonstrated [27]. Polymers as electro optic material owe its gained traction to the following properties: It has a very high electro optical coefficient (r_{33}), that was demonstrated to reach 400 pm/V; its refractive index at optical and millimeter wave are very closely match; it has a fast response time that is less than 10 femtoseconds. Additionally, electro-optical polymers are compatible with a variety of materials allowing easy integration with other optical devices; their low driving voltage has been shown to be significantly less than the driving voltage of Lithium Niobate. Furthermore, as shown in table 2, compared to polymers as optical medium material have additional relevant advantages. Such properties are: Higher modulation frequency, lower propagation and pigtail loss and more closely matched refractive index.

When electromagnetic radiation is upconverted to an optical frequency for imaging or detection purposes, a certain type of electro-optic modulator (EOM) device is involved. These devices when tailored to a specific application, they have following advantages:

- The detection bandwidth can easily be larger than the all-electronic detectors. And limited only by the optical filtration used.
- Depending on the Imaging System configuration, it can decrease the minimum resolvable temperature.
- They are Immune to Electromagnetic Interference (EMI).
- High performing EOM can be used without resorting to an LNA for amplification.
- EOMs have a relatively small form factor and can be integrated at high density for improved resolution.

- Since the up-conversion process scheme preserves the phase, the signal can travel for a verry long distance over fiber with minimal attenuation.

Limited prior work has been accomplished in the field of PMMW imaging system using optical up-conversion [28,29], they all make use of off-the-self commercially available components. They revert to the use of LNA for millimeter wave amplification due to the large loss in and millimeter wave signal link. They demonstrated modest performance but contribute great proof of concept. Figure 2-2 shows an example of a prototype mm-Wave imaging array in a distributed aperture and optical up-conversion.

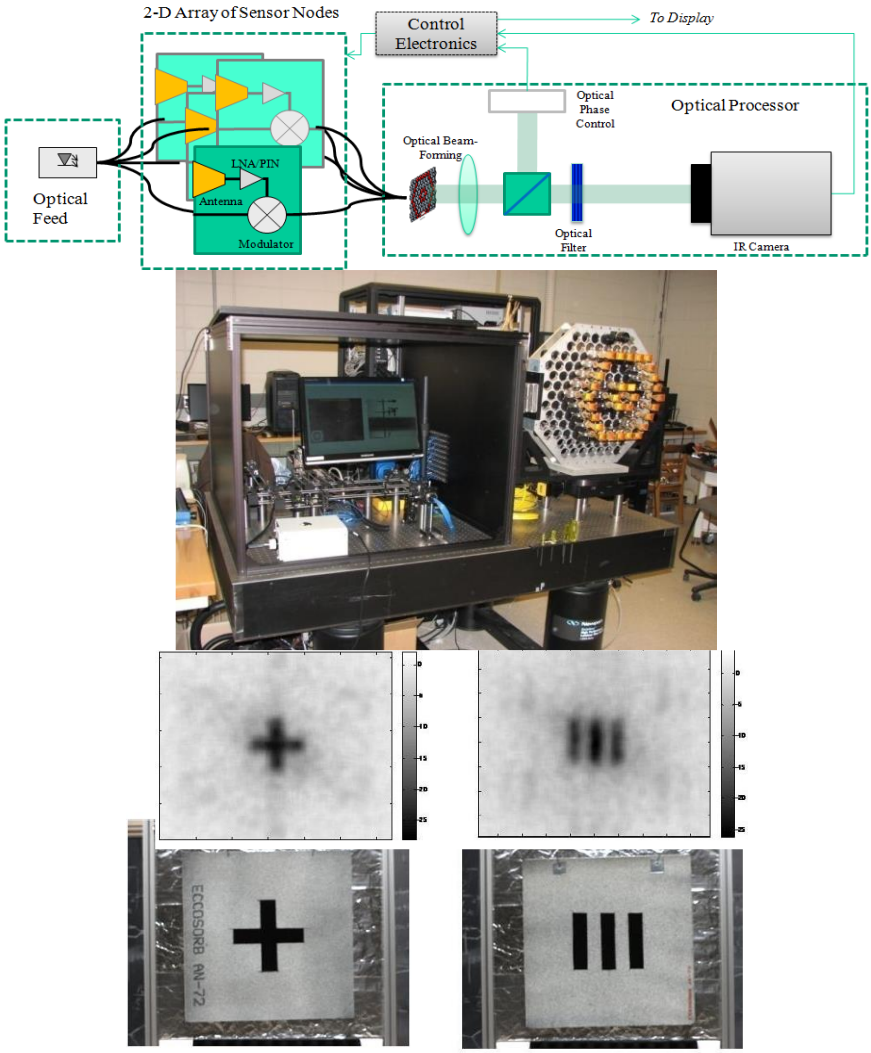

Figure 2-2. Imaging system block diagram (top), prototype (bottom left) Visible and mm-wave imaged (right) [28,29].

Table 2-1. Key Properties of EO materials at 1550 nm

Key Properties of EO materials at 1550 nm							
Material System	Prop. Loss (dB/cm)	Pigtail Loss (dB/chip)	Refractive Index (n)	Index Contrast in Waveguide (Δn)	Birefringence (nTE - nTM)	T/O Coef dn/dT (K^{-1})	Max. Modulation Frequency
Silica [SiO_2]	0.1	0.5	1.5	0 - 4% (Channel)	$10^{-4} – 10^{-2}$	10^{-5}	1 kHz (T/O)
Silicon [Si]	0.1	1.0	3.5	70% [range=0] (SOI)	$10^{-4} – 10^{-2}$	$1.8x10^{-4}$	1 kHz (T/O)
Si Oxynitrid [SiO_xN_y]	0.1	1.0	SiO_2: 1.5 Si_3N_4: 2.0	0 - 30% [30%:Si_3N_4 core]	$5x10^{-6} – 10^{-3}$	10-5	1 kHz (T/O)
Polymers	0.1	0.2	1 .3 - 1.7	0 - 35% (Channel)	$10^{-6} – 10^{-2}$	-1 to $-4x10^{-4}$	>100 GHz (E/O) 1 MHz (T/O)
Lithium Niobate [$LiNbO_3$]	0.5	2.0	2.2	0 - 0.5% (Channel)	$10^{-2} – 10^{-1}$	10^{-5}	40 GHz (E/O)
Indium Phosphide [InP]	3	10	3.1	0-3%	10-3	$0.8x10^{-4}$	40 GHz (E/O)
Gallium Arsenide [GaAs]	0.5	2.0	3.4	0 - 14% [14%:AlAs clad]	10^{-3}	$2.5x10^{-4}$	20 GHz (E/O)
Garnets [e.g. YIG]	0.5	2.0	2.2	0 - 12% [12%:GGG clad]	$10^{-5} – 10^{-4}$	10^{-5}	1 GHz (M/O)

CHAPTER 3

ANTENNA INTEGRATED ELECTRO-OPTIC MODULATOR TO PERFORM OPTICAL UP-CONVERSION DESIGN

3.1 INTRODUCTION

In scenarios where reduction of visibility is a hindrance resulting in reduced movement and an increased possibility of collision and injury, Infrared (IR) imaging is widely used for nighttime operations but suffers in the presence of optical obscurants including smoke, fog, moisture, or dust. Conversely, radio frequency such PMMW imaging, when used in the low attenuation in atmospheric window frequencies, is largely immune to airborne obscurants, as a result of the large wavelength compared to the size of such aerosols. Atmospheric windows in the mm-Wave band represent a compromise between improved resolution and minimal atmospheric attenuation, with popular frequency being 94 GHz.

As mentioned in the introduction, all terrestrial objects at room temperature emit mm-Wave black-body radiation. However, the energy emitted in the millimeter wave spectrum is approximately eight orders of magnitude lower than the energy emitted in the infrared spectrum. For this reason, passive mm-Wave Imaging is only viable if it has high enough sensitivity for a given application. Typical approaches make use of high gain amplifiers which are very noisy, they are difficult to integrate into a compact form and they are expansive. Current state-of-the-art mm-wave imager systems are “all-electronic”, primarily found in the application of body scanning for detection of concealed objects. These imaging systems make use of either a single pixel detector or a small linear array with

a bulky and slow scanning apparatus for image acquisition over a given field of view. These systems suffer from low sensitivity performance at video rate. Alternatively, Focal Plane Array (FPA) imagining systems make use of mm-wave optics to focus radiation into an array of detectors without the need of a scanning apparatus. For a reasonable spatial resolution, sensitivity, and field of view, a large number of pixel detectors are needed, driving up the cost and complexity. Though more compact than electronic systems, they still suffer from low sensitivity performance, diffraction limits, and they have a large form factor due to large required front-end lenses needed to focus incident radiation.

Existing millimeter wave imaging systems have not lived up to expectations, neither in performance nor in achieving manageable size, weight, and power (SWAP). There is still a need for low cost, compact, sensitive, and versatile PMWI systems to enable a broader field of imaging applications. Figure 3-1 shows two distinct (simplified) approaches used for black body radiations detection and PMMW imaging systems. One is all-electronic; the other makes use of optical up-conversion.

The longer-term aim of this research is to enable high-sensitivity, passive imaging system of natural mm-wave emissions, which can be used as standalone or fused with other imaging modality such as conventional IR imagery in degraded environments. This is achieved through a unique antenna integrated electro-optic (EO) modulator, where received mm-wave signals modulate an optical carrier. The optical carrier is then removed using an optical band pass filter, and the remaining sideband is projected onto a commercial off the shelf (COTS) Near-IR camera. A Schematic depiction of envisioned sparse pixel array PMWI system with optical up-conversion and sensing is shown in figure 3-2. The antenna

integrated EO modulator thereby eliminates the need for active RF electronics in the front-end requires only COTS optical source and a photo detector.

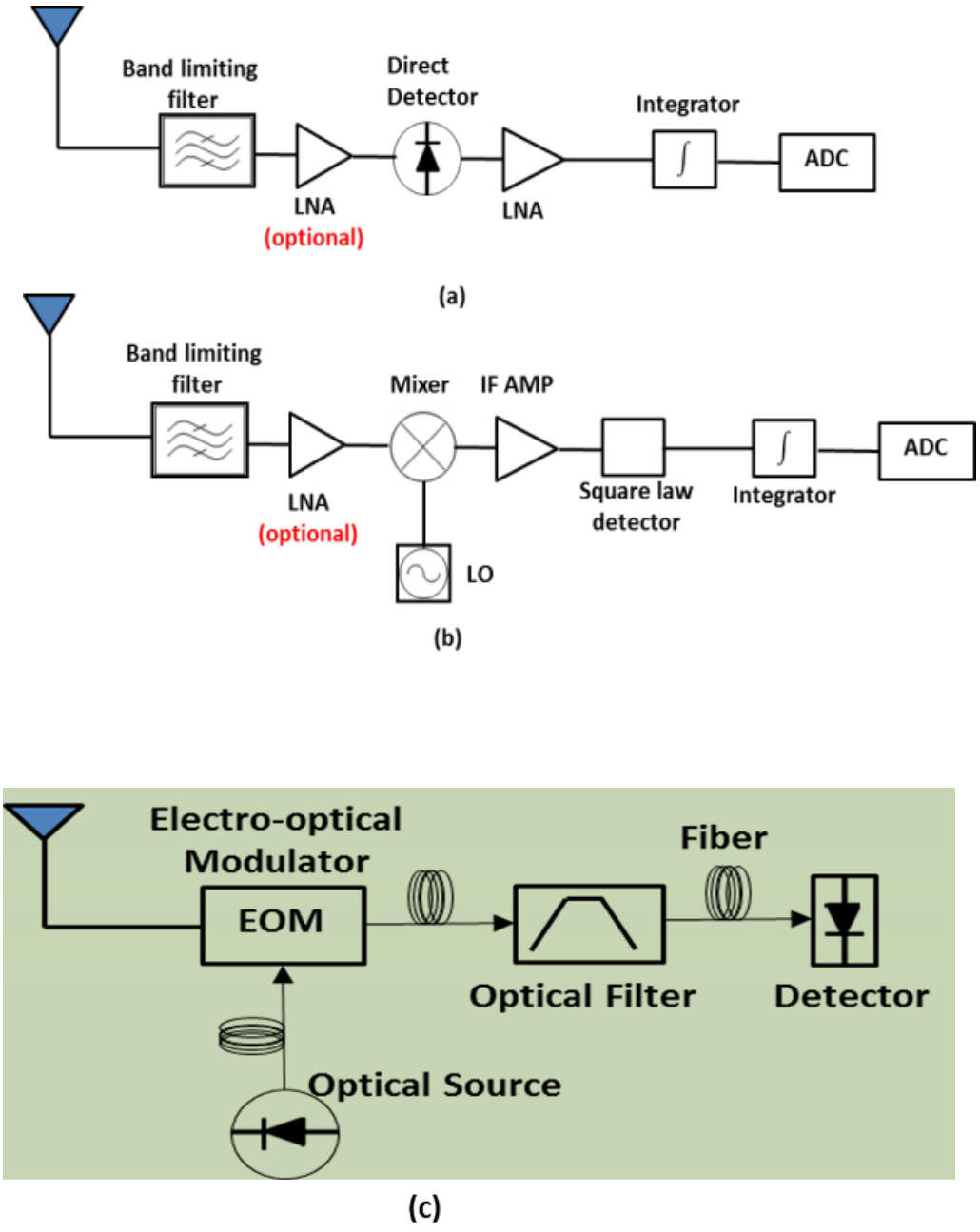

Figure 3-1 Radiometric single unit mm-wave detectors circuit diagrams. (a) direct detector; (b) heterodyne detector; (c) optical upconverting detector.

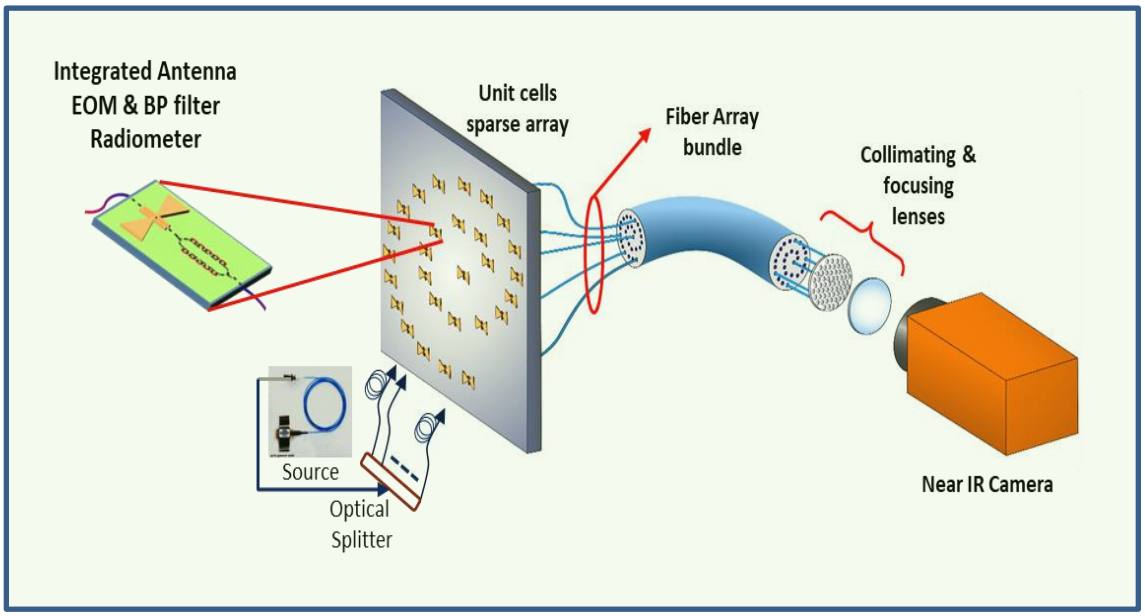

Figure 3-2 Conceptual multimodality sensing for screening and surveillance (right). Helicopter brownout landing

3.2 ELECTRO-OPTIC MODULATOR DESIGN

For PMMW imaging application requiring video rate, high sensitivity and ease in deployment, stringent requirements are put on these systems, whether they are an "all-electronic" imaging system or in when using optical up-conversion for detection scheme. For PMMW imaging application and radiometric detection, the key device component when performing optical up-conversion is the electro-optic modulator. This devise, from a technological point of view is mature and continue to advance to mainly satisfy the telecommunication industry. The leading semiconductor material used is lithium niobate. However, for Applications requiring high-speed and ultra-sensitive optical modulators beyond those most relevant to the telecommunications industry. Which is the case for PMMW imaging applications.

In a physical and form factor point of view, for PMMW imaging, it is desirable to have a planar microfabrication of EOM with antenna integrated within, in such a way received incident signal on the receiving antenna directly modulate an optical carrier. A few immediate benefits are the following:

- Planar antenna can be constructed in a planar format to be facing directly the scenes to be imaged in staring configuration.
- Long traces and/or cox cable are avoided and mitigated the Ohmic loss in the RF link. This is especially important at mm-Wave where Ohmic loss is unavoidable.
- Having the antenna near the no-linear region of the optical waveguide where modulation takes effect improves modulation efficiency due to signal strength
- An array of detectors in the form of full or sparse array configuration can easily be microfabricated and assembled in a compact form factor.

For this research, an on-chip antenna integrated EOM is devised that integrates a planar antenna directly on to the traveling wave EOM. This photonic chip is shown in figure 3-3. The figure shows extruded circuit components for illustration. This comprises passive optical waveguides, active nonlinear optical wave guide and metallic antenna serving as electrodes to the traveling wave electro-optic modulator, claddings, and substrate. This electro-optic modulator could be used standalone as an on-chip antenna integrated electro-optic modulator that can be used as mm-wave radiation detector, or as a building block for a mm-Wave photonic correlation radiometers to be discussed in later a chapter.

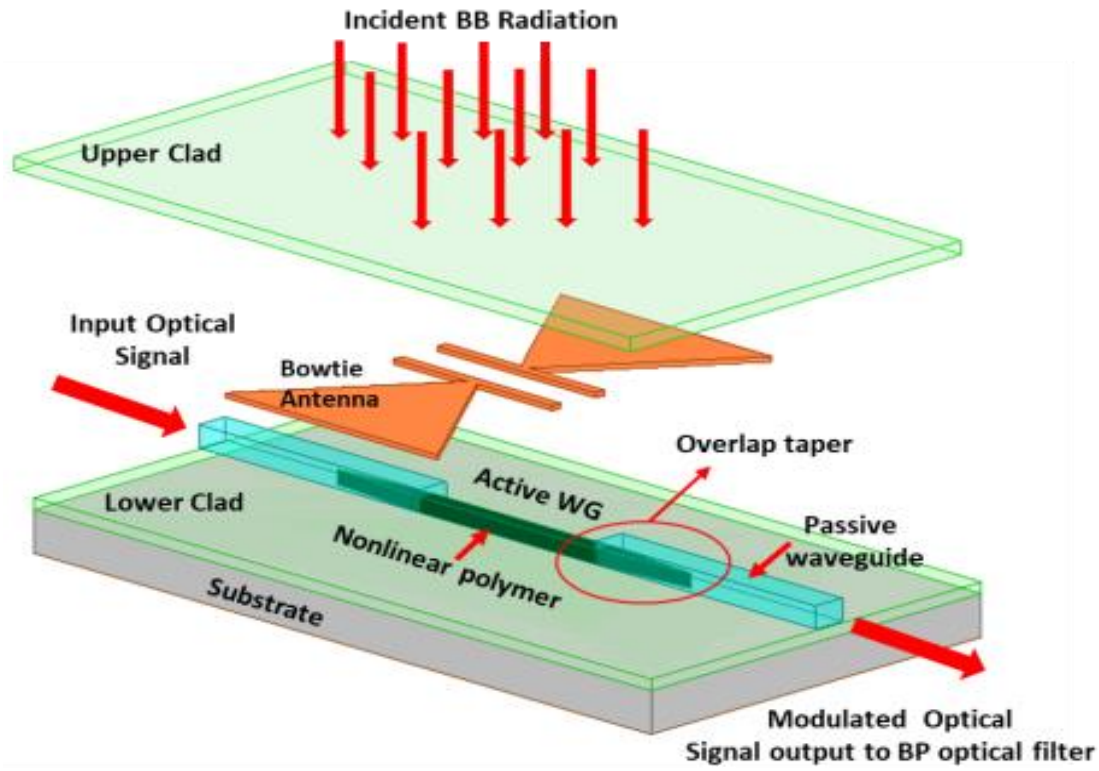

Figure 3-3 Designed antenna integrated Electro-optic modulator for use in an interferometric sparce array configuration passive millimeter wave imaging

3.3 EOM DESIGN ARCHITECTURE

The EOM design is of prime importance for PMWI systems, especially in the passive imaging configuration where application is to be avoided. The sensitivity of these types of passive imaging system is set within the EOM by means of modulation efficiency and amount of signal loss in the optical link as well as RF. Both of these two well-known limiting factors are being addressed in the proposed architecture. Millimeter wave excess loss is addressed by directly incorporating the receiving antenna onto the electro modulator architecture and avoid having to use microstrip trace to route the RF signal where needed.

Several EO modulators using antenna and resonant electrodes were reported [30-34]. They make use of connected fabricated on an EO substrate. These architectures require tunning to match the antenna and the electrodes that provides the modulating RF signal to the active area of the electro-optic modulator. This tunning may not always be optimum, precise, or efficient to obtain an optimum optical modulation. Two promising antenna topologies for this purpose have been investigated, namely a microstrip patch antenna with a slot in the middle and a microstrip bowtie with two extended bars and a gap its apex. Figure 3-4 shows the two antennas used for this work.

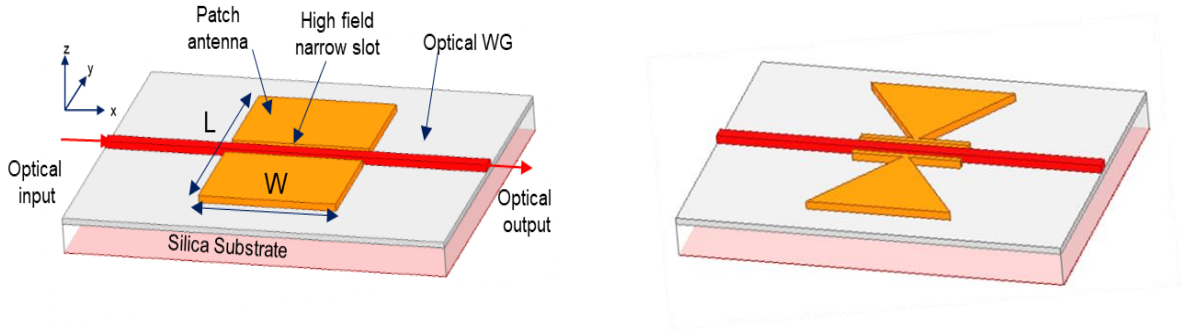

Figure 3-4 Slotted patch antennas used for monolithic integration with EO modulator design. Slotted patch (left). Bowtie with extended bars (right)

3.4 EOM DESIGN PERSPECTIVE

In antenna integrated EOM designs under consideration the antenna with a narrow slot embedded in the middle acts as tow resonant electrodes and provides an electric field responsible for modulating the optical carrier traveling along an optical waveguide embedded within the antenna gap. The optical waveguide withing and along the length of the antenna slot senses the induces electrical field and acts on the nonlinear optical material

and slightly changes it behavior and optical properties. This change is reflected in the refractive index. It is this behavior that produces the desired modulation of the optical signal. The expected outputs of this antenna integrated optical modulator are the optical signal (carrier) and sidebands on both its sides. The detected mm-Wave signal is therefore encoded on these sidebands that can be further processed.

3.4.1 Theoretical perspective and analysis

The proposed antenna integrated electro-optic modulator design lands among EO phase modulators. As mentioned, the underlaying principle behind the modulation is the change of the refractive index properties of the nonlinear optical material medium. The derivation is rigorous and has been established and treated extensively [35]. However, the treatment of the change of the refractive index with respect to applied signal can be simplified to (with respect to space and time) [7]:

$$n(x,t) = n_0 + \delta n(x,t),\ \delta n(x,t) = -\frac{1}{2} n_0^3 r_{33} \Gamma E_{\text{g slot}}(x,t) \tag{3.1}$$

where n_0 is the nonlinear optical material refractive index. and r_{33} is the electro-optic Coefficient (specific to the nonlinear polymer used). Γ is the overlap factor between the incident RF and the optical fields and E_g is the induced electrical field within the gap [36]. Assuming the RF field in the antenna is plane wave in the far field [37] and the antenna polarized in the y direction on the xz plane of incidence. The RF radiation from an external source can be expressed as:

$$E_{RF} = E_{RF}^0 \sin(k_{RF} \sin\theta x - \omega_{RF} t) \tag{3.2}$$

where $k_{RF} = 2\pi/\lambda_{RF}$ and θ is the angle of incidence.

Since the nonlinear material used is a polymer, the optical and RF signal need to be polarized in the direction parallel to the poling field (see figure 3.X).

Invoking the Fresnel transmission coefficient t_{RF} in the TE mode the electric field inside the within the slot in this case the polymer waveguide, to be:

$$E_{RF}^{\text{gap}} = t_{RF} \cdot E_{RF} = \frac{2\cos\,\theta}{\cos\,\theta+\sqrt{\varepsilon_{RF}}\cos\,\theta'} E_{RF}^{0} \sin\,(k_{RF}\sqrt{\varepsilon_{RF}}\sin\,\theta' x - \omega_{RF} t) \quad (3.3)$$

where ε_{RF} is the dielectric permittivity that is equal to (n_{RF}^2) of the polymer and θ' is the angle of incidence inside the polymer layer.

The electric field RF inside the gap that is produced by an incident RF of the antenna is:

$$E_{\text{slot}}\,(x,t) = E_{slot}^{0} \sin\,(k_{RF}\sin\,\theta x - \omega_{RF} t). \quad (3.4)$$

Where $\sqrt{\varepsilon_{RF}}\sin\,\theta' = \sin\,\theta$, from Snell's law.

In the case of a patch antenna, it can be assumed to be an ensemble of half-wave dipoles, the electric field within the gap can [22] to be expressed as:

$$E_{\text{slot}}^{0} = 2 \cdot t_{RF} \cdot E_{RF}^{0} \frac{W_{eff}}{d_{\text{slot}}} \quad (3.5)$$

where W_{eff} and d_{slot} are the effective length of the patch antenna and the gap size of the slot, respectively.

The field enhancement (or enhancement factor) in the slot of the patch antenna can be expressed as:

$$E_{slot}^{0}/E_{RF}^{0} = 2 \cdot t_{RF} \cdot W_{\text{eff}}/d_{\text{slot}} \quad (3.6)$$

When a TE light mode along the waveguide, the nonlinear undergoes a varying refractive index in time and space as $n(x,t)$ given by Eq. (1). The phase difference with respect to the constant refractive index n_0 over a distance dx can be expressed as:

$$d[\delta\phi(x,t)] = k_{op}\delta n(x,t)dx \tag{3.7}$$

where $k_{op} = 2\pi/\lambda_{op}$ and λ_{op} is the optical wavelength in vacuum.

The accumulated phase difference, from a reference $x_0 = 0$ at the waveguide at the start of the antenna gap to the end of the gap is

$$\delta\phi(t_0) = k_{op}\int_0^L \delta n\big(x, t'(x)\big)dx$$

$$= -k_{op}A\int_0^L \sin\,(k_{RF}(\sin\,\theta - n_0)x - \omega_{RF}t_0)dx \tag{3.8}$$

Note that the wave velocity is set to be:

$$v_{op} = \frac{c}{n(x,t)} = \frac{c}{n_0}\frac{1}{1-\frac{A}{n_0}\sin\,(k_{RF}\sin\,\theta\cdot x - \omega_{RF}t)} \approx \frac{c}{n_0} \tag{3.9}$$

where equation (3.1) is used (1) and A is defined as: $A \equiv n_0^3 r E_{\text{slot}}^0\,\Gamma/2$ and c is the speed of light in vacuum. Since $A/n_0 \ll 1$. The group index, $n_g = n_0 + \omega(dn/d\omega)$, is assumed to be close to the effective index. Using a calculated group velocity instead of Eq. (6) resulted in a difference of less than 1% in the optical modulation [9]. Therefore, the phase front at t_0 will reach point x in the slot at time $t' \approx (n_0/c)x + t_0$.

Using Eq. (3.7), The total accumulated phase difference over the length $of\ the slot\ L$ of the antenna is then expressed as (3.7), integrating we get:

$$\delta\phi(t_0) = k_{op}AL\sin\,\mathrm{c}\left(k_{RF}u\frac{L}{2}\right)\sin\,\left(\omega_{RF}t_0 - k_{RF}u\frac{L}{2}\right) \tag{3.10}$$

where the trigonometric identity for the difference of two cosines. and $u \equiv \sin\,\theta - n_0$ is used. For broad side RF incidence ($\theta = \theta' = 0$), we have the following result for the case of time varying, but not spatially varying RF wave. The Equation (3.10) is like the phase

modulation expression for the conventional traveling wave EO phase modulator by replacing sin θ in $u(\theta)$ with n_{RF} [38]

3.4.2 Efficiency of the EOM design

The modulation depth is the term (in equation 3.10):

$$\mathrm{m} = \sin\left(\omega_{RF} t_0 - k_{RF} u \frac{L}{2}\right) \tag{3.11}$$

The modulated (phase) optical signal is then:

$$E = E_{op} e^{j[\omega_{op} t + m\sin(\omega_{RF} t)]} \tag{3.12}$$

Employing the Jacobi-Anger expansion in Eq. (3.12) gives

$$E = E_{op} e^{j\omega_{op} t}\left[J_0(m) + \sum_{s=1}^{\infty} J_s(m) e^{js\omega_{RF} t} + \sum_{s=1}^{\infty} (-1)^s J_s(m) e^{-js\omega_{RF} t}\right] \tag{3.13}$$

where J_s is the s^{th} Bessel function.

The first term within the bracket in the above equation is the optical carrier component and the last two terms are the sidebands. Therefore, for the first order ($s = 1$) the carrier-to-sideband ratio (CSR) of the first-order sideband can be expressed as:

$$\mathrm{CSR} = \left[\frac{J_0(m)}{J_1(m)}\right]^2 = \left[20\log \frac{J_0(m)}{J_1(m)}\right]_{\mathrm{dB}} \tag{3.14}$$

The modulation depth is $m \ll 1$, $J_1(m)/J_0(m) \approx m/2$ to further simplify to:

$$\mathrm{CSR} \approx \frac{4}{m^2} = \left[20\log \frac{2}{m}\right]_{\mathrm{dB}} \tag{3.15}$$

3.4.3 Antenna integrated EOM figure of merit

The authors in [9] proposed an elegant figure of merit for the antenna integrated electro-optic modulators that describes device-specific properties where $m = \frac{\pi V_r}{V_\pi} = \frac{\pi\sqrt{2Z_m P_D A_e}}{V_\pi}$ (where the half-wave voltage V_π and the received voltage V_r) [39] where Z_m, P_D, and A_e are the impedance of the modulator, the power density, and antenna area, respectively.

$$m = \frac{\pi V_r}{V_\pi} = \frac{\pi\sqrt{2Z_m P_D A_e}}{V_\pi} \tag{3.16}$$

Ignoring Ohmic loss of the antenna and using $A_e = (\lambda^2/4\pi)G_r$, and rearranging the expression above and expose the device parameter:

$$m = \pi\left(\frac{\sqrt{2Z_m G_r}}{V_\pi}\right)\left(\sqrt{P_D\frac{\lambda^2}{4\pi}}\right) \tag{3.17}$$

Rearranging equation 3.16 leads to a FOM that describes the physical parameters of an antenna integrated electro-optic modulator [9].

$$\mathrm{FOM}[\mathrm{W}^{-1/2}] = \frac{\sqrt{2Z_m G_r}}{V_\pi} = \frac{m}{\pi}\sqrt{P_D\frac{\lambda^2}{4\pi}} \tag{3.18}$$

3.5 ANTENNA INTEGRATED DESIGN SIMULATION AND MICROFABRICATION

3.5.1 Antenna integrated EOM materials

Devices optical modulation are required to have an electro-optic (EO) effect. For which the electrical property makes the material able to change the its refractive index under a modulating RF signal. There are several non-linear processes by which a millimeter-wave

energy may be used to modulate the optical signals in the proposed detector. These processes are electro-refraction types that makes use of Pockels effect and plasma affect. And the lector-absorption type. In this work we are using the Pockels effect type. Except for the antenna, all material components EOM design considered perform in optical domain. And they will all be monolithically fabricated using a planar-fabrication process.

As we alluded to earlier, recent advances of electro-optic polymers in performance and reliability [40, 41] make them a great candidate for the design of the EOM. Due to their inherent favorable optical properties and their relative ease to use in the standard manufacturing process. They can be span on a variety of substrate including silicon and patterned using standard lithography. This makes them prime candidate to use in high frequency [42] and high performance demanding applications such as PMMW imaging systems such as the one we are proposing.

Organic polymers technology is now capable of producing high speed electro-optic devices, over 100 GHz modulation has been demonstrated as shown in figure 3-5. And sub 1 Volt Half Wave Voltage (V_π) at 1550 nm has been demonstrated [43].

Complex electro-optic devices designs using spin coating, photo lithography and planar-fabrication process on multitude of substrates have also been demonstrated [44]. The flexibility of processing polymer optical material, such as the ability to use different polymer types and hybrid sol-gel/polymer or other passive optical polymer materials within the same optical integrated circuit are some other significant features that are critical for the proposed research. These features allow not only optical-wave and control confinement but can also be optimized for many applications.

For applications such as mm-Wave imaging, the electro-optic modulator is required to have the highest possible efficiency performance at millimeter wave. The stringent sensitivity requirement of the PMMW imaging system necessitates the use of optimum materials and a topology that mitigates all types of losses within the optical path of the photonic chip. For this work, that entails high fiber coupling efficiency, choice low loss in passive optical waveguide material with large effective optical confinement, the devices design topology, and an active EO polymeric materials with high optic coefficient.

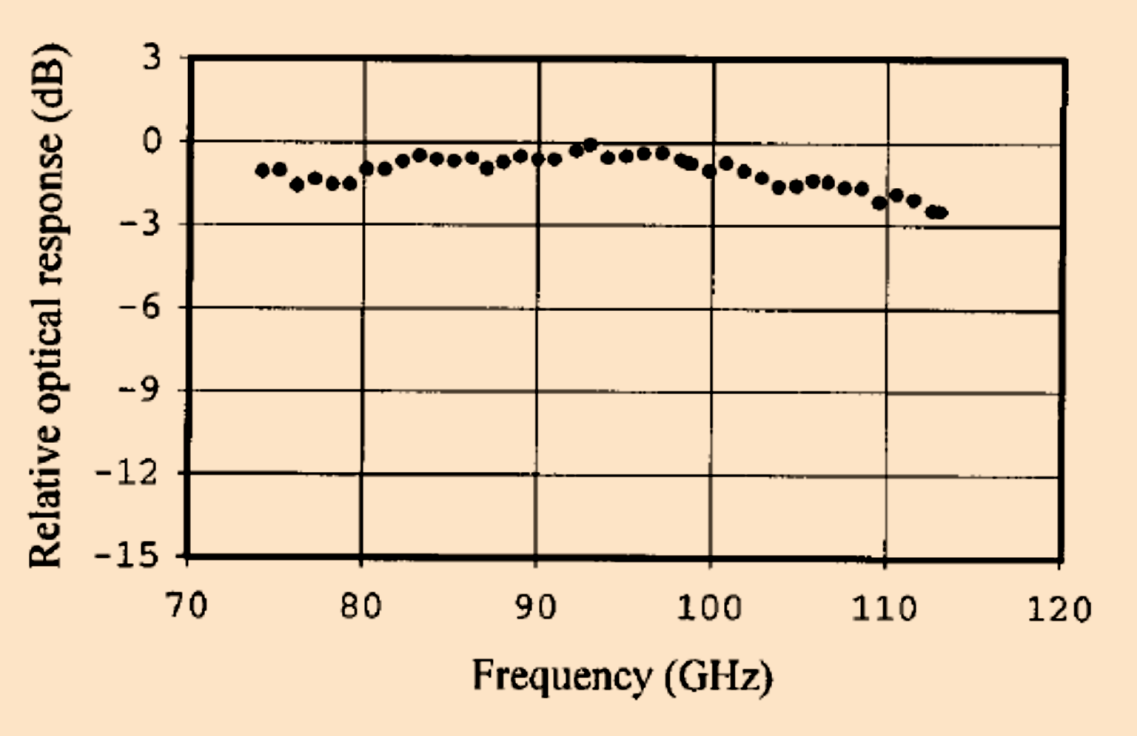

Figure 3-5 High frequency optical response curve of EO polymer modulator from 74 to 113 GHz. The total variation was less than 3 dB [43].

High EO coefficient, which a material characteristic, is required for high conversion efficiency modulator design, however active electro-optical polymer specifically designed for high electro-optic coefficient will inherently have higher optical propagation loss

compared to a passive material such as other polymer or sol-gel designed uniquely designed and optimized for passive optical waveguides and device interconnects. It is therefore advantageous to use lossy materials only in the section of the EO modulator device design only where it's needed, i.e., the active section of the modulator wave guide. This will specifically be beneficial for a large array design where the transmission loss over longer propagation paths can affect sensitivity performance. An additional benefit in using optimized for low loss material for passive wave guide in the optical circuit integration is that they can be chosen to provide an optimal match to a standard optical fiber for efficient coupling. The design scheme of incorporation of the nonlinear polymer only where the modulation takes effect is illustrated in figure 3-6.

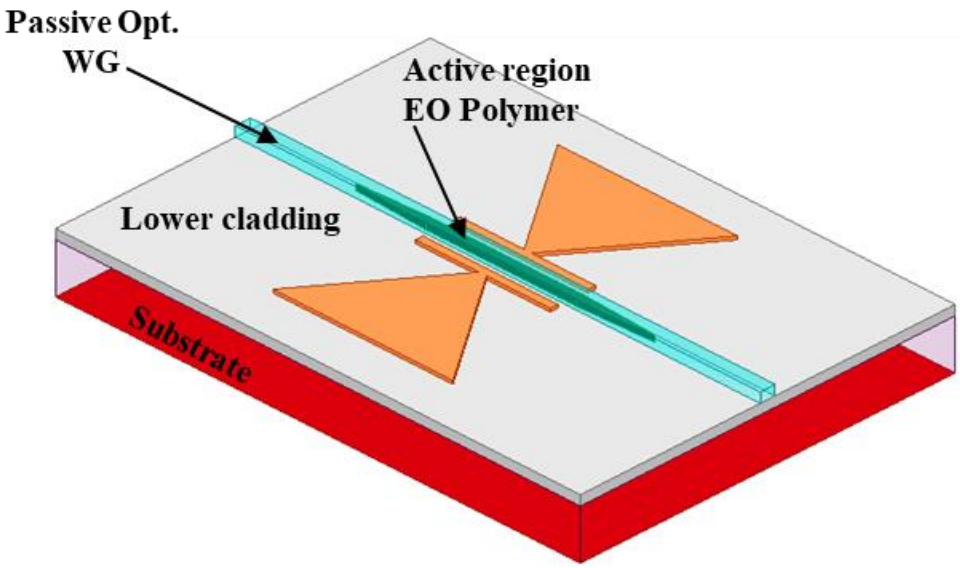

Figure 3-6 Antenna integrated EOM design showing the active polymer within the antenna gap.

An optimum passive wave guide mode pattern is almost circular while the mode pattern in an electro-optical modulator is elliptical, and simply butting together the two wave guides can result in detrimental losses due to the mismatch in reflection coefficient as well as the geometry at the interface. The Functionality of the EOM design is as follows: The optical signal carrier travelling through a standard single mode fiber is coupled to patterned optical polymer low loss waveguide. Once it reaches the active section of the modulator, the optical signal is coupled to the electro-polymer (active region) waveguide where phase modulation takes place. At the other end of the active, the phase modulated signal couples back to low loss polymer optical passive waveguide (as depicted in figure 3-6)

This coupling behavior is made possible by the difference in refractive indices between the active (EO polymer) and the core passive optical waveguides (passive polymer). The refractive index of the passive is chosen such that it favors an optimum transition and low loss. To facilitate the transition, the active portion of the nonlinear polymer waveguide is tapered to minimize the reflection in the interface and extends beyond the antenna gap. This topology mitigates fiber coupling loss, propagation loss, allow for an active high Pockels electro-optic effects EO polymer material be applied only where needed. It is cost effective for device fabrication and is mostly independent on electro-optic polymer used. And it contributes to the overall modulation efficiency and achieves high sensitivity of the overall system.

Poling is a critical and an essential processing step for electro-optic polymers. And the poling recipe involved involves applying voltage and temperature the of which is

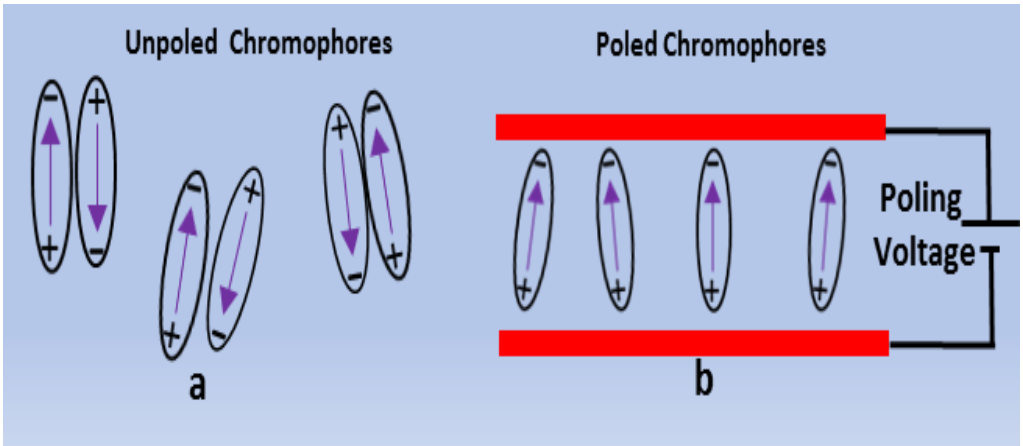

Figure 3-7. Antiparallel Unpoled chromophores Pairs (a), Poled chromophores (b)

electro-optic material specific. Poling induces the optical effect necessary for active optical devices such as electro-optical modulator. For a given electro-optical polymer material, chromophores dipoles are paired randomly in an antiparallel fashion as shown in figure 3-7 (a), statistically this pairing results in a zero net change in polarization.

The necessary optic-effect requires a net polarization gradient in the active polymer, this is mainly accomplished in three steps, heating, applying high voltage and cooling. The poling recipe varies with the EO polymer material used, the voltage and temperature levels and cooling speed material dependent. Essentially, after the poling process, dipolar chromophores suspended in the polymer host reorient to look like figure 9(b). Poling electro-optic polymer materials sets the vector-optical tensor r_{33} (the nonlinearity parameter of the material) that induces a change in the refractive index of the electro-optic material at the presence of an electric field. Poling efficiency of an electro-optic polymer is defined as the ratio of the in-device poled r_{33} and single thin film poled r_{33} of the same material. In practice, it is challenging to achieve in device 100 percent poling efficiency. In device poled

electro-optic polymer tend to have lower r_{33} mainly because: during the poling process, in device active polymer is usually sandwiched within cladding materials and/or other buffer layer that causes some of the voltage to drop in these surrounding layers and prevents the electro-optic layer from receiving a full voltage needed dose. One way to ensure high poling efficiency is to reduce the voltage drop in the materials surrounding the active area to be poled; this can be done by controlling the conductivity of the cladding. Sol-gel cladding material conductivity can easily be altered through doping such that it is much higher than that of the electro-optic polymer at poling temperature and applied voltage. Another way to improve poling efficiency is to use more favorable poling material. For this research, we use commercially available electro-optic polymer and Epocore and Epoclad as the passive optical material.

3.5.2 Antenna integrated EOM design

Two Antenna integrated lector-optic modulators are designed. They differ only in antenna type used. Figure 3-8 shows a cross section view of the device and the simulated dimensions. The optical wave guides, both in the passive and the nonlinear region withing the slot of the antenna are designed to propagate a single TE mode. The antennas, namely, a path antenna and a microstrip bowtie are designed to resonate at 94 GHz explained in more detail in the next chapter. A key design parameter are the slot dimensions for the path, the extended bars of the bowtie and the resulting field enhancement within these gaps. Field enhancement is an important parameter as it provides a electrical field to the nonlinear polymer waveguide and promotes efficiency and sensitivity. Therefore, the antenna design needs not only to provide resonance but also a high filed enhancement in addition allowing for microfabrication processability. Table 3 lists the material used in the

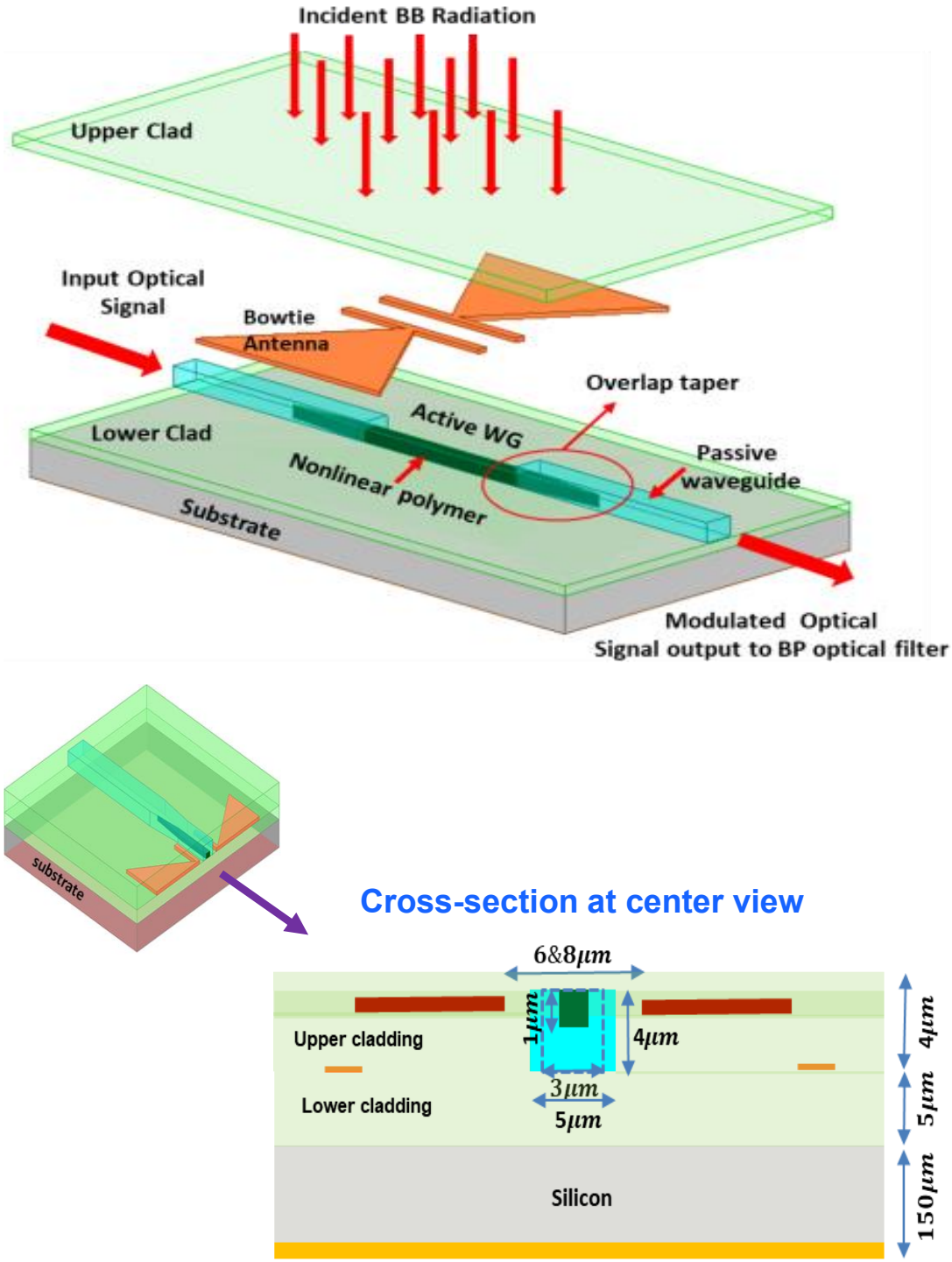

Figure 3-8. Designed antenna integrated EOM design showing all the microfabrication component involved (top). Cross section showing all the dimensions.

microfabrication process to be discussed in the next section. The nonlinear polymer used is JRD1 from NLM PHOTONICS with the following published properties:

- Electro-optic coefficient (r_{33}):
    - Up to 390 pm/V in a silicon-organic hybrid device at 1550 nm
    - Up to 556 pm/V in a parallel plate configuration at 1310 nm
- Refractive index at 1550 nm (from VASE) = 1.83 – 1.85
- Thin film absorption maximum (m_{ix}): 800 nm
- Hyperpolarizability (β) in CHCl3 at 1300 nm: 3330 x 10^{-30} so ± 50 x 10^{-30}
- Thermal stability: < 50 °C
- T_d: 226 °C
- Poling temperature: ~85-90 °C
- T_{og}: 82 °C

Table 3-1. Effective Emissivity of common materials

Component	Material
Active waveguide	Nonlinear Polymer JRD1
Passive Waveguide	EpoCore
Substrate	150 µm thick Si
Upper/Lower Clad	EpoClad/EpoCore
Metal	Al

3.5.3 Optical waveguide transition design

The antenna integrated EO modulator is depicted in figure 3-8 shows its individual components are: Lower/upper claddings are off-the -self-optical polymer materials. Active nonlinear polymer (JRD1). Passive optical waveguide for which a commercially available Epocore is used. The Patch/bowtie antenna is inserted on top of lower cladding. The design has the following features:

- EO phase modulator with an integrated antenna to operate at 94 GHz & 1.55 nm optical signal
- Poled polymer based, and takes advantage of high 2nd order nonlinearity effect (Pockels- effect)
- It makes use of planar patch antenna (with a slot in the middle) to promote low optical loss, increase modulation efficiency; increase optical and rf velocity match and higher antenna directivity.
- A unique device architecture that promotes efficient poling
- The architecture utilizes the polymer only where needed, while a passive low loss optical wave guide is used to channel optical signal within the chip.

Directly coupling light from an optical fiber using face coupling into much narrower optical waveguide is inefficient due to large difference in modal area. Commercial single mode core fiber tips are ~4-8 microns. Furthermore, the nonlinear polymer tends to have large optical signal attenuation, therefore we elected to use it only where it's required, namely where the modulation takes effect. To mitigate these two issues, an adiabatic/spot-size converter transition is designed into the EO modulator architecture device that consists of:

- Passive waveguide using Epoclad as a passive polymer material.
- Active waveguide tapered on each extremity using nonlinear polymer.
- The two waveguides overlap in the tapered region for smooth transition (referred to as a spot size conversion).
- The whole structure is embodied in an upper cladding optical passive optical polymer material (Epoclad)

The fundamental mode of the smaller index Epocore waveguide propagates through the taper, the modal fields slowly couples into and out the narrower non-linear polymer tapered waveguide. The design goal is to optimize the taper dimensions of the non-linear optical wave guide in such a way as allows the fields to smoothly transition with minimal back reflection. When the taper is gradual enough, the fields will smoothly transition to the fundamental mode of the next waveguide (the nonlinear waveguide region) before exiting

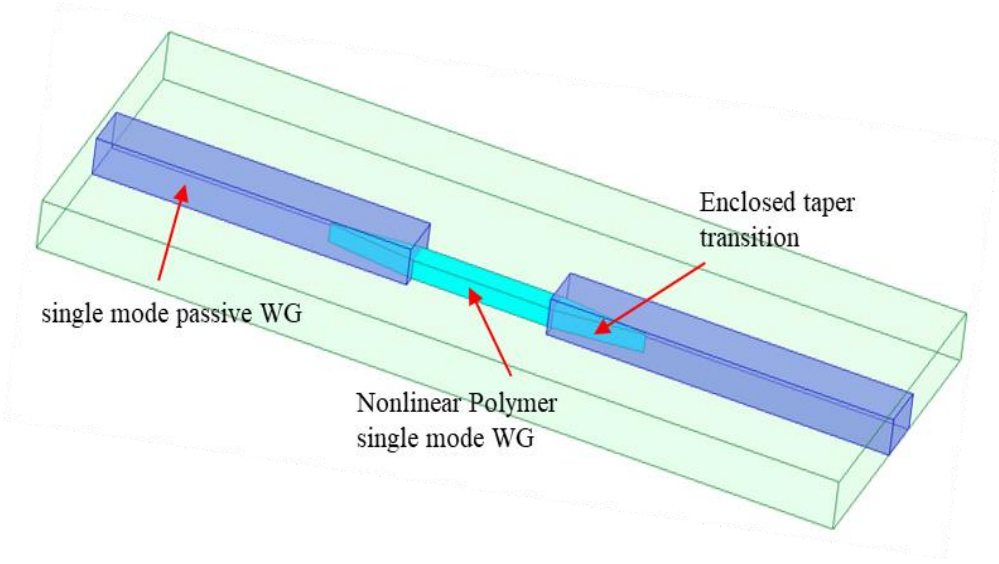

Figure 3-9. Back-to-back fundamental mode adiabatic transition, spot-size converter

at the other end in a back-to-back configuration., with minimal back reflection. The simulated design structure is shown in figure 3-9.

Before the design of the adiabatic transition. The two waveguides, namely the passive optical waveguide and the active waveguide are independently designed and dimensioned designed to carry a single TE/TM mode for the given material properties. The material used are Epoclad and Epocore for passive and active waveguides respectively. The simulated passive and active waveguide results are shown in figure 3-10 and figure 3-12. Also shown in figures 3-10 and figures 3-11 are their respective index and E-field intensity profile. The single optical mode TE/TM mode waveguide dimensions are determined by simulating the effective index as a function of the waveguide dimension and observing the cut-off dimension of the desired mode. These simulation results show that in order for only a single mode (fundamental) to propagate the active and passive waveguides cannot exceed 2μm and 4.25μm respectively. The E-field intensities of the designed waveguides shown in figure 3-11 and figure 3-13 are for the waveguide sizes of 2μm and 4μm corresponding to the active and passive waveguides respectively. Note that the field is well confined for a single mode within these dimensions.

Following the dimensioning of the passive and active waveguides individually, a back-to-back transition is built and drawn into the simulator to determine the extension and the size of the overlap portion of the two waveguides shown in figure 3-8. Note that in the actual device the passive waveguide extends to cover the entire length of the nonlinear polymer. A 1550 nm light beam is launched from one port and propagates through the taper overlap (transition) and exits on the second port. And the conversion efficiency is recorded as a function of the taper length.

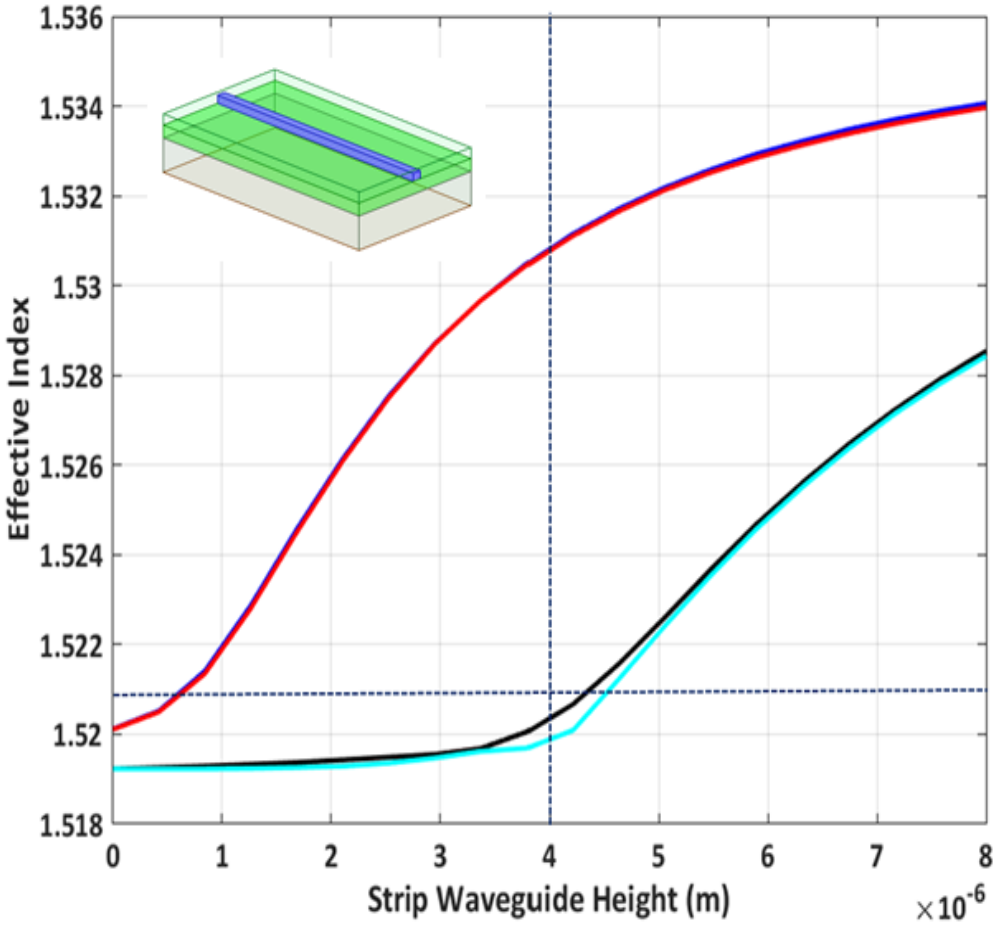

Figure 3-10. Passive optical waveguide TE/TM mode simulation profiles, effective index as a function of waveguide dimension, both results are for 1550 nm wavelength.

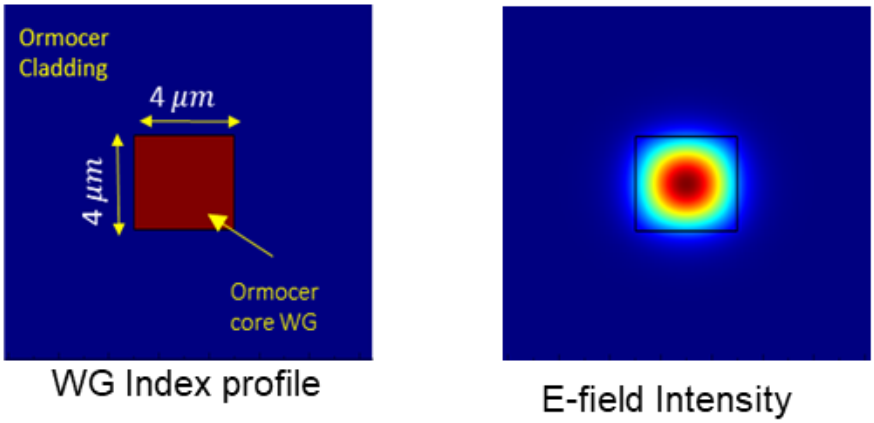

Figure 3-11. A 4x4 micron passive waveguide with Ormocer polymer hybrid materials at its core and cladding.

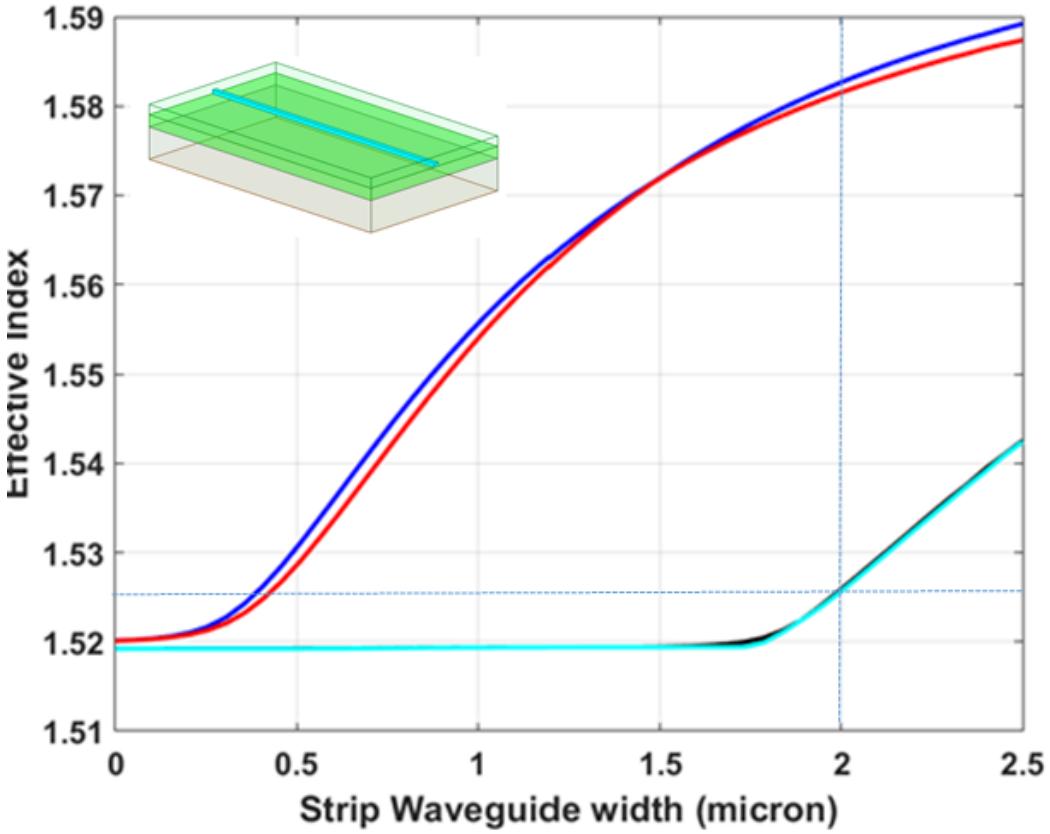

Figure 3-12. Active waveguide TE/TM mode simulation profiles, effective index as a function of waveguide dimension, both results are for 1550 nm wavelength.

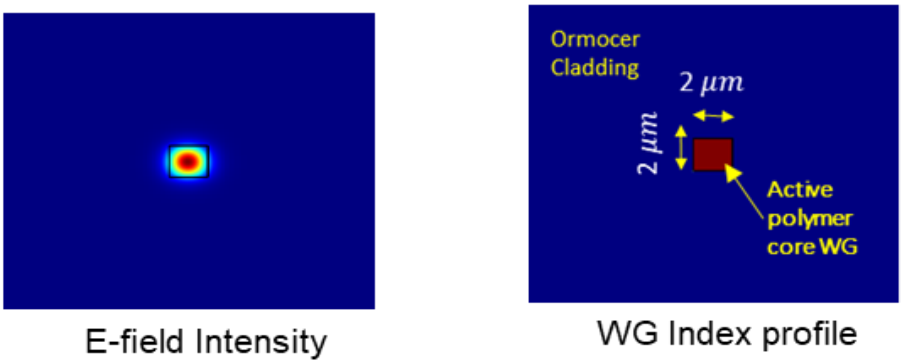

Figure 3-13. 2×2-micron active polymer waveguide with Ormocer as its cladding material.

The back-to-back transition model shown in figure 3-9 is optimized to produce an adiabatic transition which is mainly a function of the taper length in the overlap region of the passive and active waveguide and end of the taper dimensions. In the simulation a single mode is launched on one side of the passive waveguide designed for 1550 nm wavelength. This fundamental mode propagates and encounters the tapered active polymer waveguide overlap region. This mode slowly leaks into the active region with higher refractive index and becomes confined at the end of the overlap region and continues propagating solely in the active polymer wave guide. In this design topology, the length of the active region is dictated by the antenna width (slot width), while the waveguide overlap is determined by the transition performance. The goal is to achieve a transition with minimal loss by reducing light wave reflection. This requires optimizing the taper length, and the width of its extremities. The simulation shows that by for a given taper end width there is an optimum taper length where the optical transmission becomes constant minimum. For this design, both active and passive waveguides are designed to support single mode at 1550 nm,

Figure 3-14 shows the result of with the base width of 120nm at end of the taper. A tapper longer than 400 microns is needed to achieve close to 98% efficiency. Figure 3-15. shows the index profile and the electrical field intensity (|E|^2) profile seeing from the top and side views.

The field shows excellent transition and confinement of the field within respective waveguides. Note the field intensity looks much more intense in the middle region in shown intensity scale, this because the end waveguides sidewalls of the back-to-back transition (passive waveguide) are twice as large as the middles section. The cross section of the back-

to-back transition is depicted in figure 3-16. It also shoes multiple slices of the E-field magnitude along the propagation from port 1 to port 2. The simulated results clearly show the expected mode size that is well confined within the respective modal area as it transitions from a lower refractive index to higher one and back.

.

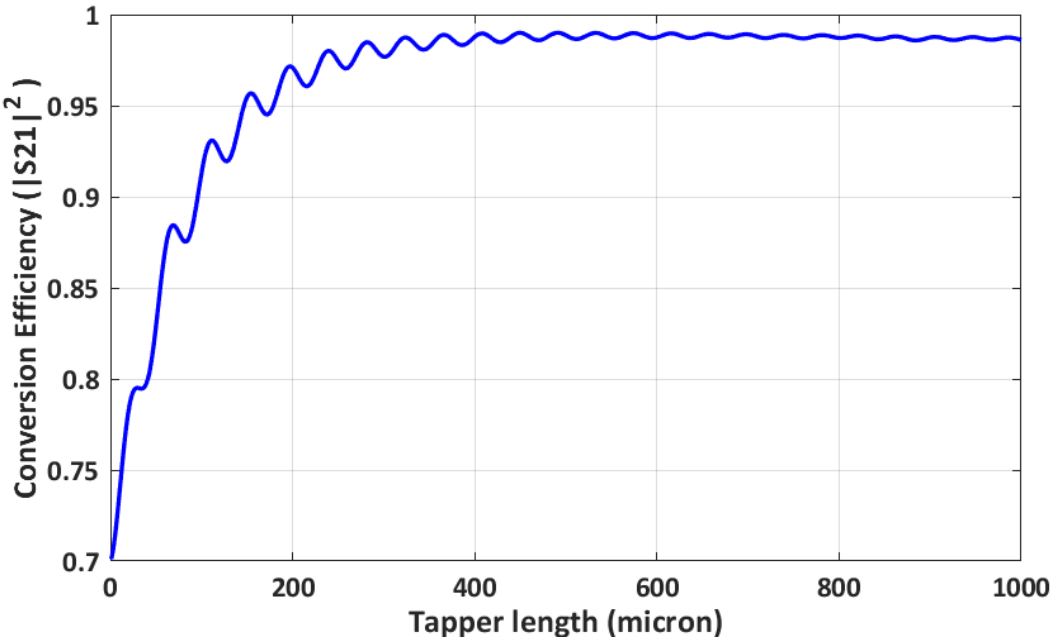

Figure 3-14. The conversion efficiency as a function of taper length

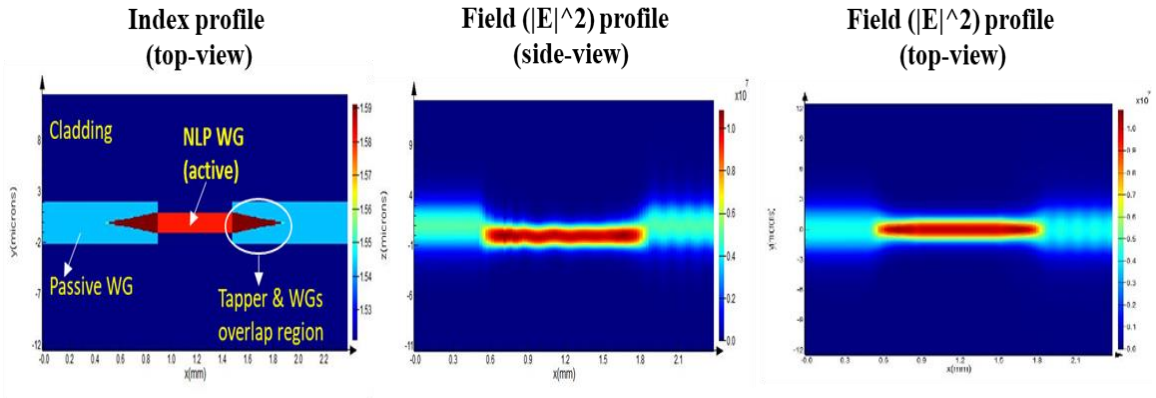

Figure 3-15. Material index profile (left). Field intensity along waveguides transition side and top view (right).

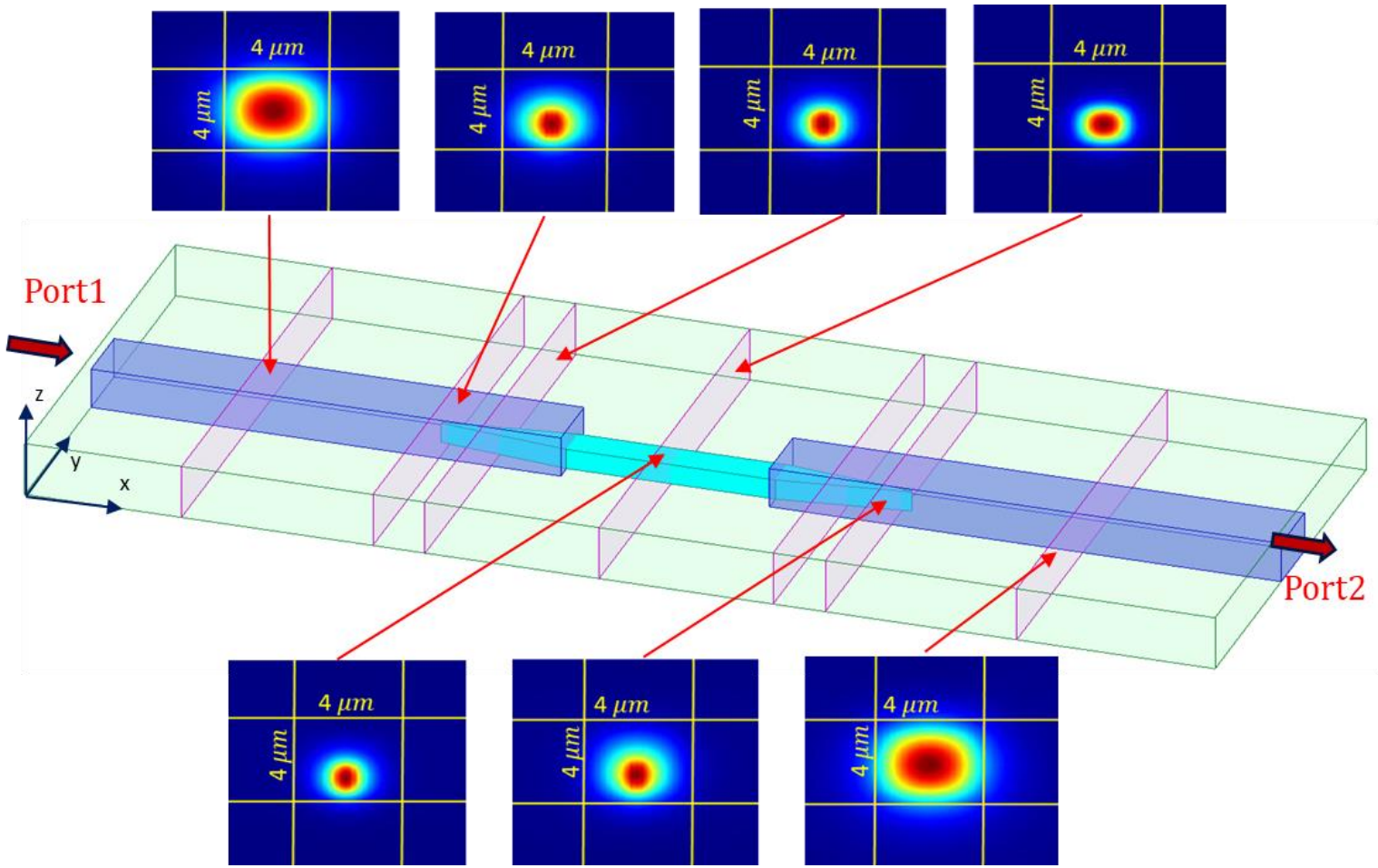

Figure 3-16 Calculated Electrical field in the y-z plane at various stages of the back-to-back transitions.

3.5.4 EOM microfabrication process

In this section the microfabrication process summary is described in more detail. The entire process consists of 16 steps. These steps are described in figures 3.17 to figure to figure 3.20. The first four microfabrication processes are as follows:

A high resistivity, 150-micron thick (dictated by the antenna performance design) is used as a substrate. A deep cleaning using the silicon standard cleaning procedure is followed to remove particles and impurities from the surface. After cleaning process, a 1-micron thick aluminum is deposited on the back side of the 2-inch wafer using the e-bean metal evaporator. This metal serves as the ground plane for designed antennas. The final dimensions of the electro-optic modulator design are illustrated in figure 3-8. Precise control of all these dimensions is necessary to control the behavior of the final EOM device in order to control and to confine the proper propagating mode. The depicted in figure 3-17 the first step is the deposition of 5-micron of the lower cladding, namely, the Epoclad. We have used the vendor's spin curve as a starting point to make necessary adjustments. A new spin built a is shown in figure 3-21. Another necessary preliminary step is the measurement of the refractive index for both the cladding and core materials, Epoclad and Epocore respectively. This is critical as the refractive indices values in difference control the behavior of the optical signal propagation and the dimensioning of the optical waveguide.

For this purpose, an Attenuated Total Reflectance (ATR) operating a 650nm laser is used to measure both deposited thickness and the refractive indices. The established spin curve and the measured refractive indices are shown in figure 3-21. Using this spin curve a 5-micron thick Epoclad is deposited on the silicon substrate and cured using irradiated UV, post bake and hard bake. After deposition of the lower cladding, a set of alignment

Claddings & Passive waveguide Patterning processes summery.

Processes (1-4):

1. **Lower cladding deposition:**

   Spin coat of Epoclad on 150-micron silicon substrate

2. **Alignment marks patten:**

   Lift-off- process is used to pattern the alignment mark to be used for subsequent photolithography steps

3. **Core material deposition:** Spin coat of the core material (Epoclad) for the passive optical waveguide

4 **Metal deposition:**

   Used for optical waveguide patterning, a lift-off process as in step 2

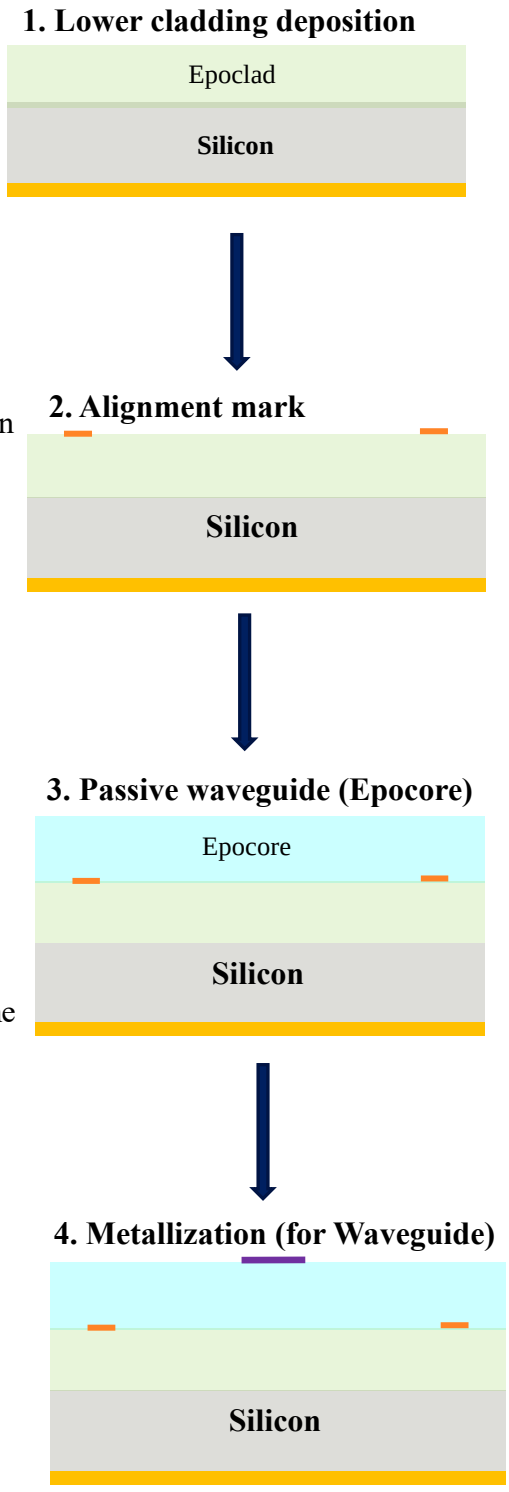

Figure 3-17. 1 to 4 of 16 designed microfabrication processes steps used in the EOM fabrication.

Passive optical waveguide pattering and dry etch process summery

Processes (5-8):

5. Dry etch unmasked area using dry etch process using ICP RIE dry etch process

6. Deposit Upper cladding and dry etch excess material to expose the waveguide masking layer

7. Dry etch to remove excess material to ready for antenna mediazation

8. Antenna metal deposition:
   Liftoff and e-beam evaporation

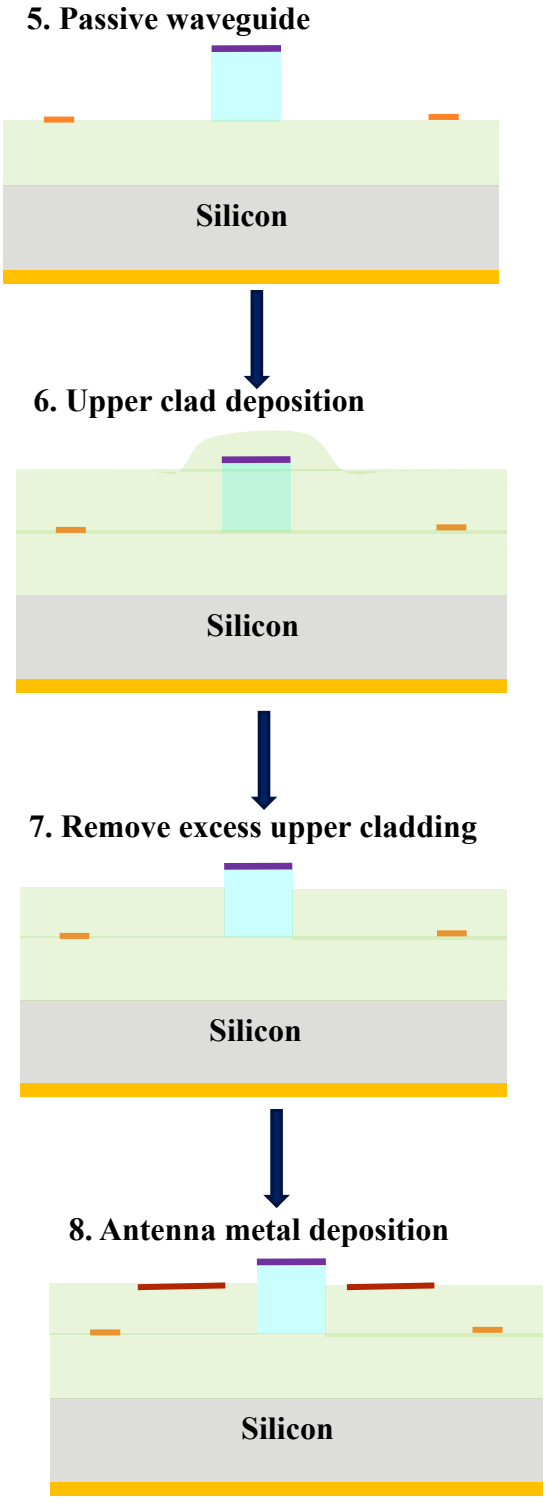

Figure 3-18. 5 to 8 of 16 designed microfabrication processes steps used in the EOM fabrication.

Upper cladding dry etch to expose antenna and passive waveguide masking metal

Processes (9-12):

9. Upper clad is deposited using spin coating

10. Lithography step to introduce void in deposited upper cladding to used for poling probes

11. RIE dry etch to expose waveguide masking metal

12. Spin coting od upper cladding thin layer (optional)

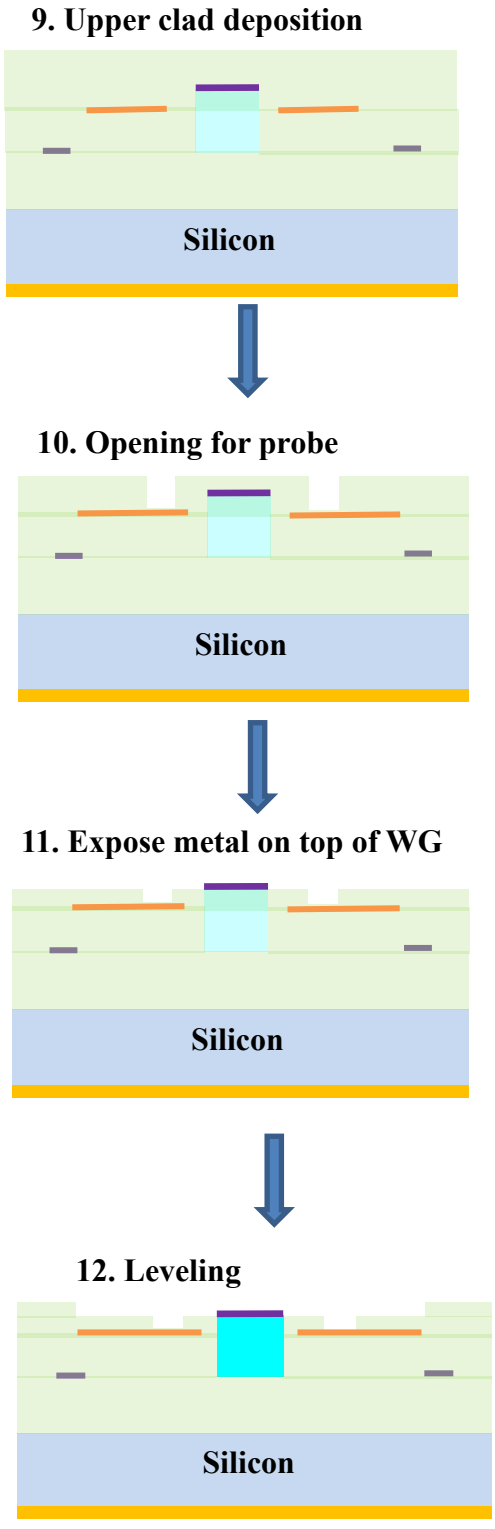

Figure 3-19. 8 to 11 of 16 designed microfabrication processes steps used in the EOM fabrication.

Nonlinear polymer waveguide patterning & passivation

Processes (13-16):

13. Etch a window on the passive waveguide metal mask.

14. Dry etch the core material to pattern the nonlinear polymer waveguide and wet etch the remaining metal mask

15. Spin coat the nonlinear polymer

16. Passivation using Epoclad or SiO_2 to protect the device

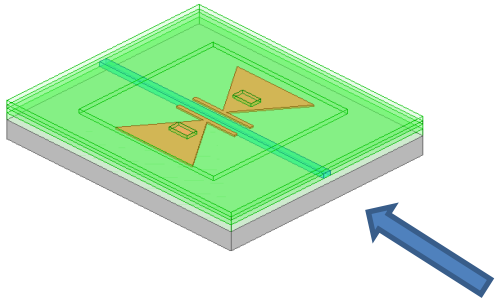

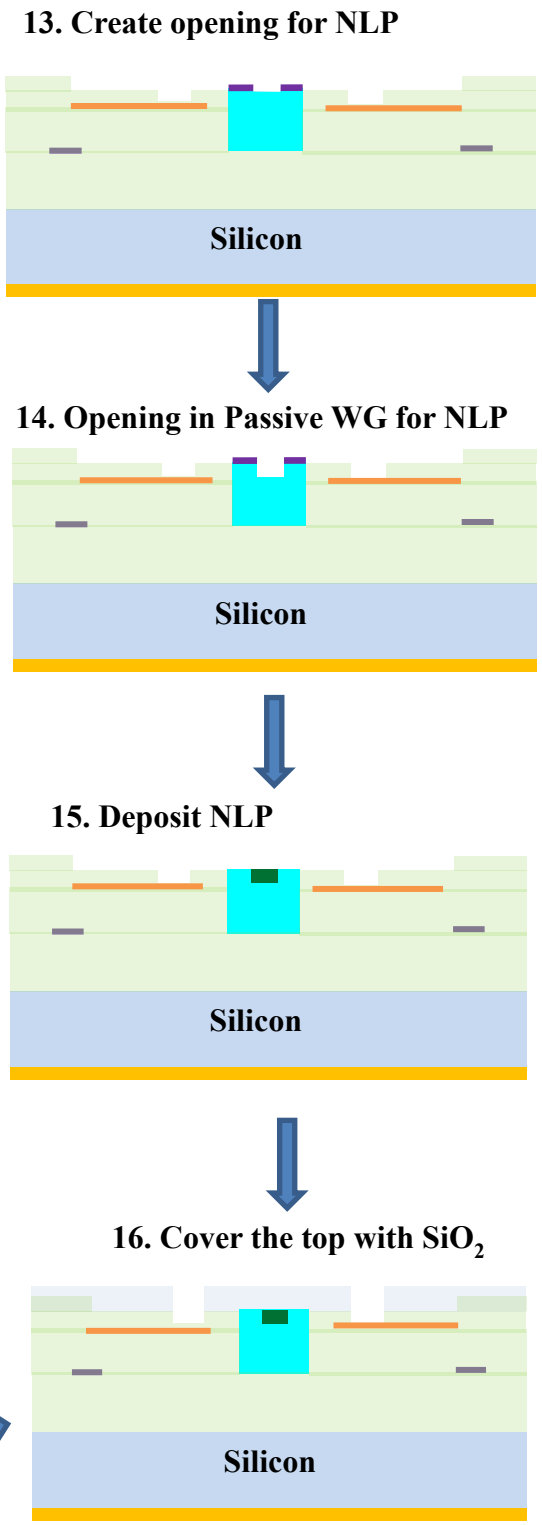

Figure 3-20. 13 to 16 of 16 designed microfabrication processes steps used in the EOM fabrication.

makes are patterned and metalized on of the cladding using the lift-off process. Where a negative (NLOF 2020) photo resist is used to pattern, and an e-beam evaporator is used. Figure 3-22 shows the lift-off process used and some of the results obtained through this microfabrication process. The are many metallization steps in in process and the described lift-off process is used in all of them.

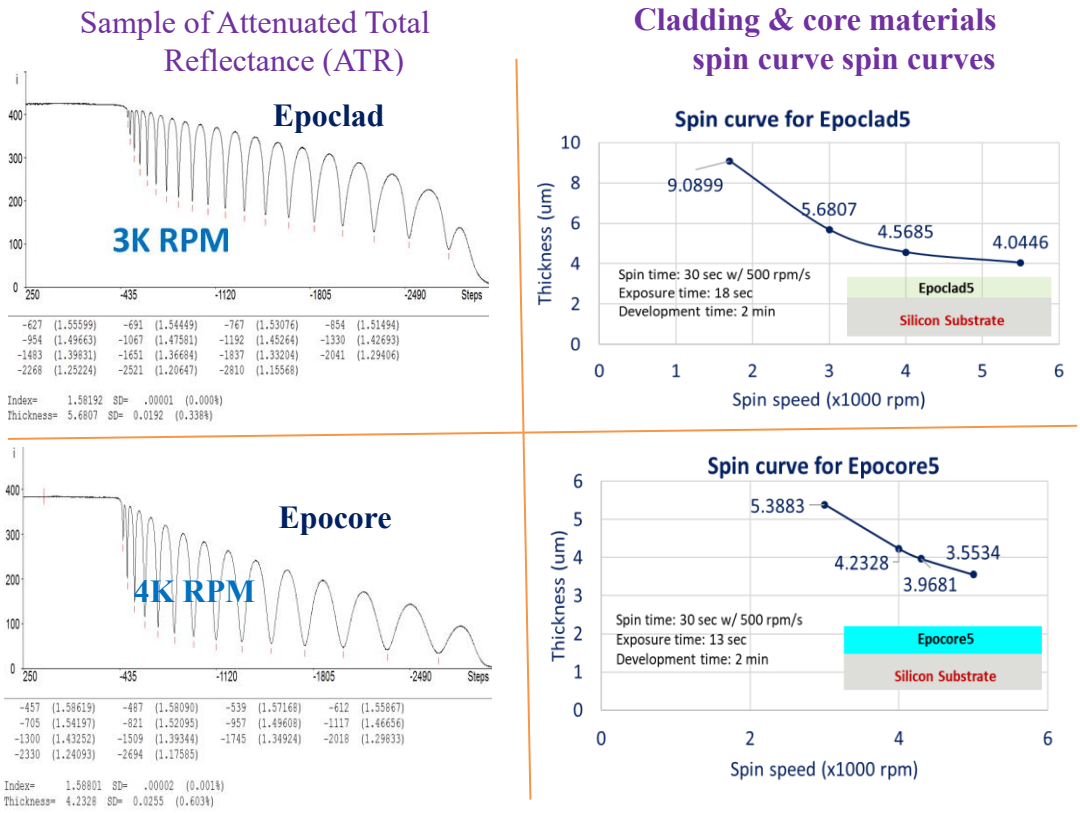

Figure 3-21. Epoclad and Epocore cladding spin curves and refractive index measurement using ATR

After adjustment has been made to the recipes at hand and a successful metallization of the alignment marks to guide the process flow, a 4-micron of the core material (Epocore) is deposited on the top of the lower cured cladding containing the metalized alignment mark.

This layer is used to pattern and etch the passive optical waveguide. For this purpose, a metallic masking layer is used by depositing 100nm of Au using the lift-off process described above.

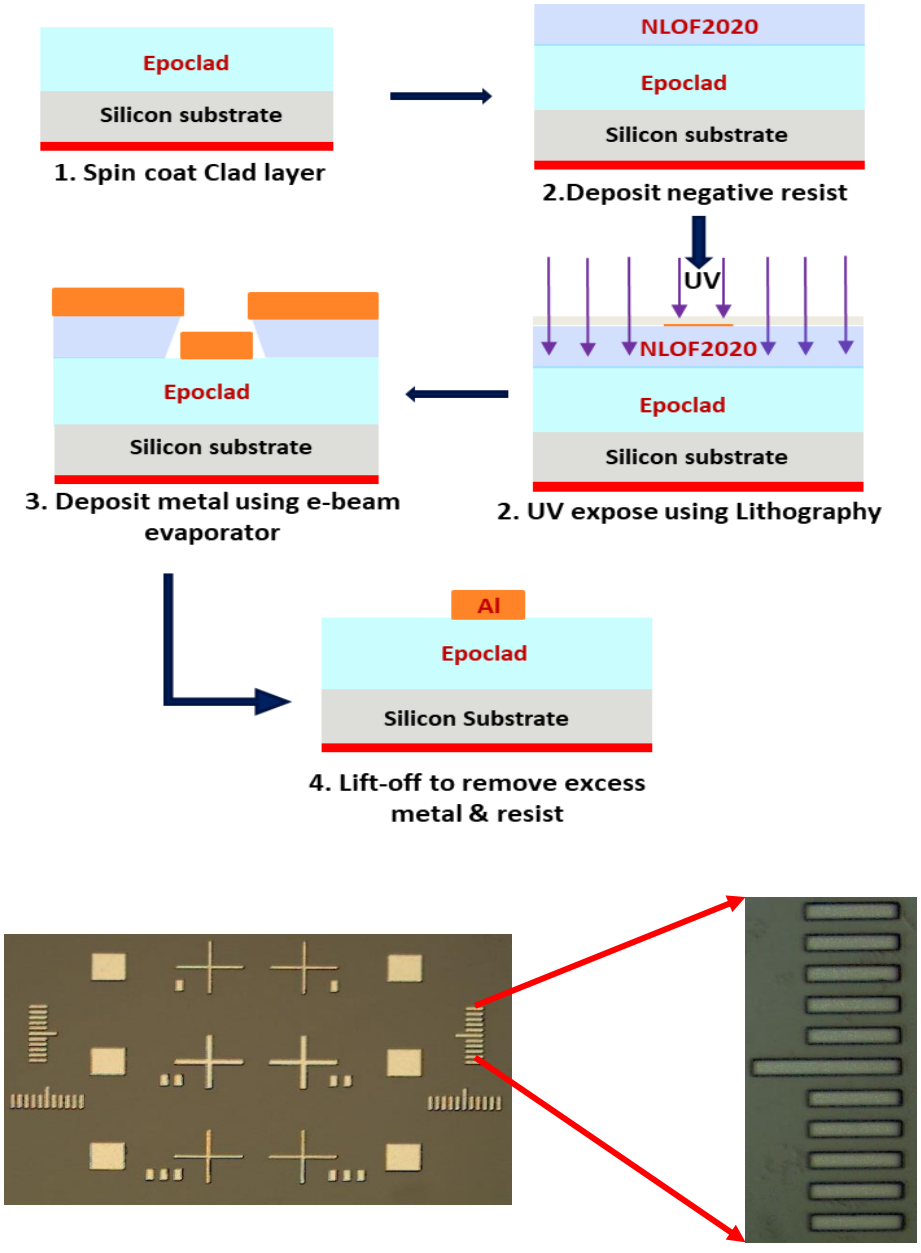

Figure 3-22. Metallization using Lift-off (top) SEM picture 5-micron features patterned alignment marks (bottom)

In the microfabrication processing steps 5 to 8 of figure 3-18, the passive optical polymer waveguide is pattern and antenna metal is deposited. For the antenna the lift-off process previously established for patterning the alignment marks is used. As for the passive waveguide however, a new recipe is developed to dry etch the core and the cladding materials. This entailed choice of appropriate gases, their flow rate and pressure. To obtain as vertical as possible side wall as possible for the passive optical waveguide a reactive inductively coupled reactive ion etcher (ICP-RIE) is used.

Given the nature of the cladding and the core materials i.e. Epocore and Epoclad as polymer based electro-optic materials within the EOM device, the microfabrication process implies the use of a suitable etching process, namely the ICP-RIE and hard mask. To dry g using the ICP-RIE, we deposited aluminum for the alignment marks and gold for the waveguide patterning hard mask creation. Notably, we used sulfur hexafluoride (SF_6) and oxygen (O_2) combination as gas etchants. These gases in combination with appropriate flow rate and pressure provided a favorable anisotropic etch rate that is key to the optical waveguide profile.

To obtain a dry etch favorable dry etch recipe, cation, a metal is patterned on the top of the cladding Epoclad and on the core material Epocore using lift-off and e-beam evaporator. Subsequently, ICP-RIE etching process is performed under multiple variable conditions. Figure 3-22 summarizes the final use recipe in all EOM microfabrication process ICP-RIE dry etch. Figure 3-23 shows an example of the profile of etching using Epoclad with aluminum as a hard mask for a duration of 2 minutes

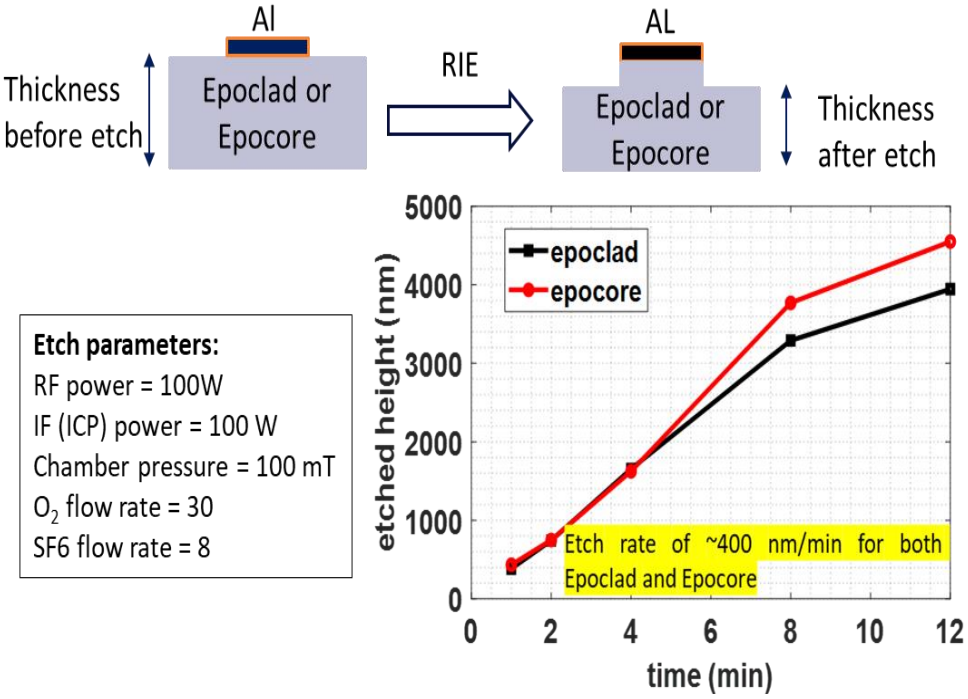

Figure 3-23. Dry ICP-RIE etch process; recipe and etch rate for Epocore and Epoclad materials

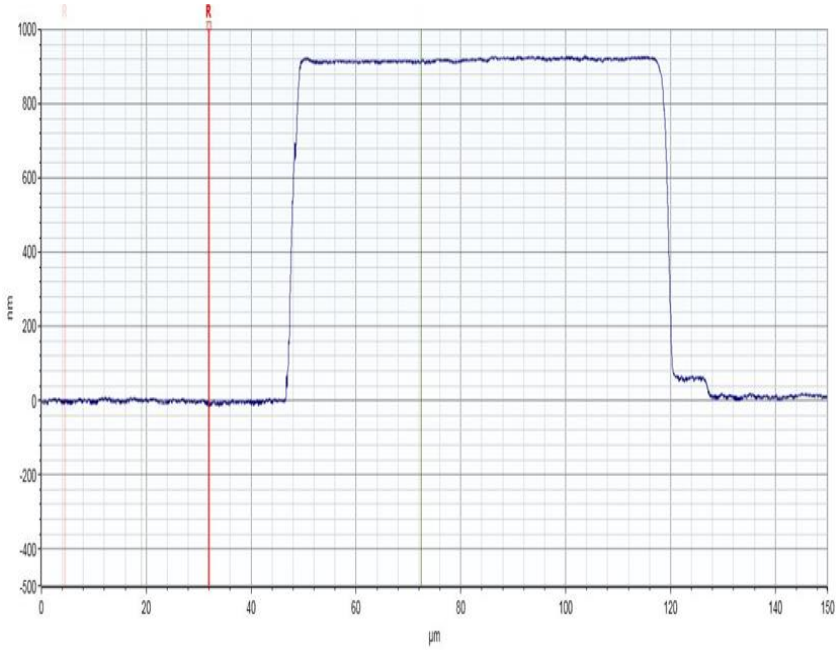

Figure 3-24. ICP-RIE etch step profile using Epoclad material, and a patterning duration of 2 minutes

One all the processing recipes such the lift-off, metallization (including adhesion issues), ICP RIE dry etch and wet etching of masking metal, were established, tested and verified. A count of 9 photolithography masks were required to go through the microfabrication process described in figures 3.17 to figure 3.20 sequentially to microfabricate the electro-optical polymer. Depicted in figure 3-25, is a snapshot picture as if stacked masks layout. The inset is two electro-optic modulator designs using two different antennas, one is a bowtie with extended bars at its apex to accommodate the nonlinear polymer and modulation. The other is a microstrip patch antenna with a slot in the middle.

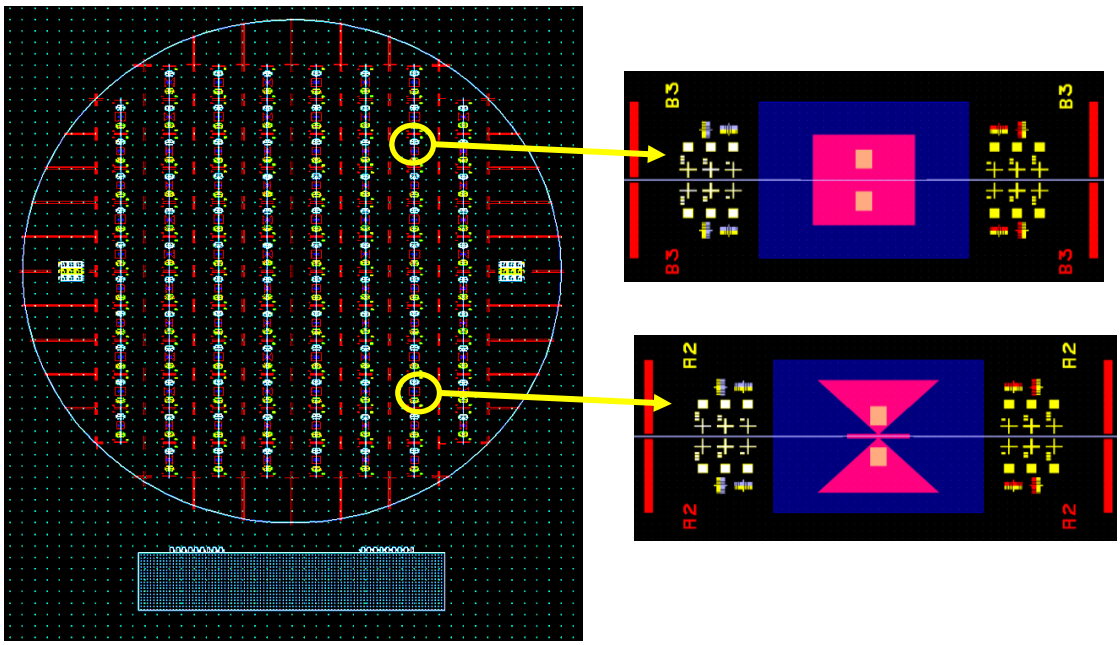

Figure 3-25. A stacked photolithography mask set used the described microfabrication process. The insets are pictured of patch and bowtie antennas EOMs.

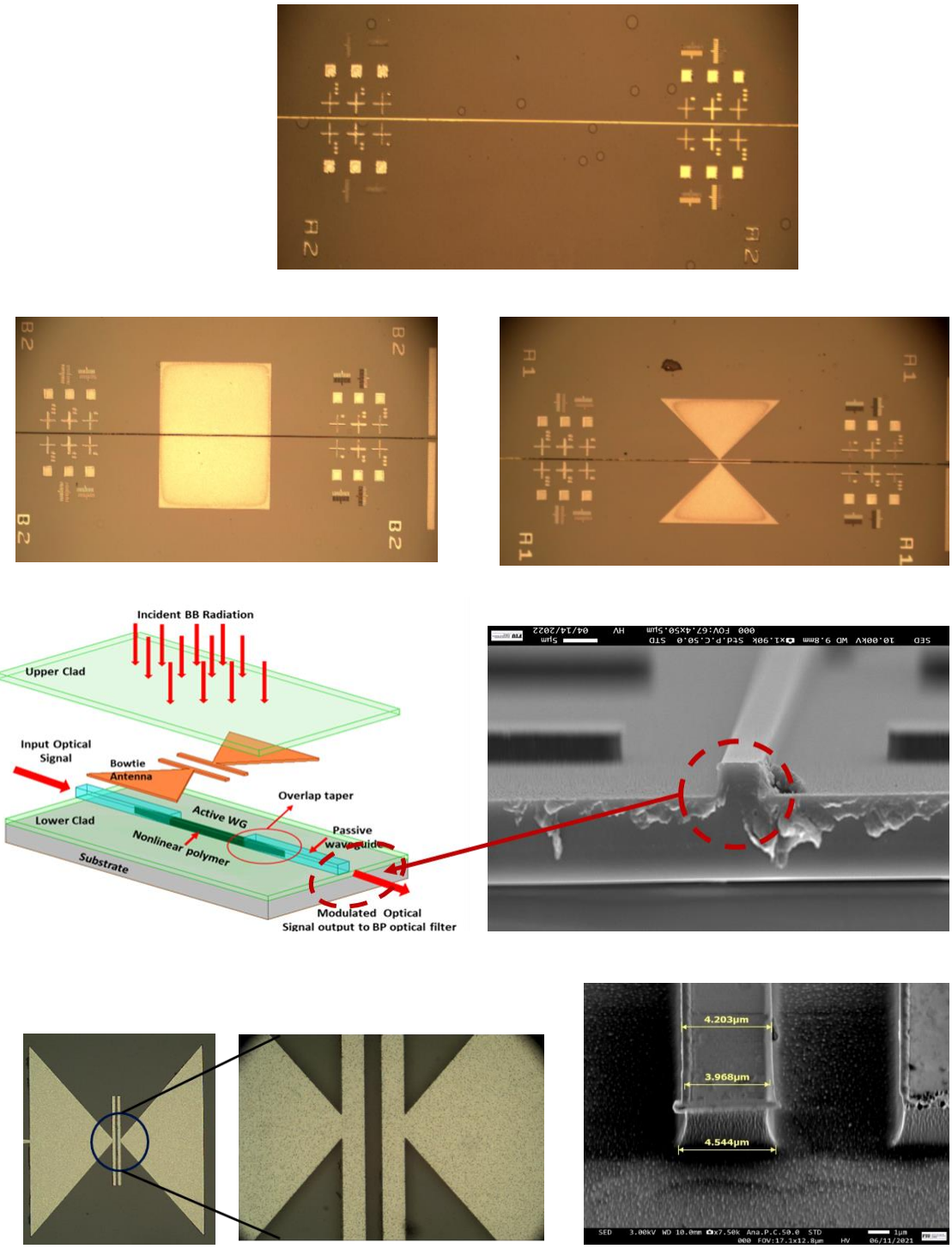

Figure 3-26. Metallization using Lift-off (top) SEM picture 5-micron features patterned alignment marks (bo

CHAPTER 4

SUITABLE PLANAR ANTENNA DESIGN FOR INTEGRATED ELECTRO-OPTIC MODULATOR

4.1 INTRODUCTION

One of the key challenges in designing passive mm-wave imaging systems at high frequency such as 94 GHz is the way the incident radiation from the antenna is coupled to the imaging system. At higher frequencies conductor loss influences both sensitivity performance and form factor [45]. In most cases, system designers' resort to using LNAs for amplification further exacerbates the architecture and cost when array format is considered. To circumvent these issues, a solution would be to directly integrate the antenna onto the electrooptical modulator. And make it we propose a solution of **antenna-coupled** an integral part of the modulator. The expected benefits are modulation efficiency improvement, low cost, and considerable reduction in complexity and size. It avoids associated practical problems such as Ohmic excess loss, interconnect parasitic losses, and mismatch issues. It would also overcome the limiting material dispersion on bandwidth-sensitivity product.

The practicability of on chip antenna integrated electro-optic modulator (EOM) operating in the millimeter wave regime is gaining traction now more than ever. They can be used in a wide range of applications and provide solutions to current pressing needs in communication data through put, electromagnetic sensing, electro-optical modulation in transceivers and millimeter wave imaging systems. Electromagnetic waves are directly modulated by an optical carrier within an EOM promoting a direct impact on efficiency,

bandwidth, sensitivity, speed and permit use and integrate solid state photodetectors. This will mostly benefit the upper band of the millimeter wave regime where the conductor loss and cost and size can be prohibitive in an all-electronic system in the mm-Wave imaging applications. The main components of an electro-optical modulator, regardless of the type, are: the sensing component such as an antenna or electrodes. an active optical region and a passive signal medium such as optical waveguide or fiber.

For this research, the design is on chip antenna integrated modulator focus on the application of interferometric passive millimeter wave imaging camera system in the operation regime of 94 GHz or 77 GHz, where the RF sensing element is a millimeter wave antenna. Such a system has a demanding sensitivity requirement driven among other components by the sensing antenna elements in the front-end especially when LNAs are to be avoided. The Antennas under consideration are planar and make use of slots in the middle where a nonlinear optical wave guide resides as described in the previous chapter.

The electro-optical modulation takes effect via direct incident millimeter wave radiation. The enhanced field within the slot is directly proportional to the modulation efficiency and sensitivity of the modulator. Therefore, an optimum antenna design with as large as possible field enhancement (FE) within the slot is key. As noted, the field enhancement within the antenna slots is one of the main parameters in determining the EOM performance. A few possible antenna candidates for this purpose are shown in figure 4-1.

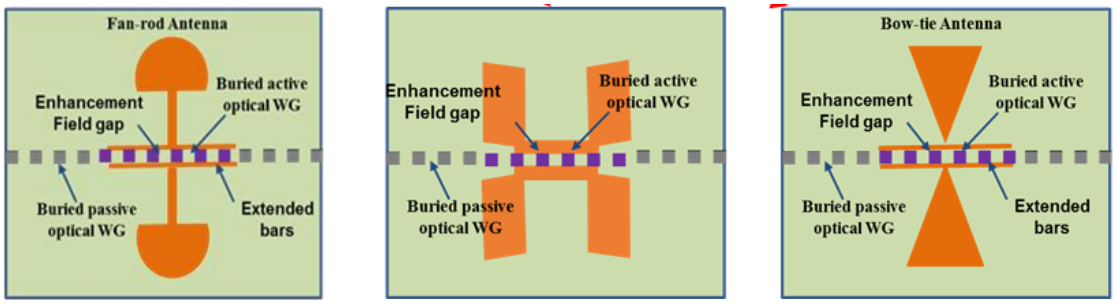

Figure 4.1. Planar dipole antennas candidates for antenna integrated EOM. Planar dipole like

4.2 HIGH FIELD ENHANCEMENT ANTENNA DESIGN

Antenna coupled electro-optical modulator does not have any physical electrical connection. Planar printed antennas on substrates are mainly monopoles and dipoles. For the application considered in this research, a dipole-like type is most suitable. Its convenience lays in its field gap between its structure. For this research we have identified two types of dipole like antenna: A bow-tie microstrip antenna and a microstrip patch. They can both be modified to accommodate the optical travelling wave in the active section of the electro-optic modulator by introducing a gap in the middle of the patch and introduce two bars to the bowtie antenna to extend the field along the active region of the electro-optic modulator along the modulation path. With emphasis on the field enhancement.

Both antennas type will be evaluated in conjunction with EO phase modulator design for an optimum performance with an emphasis of the field enhancement, gain and bandwidth for best EO modulation performance. The modification to these antennas is also similar, it involves adding extended bars at their apex that have the same length as the active portion of the electro-optical modulator to provide uniform field intensity along the modulation propagation path. These bars will also provide and allow for an additional

degree of freedom for tuning and optimization. The gap between the capacitive bars is an optimizing and design parameter affecting electrical field enhancement, necessary for efficient modulation and sensitivity. It is worthwhile mentioning that for this topology, there will be no external electrical connection and the bowties antenna arms can be used as poling electrodes.

These antennas, when integrated onto EO modulator do not make use of a direct feed port as in the conventional antenna structures. Therefore, conventional design methodology will not yield accurate results since the presence of a feed port is an integral part of the antenna and influences performance and impedance matching. Further, traditional formulas only give an approximate value of antenna dimensions for a given resonant frequency and deviations is exacerbated at millimeter wave. A new design procedure is therefore warranted. We have devised a design procedure that does not require a directly connected feed to antenna. The procedure uses a TEM waveguide approach to determine patch dimensions, followed by Eigen Mode analysis to observe the resultant resonant frequencies for verification. Results show, even in the absence of a feed line an optimum field enhancement can be obtained while controlling the topology of the antenna design such as the slot gap width and length. Results also show that the Field Enhancement within the slot is directly affected by the antenna gain and efficiency.

4.2 PLANAR ANTENNA DESIGN PROCEDURE OPTIMIZED FOR HIGH FIELD ENHANCEMENT

The devised design procedure that does not require a directly connected feed to the antenna takes on a Floquet waveguide approach to determine patch dimensions, followed

by Eigen Mode analysis to observe the resultant resonant frequencies for verification. The procedural steps are summarized below. Note that this procedure is similar for both types of antennas considered shown in figure 4.2.

I. Determine antenna dimensions

For a predetermined substrate height and material characteristics, as an initial estimate, Microstrip patch is sized to resonate at the desired frequency using available standard closed form formulas.

- Design a waveguide with opposing side pairs to be PEC & PMC such that it allows:
- TEM mode propagation
- Plane wave (377Ohms) interface to the waveguide.
- The structure allows for S-parameter computation and phase information
- Sized MS patch antenna and associated substrate are inserted into the waveguide to compute the resonant frequency by observing the reflected phase from the surface of the patch.
- To accomplish this, the wave port is de-embedded to the surface of the patch. Resonance frequency corresponds to where the reflected phase is zero.
- Introduce a narrow split in the patch to match the gap size needed, this will shift the resonant frequency to a higher value.
- Resize the patch to walk back the resonance frequency to its original/desired value.

Note: The waveguide height and PEC walls separation need be carefully determined as to make sure any TE and TM modes in the waveguide are decayed and cut-off

II. Determine antenna parameters

Once the slotted Microstrip antenna resonant dimensions are determined, the antenna parameter can be simulated by inserting it into a radiation box fed from the top using a plane wave port. The available simulation results using HFSS suite are Directivity, radiation pattern, bandwidth & enhancement factor (ratio of incident field to field in the slot).

III. Eigen modes Analysis

Perform Eigen mode analysis to check for proper resonant mode presence

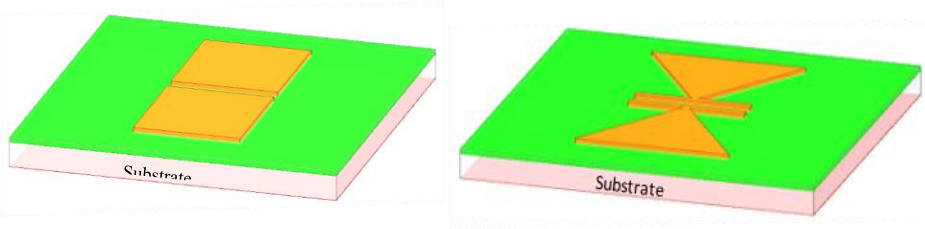

Figure 4.2. Slotted planar antennas used considered for EOM design. Patch antenna (left). Bowtie antenna (right)

4.2.1 Antenna design simulation for EOM integration.

One of the key challenges in the concept of directly integrating a planar patch antenna onto the EO modulator lay in the absence of a feed-port. Not only that the design has to have as large as possible field enhancement within the slot to promote modulation index, but also, a full a priori knowledge of antenna parameters, such as beamwidth, directivity etc. are required for the design of the sparse array. Based on the outlined antenna

design procedure outlined in this document, we investigated two antennas: a slotted patch and a plane bowtie, the material stack and dimensions and TEM waveguide mode setup for the design simulation are depicted in Figure 4-3. The heights of the materials in the simulated stack are analogous to the EOM design discussed in the previous chapter.

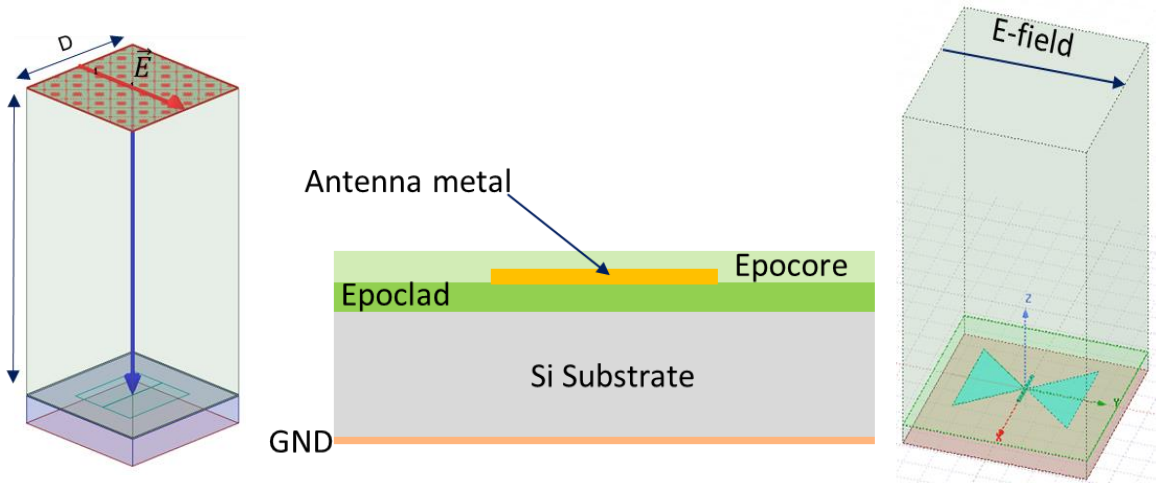

Figure 4.3. From left to right, slotted patch antenna TEM mode waveguide, material stack used in the simulation. Bowtie patch with extended bars TEM mode simulation setup

The following simulated results stem from the simulation procedure outlined in the previous section and use the material stack dimensions shown in Figure 3.8 and Figure 4.3 respectively. Starting from an initial estimate of the standard patch dimension (without a slot) a TEM wave guide is used to determine the final dimension at which the patch resonates. This is determined by de-embedding the port to the air and antenna structure interface and observing the reflected phase. The resonance occurs where the phase is zero.

For Initial antenna dimensioning as a starting point, standard literature formulas without a gap are used. These formulas predict resonance very well at low RF frequencies, but deviated substantiality at high frequency such as 94 GHz used. Therefore, for

verification purposes, both antennas without a gap under consideration are first simulated in the waveguide and found, as predicted, to deviates from dimensions calculated using closed form formulas.

Next, a six-micron gap is introduced to split the patch into two, while the overall dimensions are kept the same. This has the effect of shifting the resonant frequency higher than 94 GHz. The resonant frequency is then reduced by increasing the length of the patch and observing the reflected phase.

For the patch antenna, the simulation results are shown in Figure 4-4. The black curve reflects the initial dimensions after the introduction of 6-micron slot. The blue curve shows resonance after dimensioning. The insert in the figure represents the field intensity

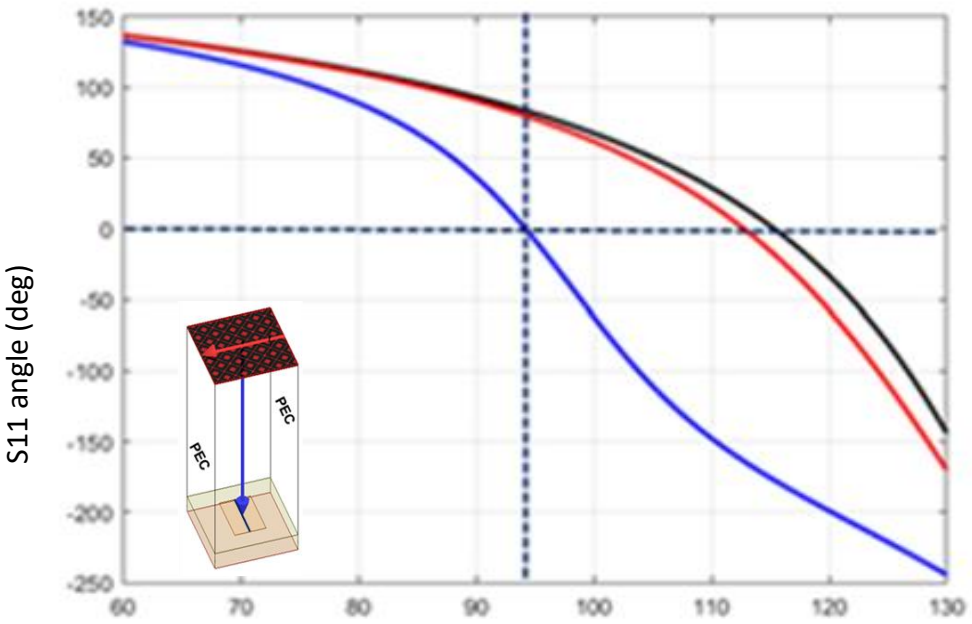

Figure 4-4. Simulated reflected S11 (angle) at the slot antenna for the resized slotted patch antenna (blue curve). reflected S11 prior re-dimensioning

profile confirming a resonant structure. The field enhancement along the slot is plotted Figure 4.5.

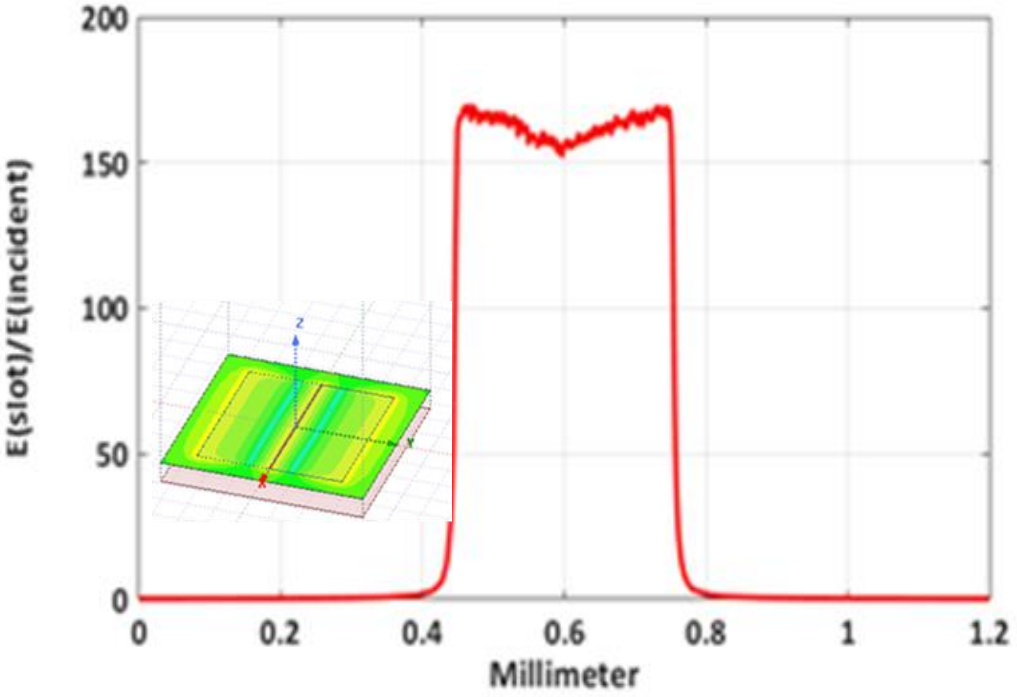

Figure 4-5. Field enhancement along the gap of the resonant patch antenna. The insert is the computed field profile

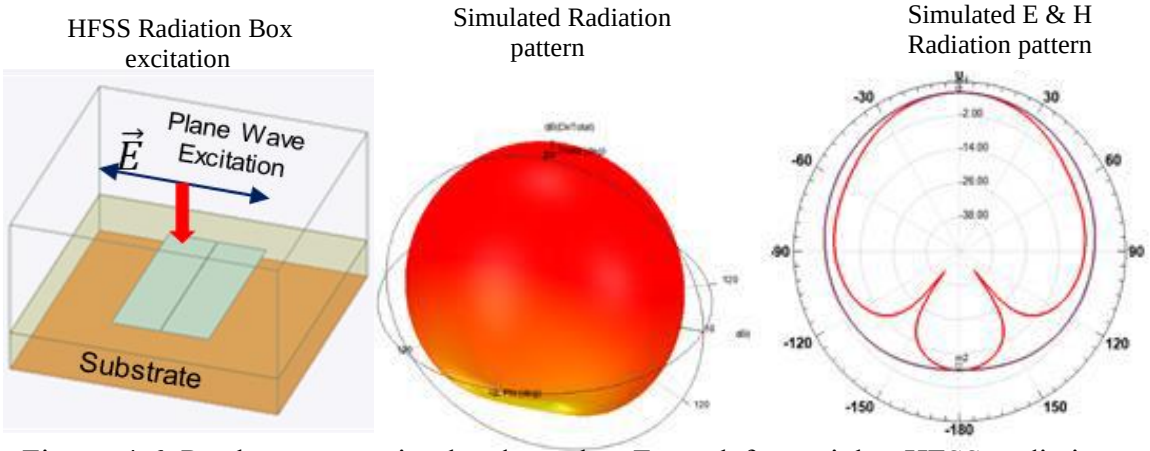

Figure 4-6 Patch antenna simulated results. From left to right: HFSS radiation boundaries and excitation setup, spherical radiation pattern and E & H fields Radiation patterns

Following the previously outlined procedure, the Once the slotted planar patch is dimensioned to resonate at 94 GHz, a full EM analysis is performed using HFSS suite to determine the remaining designed antenna figures of merit, such as directivity, radiation pattern and field enhancement within the created slot. The source in the simulation is a plane wave simulation. Figure 4-6 depict some of the most meaningful simulated results the slotted. The next as outlined in the design procedure is to perform modal analysis. Again, Ansys HFSS simulation suite is used.

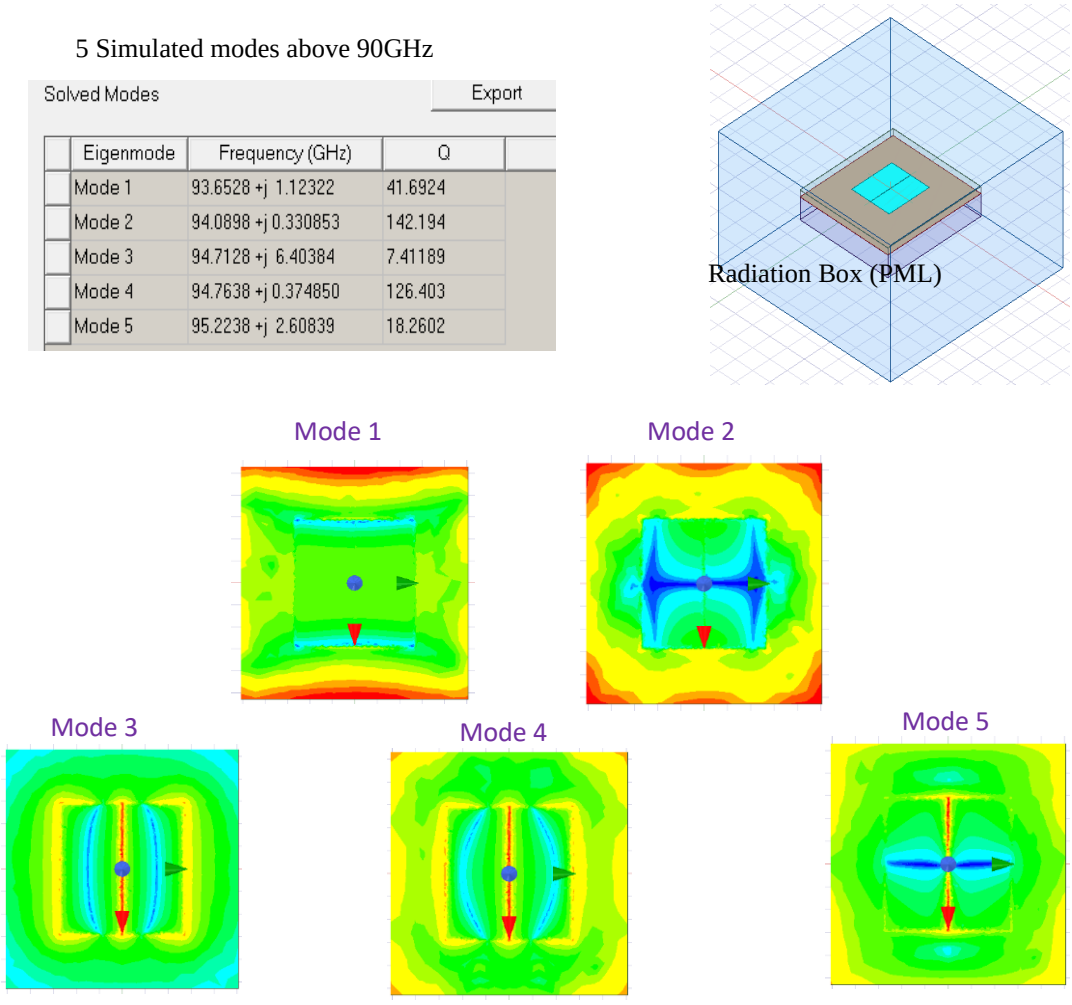

Figure 4-7. Patch antenna simulated modal analysis. Modes above 90 GHz and HFSS PML radiation boundary setup (top). Modes one to four electrical field plots.

Figure 4.7 summarizes the simulated results. Five modes are found at the vicinity of 94 GHz. Upon inspection of the shown field plots, mode number for looks to have the patch antenna behavior like.

For the above simulated patch antenna, the devised design procedure was carried out. Similar procedure was followed for the bowtie antenna. A notable difference is the added extended bars at the apex of the bowtie. The bars dimensions have the ability to tune the resonant frequency. This could be considered as a bonus as it adds another tunning degree of freedom. Figure 4-6 shows the sole effect of tuning using the extended bars length. Regardless, these bars are required to provide a uniform field withing the gap, along the path of the optical signal propagation. The simulated result for the bowtie antenna is shown in Figure 4-8, Figure 4-9 and Figure 4-10.

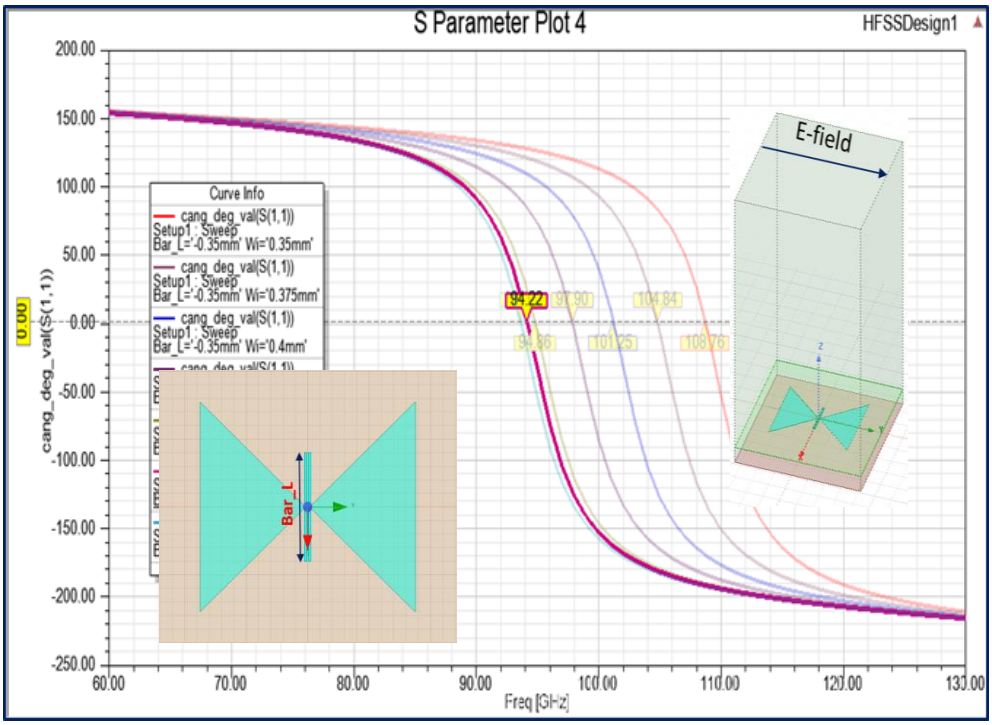

Figure 4-8. Simulated reflected S11 (angle) at the bowtie antenna. The faded curve shows the effect of the extended bars tunning effect.

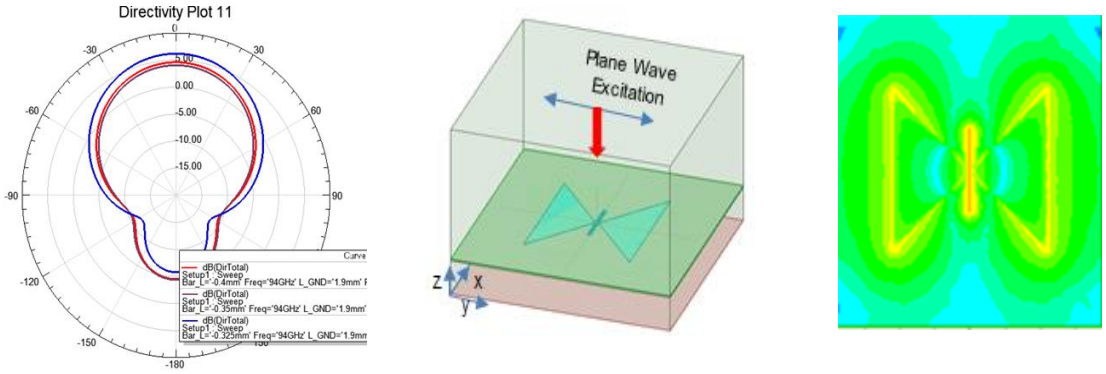

Figure 4-9. bowtie antenna simulated results. From left to right: directivity, HFSS plane wave radiation box setup and induced field on the antenna surface

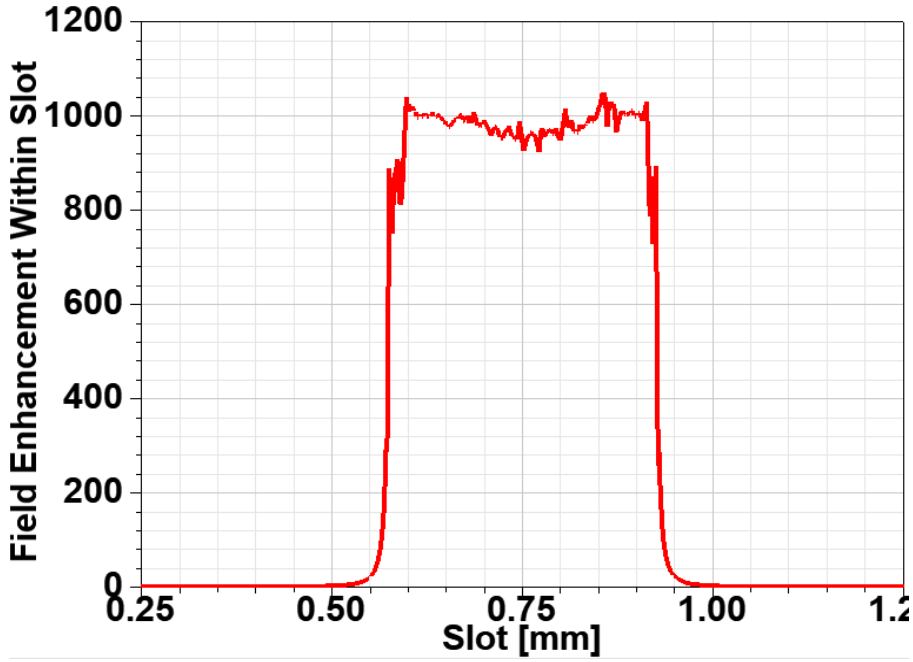

Figure 4-10. Bowtie antenna simulated field enhancement along the gap at resonance (94 GHz)

Like the patch antenna, mode analysis was performed for the bowtie. Five modes are found at the vicinity of 94 GHz. Upon inspection of the shown field plots, mode number four appears to have the patch antenna behavior like. The modes found are shown in Figure 4-11.

Eigenmode	Frequency (GHz)	Q
Mode 1	91.1096 +j 0.980760	46.4512
Mode 2	93.5404 +j 2.96866	15.7626
Mode 3	94.2897 +j 0.306921	153.607
Mode 4	94.3150 +j 2.66484	17.7033
Mode 5	96.1456 +j 0.551854	87.1129

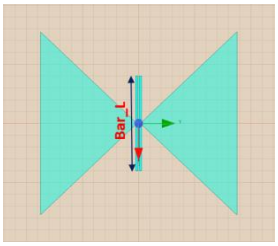

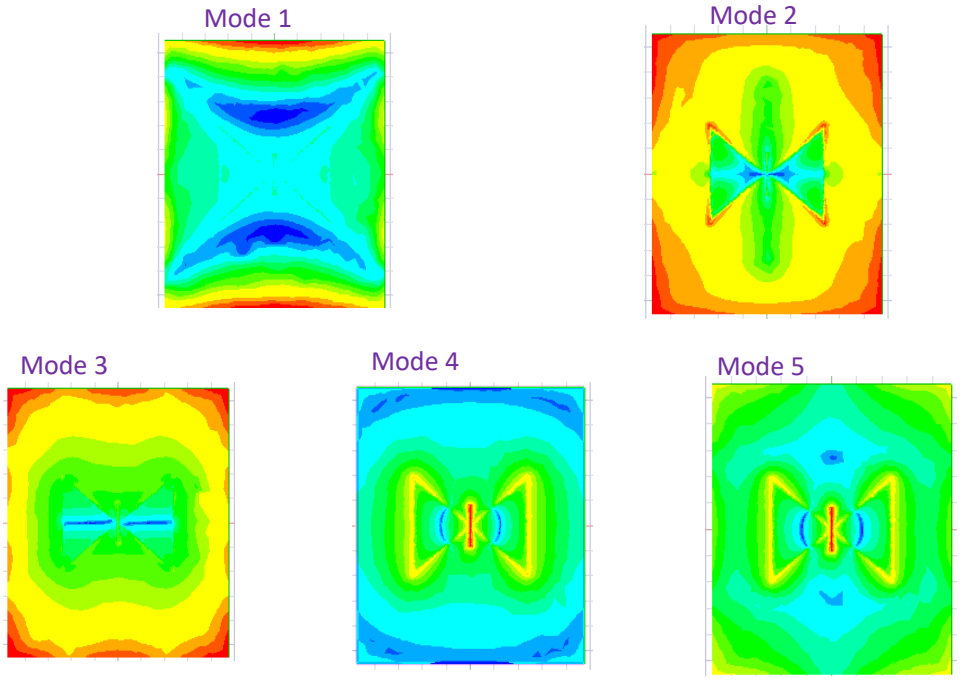

Figure 4.11. Bowtie antenna with extended bars modal analysis. Modes above 90 GHz and HFSS PML radiation boundary setup (top). Modes one to four electrical field plots.

4.2.2 Antenna design microfabrication and measurements

To further validate the antennas designs shown in Figure 4-2, and the devised procedure, both antennas were microfabricated using the same process described in chapter

3. However, since the antennas do not have a feed as designed. For functionality and verification purposes, a feed network was introduced and matched to the antenna impedance to accommodate the measuring testbench equipment. The microfabricated antennas were first probed using a W-band (75-110 GHz) probe setup to measure the return loss. Figure 4-12 and Figure 4-13 show the measured return loss (S11) for two different gap, 6 µm and 8 µm. This measurement as a first step was necessary as our anechoic chamber for radiation measurement is a 50 Ohm system. The increase in the slot gap, as predicted, has the effect of shift of resonant frequency to lower values. Also noted is that, as far as the return loss is concerned the measured results follow closely the simulated simulation. Following these measurements, we introduced these antennas to the anechoic chamber and produced a set of radiation patterns and gain measurements. Figure 4-14 shows the plot of the gain measurements.

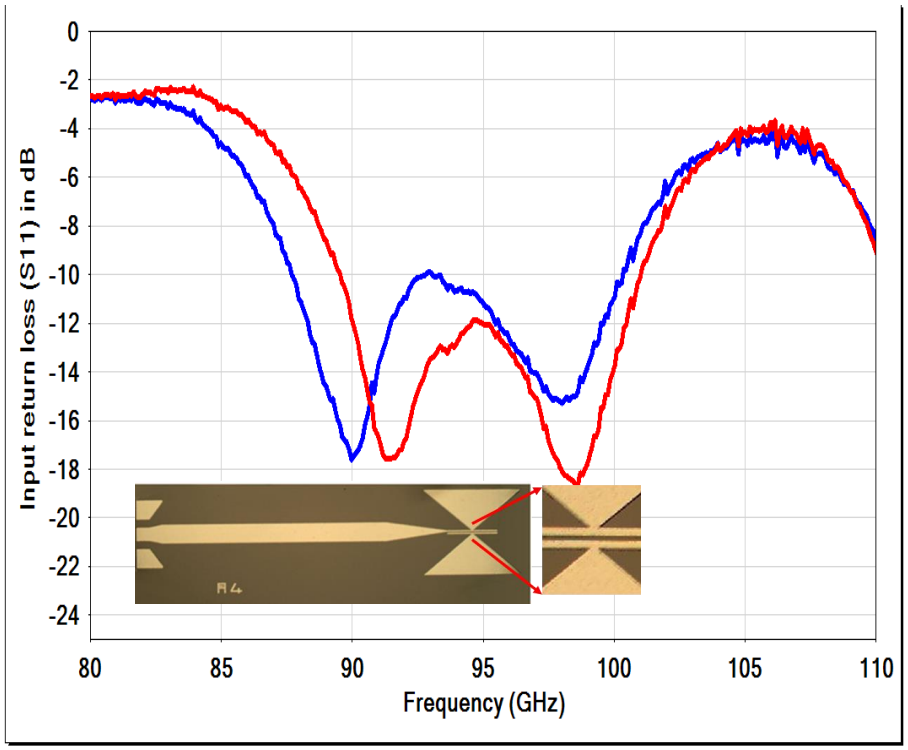

Figure 4-12. Measured return loss of the microfabricated antennas. For the bowtie antennas with 6 µm gap (red), 8 µm gap (blue)

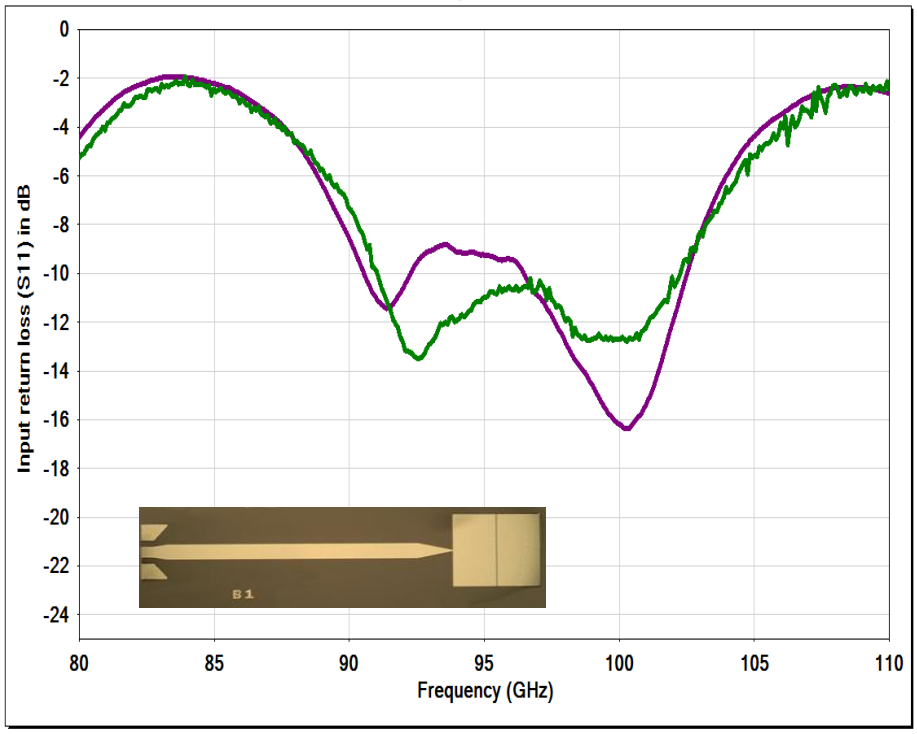

Figure 4-13. Measured return loss of the microfabricated antennas. For the patch antennas with 6 6 µm gap (green), 8 µm gap (purple)

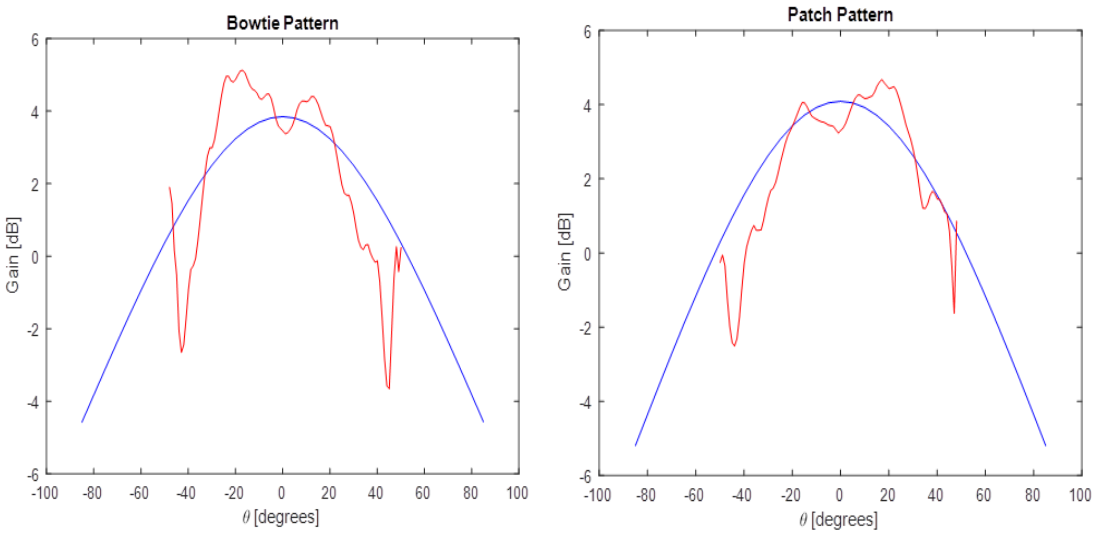

Figure 4-14 Simulated (in blue) and measured (in red) of Cartesian a radiation gain pattern for the microstrip bowtie (left) and slotted patch (right)

CHAPTER 5

PASSIVE MM-WAVE IMAGING USING OPTICAL UP-CONVERSION FRONT-END

5.1 INTRODUCTION

A passive mm-wave imaging system that can detect natural mm-wave block body radiation emissions can be used as standalone or fused with other imaging modality such as conventional IR imagery and LiDAR in degraded visibility and a host of other applications. In the optical up-conversion scheme of detection, an antenna integrated electro-optic (EO) modulator the received mm-wave signals and modulate an optical carrier. The optical carrier is then removed using an optical band pass filter, and the remaining sideband is projected onto a Near-IR camera. The antenna integrated EO modulator thereby eliminates active RF electronics in the front-end, requires only optical source and a photo detector.

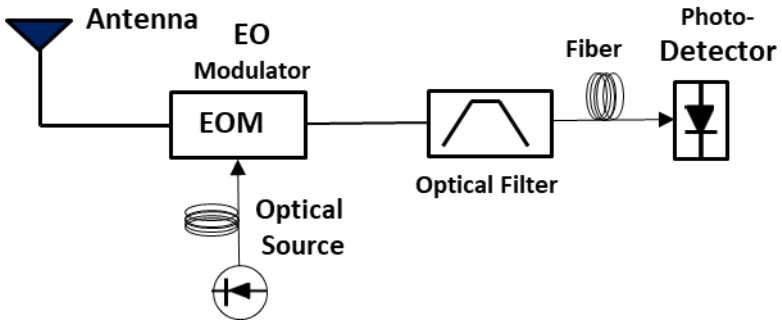

Figure 5-1. Unit cell performing optical up-conversion of a mm-wave signal used in simulation

This topology eliminates the need for bulky front-end lenses. The mm-Wave antenna integrated EO modulator has the potential to achieve high sensitivity at video rates, sub-1˚K temperature resolution, and broad field of view (>20˚) capability. For a front-end, in an array format, a unit detector cell block diagram is shown in Figure 5-1. This front-end unit

cell consists of an antenna integrated electro-optical modulator and an optical band pass filter fibers and a solid-state photo detector.

5.2 OVERALL PMMW IMAGING SYSTEM APPROACH

A PMWI operating at 94 GHz using sparse interferometric arrays is an alternative approach to realizing Passive Millimeter Wave Imaging Systems that have the potential to alleviate and overcome the challenges encountered in "all-electronic" and FPA imaging systems,. Each unit cell (see Figure 5-1) of the sparse array integrates an antenna, an Electro-Optic Modulator (EOM) and optical filter (to strip the optical carrier). This can be accomplished by direct conversion of 94 GHz radiation onto an optical domain carrier (common 1.55-micron laser), with a fiber bundle to transport the optical signal to an off-the-shelf commercially available NIR camera for image acquisition. Figure 5.2 is a schematic depiction of envisioned of such PMMW imaging system.

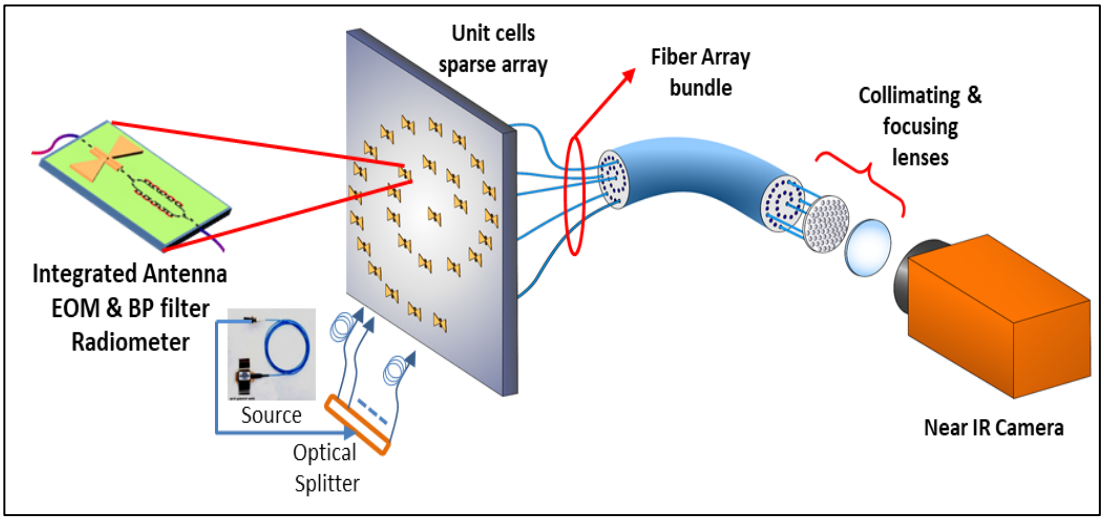

Figure 5-2. Schematic depiction of envisioned sparse pixel array PMWI system with optical up-conversion and sensing.

The envisioned integrated photonic chip eliminates the need of connectorized components which reduces overall system size and weight. It achieves high sensitivity at lower cost. Altogether, this approach enables a dramatic increase in sensitivity, integration density and versatility.

As noted earlier, directly driving an Electro-Optical Modulator from an integrated antenna provides an almost background-free measurement and high sensitivity. PMWI imaging systems based on optical up-conversion were first proposed by Blanchard and latter demonstrated to a certain extent by others [18]. The optical up-conversion scheme when applied in a passive millimeter wave imaging system has shown the potential to surpass "all-electronic" imaging systems in terms of performance, cost, and form factor. Their unique capabilities mean that they 1) remove the need for mechanical scanning, 2) do not require mm-wave optics, resulting in thinner, lighter-weight form factor over a standard FPA design, 3) provide greater sensitivity, eliminating the need for Low Noise Amplifiers (LNAs) and 4) can leverage existing and mature technology of NIR camera Read-Out Integrated Circuit (ROIC).

A high performance/efficiency EOM modulator with a single radiometric detector can theoretically achieve temperature detection resolution as low as ~20 milli-Kelvins. However, currently demonstrated PMWI systems with EO modulation [47,46] have so far failed to achieve the sensitivity performance required for successful video-rate mm-wave imaging at 94 GHz. This is because current systems primarily rely on connectorized discrete system components, both in the RF and optical signal chains, together with low performing EOMs. As a result, all demonstrated imagers so far have been forced to resort to amplification using LNAs to compensate for excessive losses to the impinging mm-wave

radiation. Conversely, the proposed approach is highly integrated, combining the mm-wave antenna, EOM, and optical signal conditioning into a single, modular chip. A single integrated pixel is depicted in Figure 5-3. The EOM design is of prime importance in this case and architecture. Especially in the passive imaging configuration. The sensitivity of the system is primarily set within the EOM by means of modulation efficiency and signal loss in the optical link.

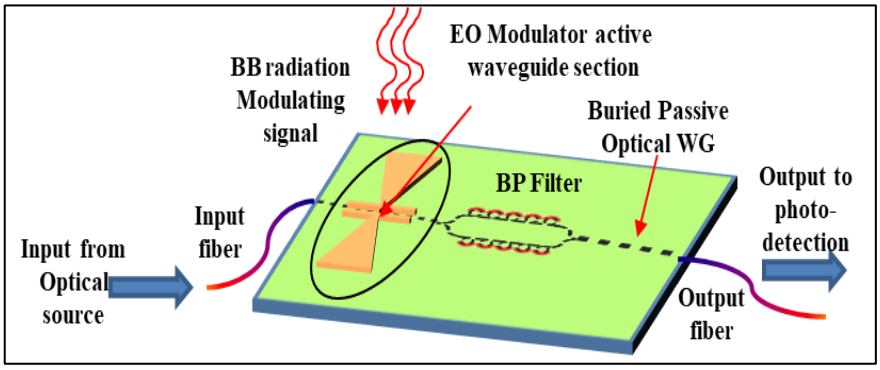

Figure 5-3. Envisioned integrated sparse array unit containing an antenna, EO modulator, optical filter & I/O fibers

5.3 PMMW IMAGING SYSTEM OVERVIEW

The Passive Millimeter-wave Imaging (PMWI) camera system under consideration will detect naturally emitted radiation at 94 GHz (one of the low absorption atmospheric windows), by encoding onto an optical signal source (such as the readily available 1550 nm laser) using an Electro-Optic (EO) phase modulator. Critically, by preserving phase of the collected energy, interferometric sparse array techniques can be leveraged to realize a large effective aperture with just a few individual detectors. This eliminates the need for large refractive lenses associated with FPAs and single scanning detectors. Simultaneously, the receiving antenna will be directly integrated onto the EO modulator such the one covered

in chapter 4. Thereby avoiding the inherently lossy transport from the antenna of the weak mm-Wave signal. This approach eliminates the need for demanding LNAs, LO, and supporting electronic networks, required by current systems.

Each detector detecting unit cell of the sparse array will be a photonic chip, which monolithically integrates the following components: high-efficiency 94 GHz antenna, a high performance EO phase modulator to perform up-conversion, and fiber pigtails for optical signals input and output (see Figure 5-3). These detector unit cells components are monolithically co-designed and integrated to shape a single channel that will form the basis of the overall integration of the front-end. The EO phase modulator design will use a large Pockels-effect EO polymer to achieve high efficiency and high speed. To further improve sensitivity and efficiency in the optical link, the EO polymer (responsible for modulation) is used only in the active region (where the phase modulation takes place) covered in chapter 4, while an off-the-shelf product, Ormocer, is used in the passive propagation of the optical link.

Using a sparse array architecture eliminates the need for large and bulky refractive lenses commonly found in Focal Plane Array and scanning systems, and substantially reduces cost and complexity by reducing the aperture pixel count. For a predefined spatial resolution, an optimum distribution of baseline (u-v coverage of the array) can be optimized to mitigate grating lobes that causes blurring. To optically reconstruct the image, a homothetic mapping of the output fiber array matching the antenna distribution, with scaling factor $(\boldsymbol{\lambda_{opt}/d}) \,/\, (\boldsymbol{\lambda_{rf}/D})$ where *d* and *D* are the fiber and antenna spacing respectively, will project collimated fiber signals onto a lens of an off-the shelf near-IR camera. Therefore by using a coherent interferometric distributed sparse array configuration, the system cell

leveraging optical up-conversion, paired with commercially available lenses and an Near-infrared (NIR) camera for detection, low form factor and low cost can be achieved.

In summary, a PMWI camera system, for detection of BB radiation centered at 94GHz, will be developed using a coherent interferometric distributed sparse array configuration. The system comprises a novel front-end unit cell leveraging optical up-conversion, paired with commercially available lenses and camera for detection.

5.4 PMMW IMAGING SYSTEM USING INTERFEROMETRIC SPARSE ARRAY

The fundamental theory behind aperture synthesis techniques has been in application for decades in radio astronomy [48]. It measures the correlation between the collected signals from antennas with overlapping fields of view to synthesize a virtual array having a much larger number of elements, and therefore greater spatial resolution. The under lying concept for real time image capture for the proposed PMWI camera system is an interferometric imaging array geometry using a distributed, sparsely populated, coherent aperture distribution in the front-end. In this way, the resolution of a large aperture is achieved by strategically covering the equivalent area with a much smaller number of elements. This approach will generate images in real time at a predefined spatial resolution determined by the largest baseline (largest antenna pairs spacing). The camera under consideration is a ‘staring’ array and avoids the need for scanning and focusing lenses in the front end.

The resolution of an interferometric imager is like that of a fully populated phased array. Therefore, the physical array can be made lighter, at lower cost and lower power than a full array. In essence the imager synthetically reproduces an image from several

correlation radiometers by cross correlating the outputs of each pair of antennas of the sparse array. This requires measuring amplitude and phase of each pixel detector of the array, followed by many complex correlators to recover the scene image. The conventional approach is depicted in Figure 5-4 (left). Where for which N number of sensors are required to have their detected power split N times (1xN power splitter) and N*(N-1)/2 complex correlators, followed by the large data processing step, which increases substantially in size and computing power. However, in the optical domain, as an alternative, the large amount of hardware and computations can be substituted using simple optical lenses and ROIC as shown in Figure 5-4 (right) (e.g. near-IR camera). Images are generated from the sparse modulators using typical optics and an array of detectors (e.g. commercial camera) to perform the spatial Fourier Transform of the sampled aperture at optical wavelength.

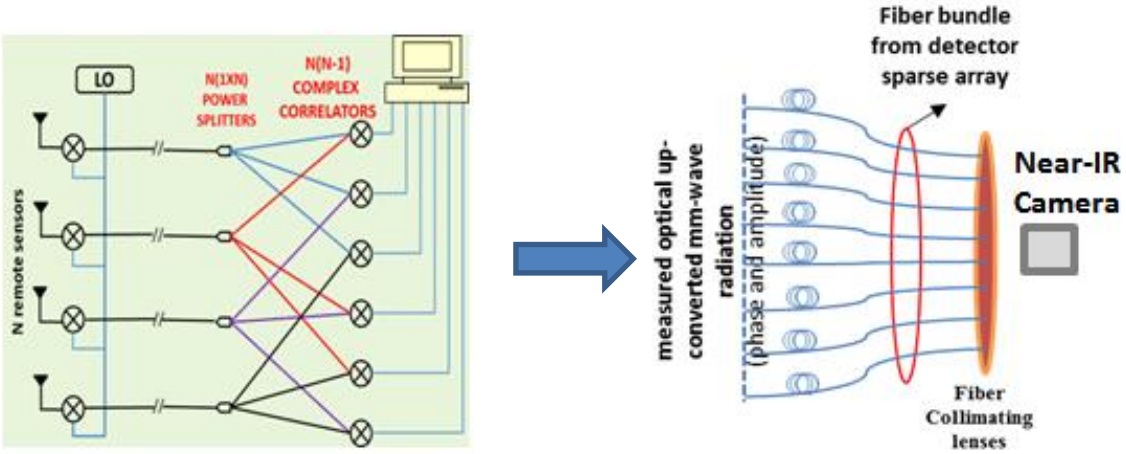

Figure 5-4. Synthetic aperture using power splitters and correlators engine (left). Using simple Fourier lens in optical domain (right).

The image quality of the proposed 2-D distributed aperture for interferometric imaging array is governed by the floor plan of the sampling antenna array. The method relies

on the relative spacing of antenna elements (baselines) to produce u-v coverage of the antenna array (sampling function). The visibility samples are determined by the spatial frequencies, which are in turn determined by the given antenna pair spacing. Therefore, the antenna geometry of the array plays a critical role in determining the effectiveness of the imager, and arrays should be designed such that the visibility function is well sampled and there is no break in the spatial frequency coverage. This implies that antennas in the array are uniformly incremented. Some popular sparse arrays and their u-v coverage are shown in Figure 5-5 [49].

Sparse array design layout for PMMW imaging is critical, the task is to find the minimum redundancy array, while maximizing sensitivity and resolution. Finding minimum redundancy in a linear array is strait forward and various algorithms exist for an optimum topology. However, in the case of a 2D planar array, finding minimum redundancy is not as simple, especially when the number of detectors is greater than 10. Four main sparse sampling configurations are: rectangular, hexagonal, circular, and non-uniform. These systems are application specific and the amount of detector and their spacing are wavelength and device size architecture limited, Judicious planning in all aspect of the system design is required. For example once the unit cell detector such the one discussed here, and the specs such field of view and desired spatial resolution is known, , one can proceed with the most appropriate configuration and optimize it to fit the backend camera specifications. In most case optimization code needs to be developed to generate an array configuration which will give maximum number of unique samples in the u-v plane and produces minimum grating lobes in the point spread function.

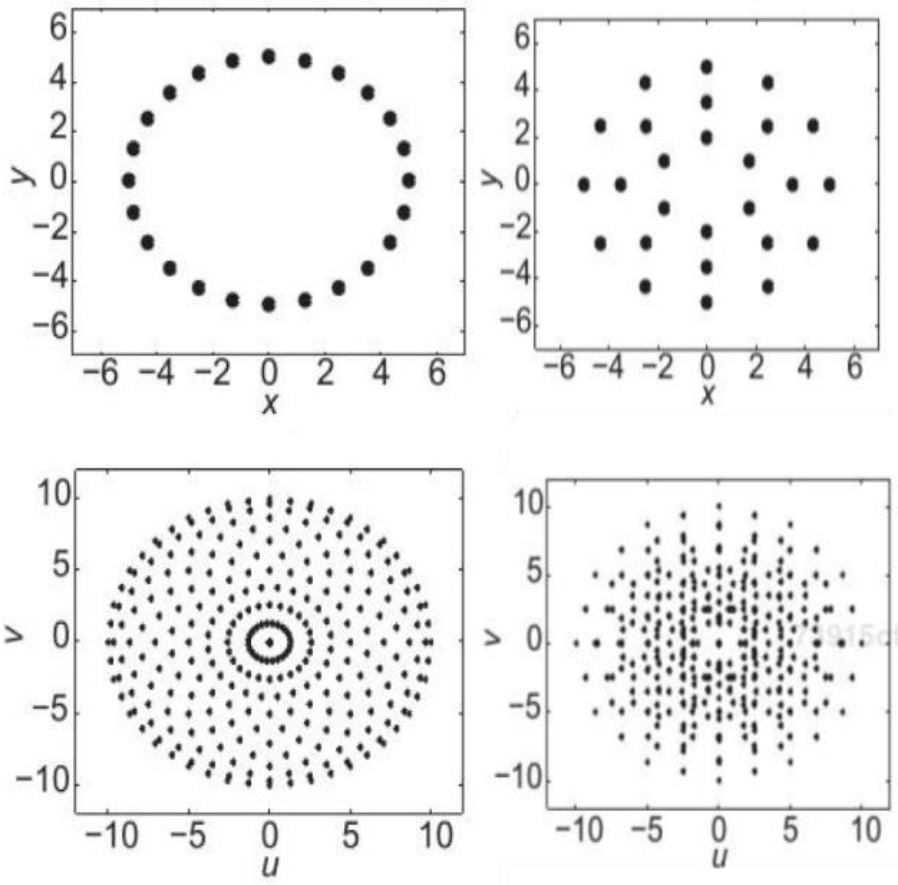

Figure 5-5. Variety of sparse array configurations (top) their corresponding spatial frequency coverage (bottom)

5.4.1 Sparse array Canonical point spread function

Imaging performance of the mm-Wave imaging camera system in sparse array configuration dependents on the design of the sparse array layout, which can be assessed through the Point Spread Function (PSF). The PSF defines the beam shape or diffraction limit of the aperture. Key parameters are the size of the main lobe, intensity of the side lobes, and presence of any grating lobes in the visible region, all of which can contribute to blurring, artifacts, and power loss in image generation.

Three canonical sparse array layouts are shown in Figure 5-6: the T-, circle, and Y-arrays. In each case we can see the physical layout of the antennas (left) is substantially sparse compared to a fully populated array. Auto-correlation of the physical layout produces the sampling function in the spatial frequency space (center), which acts as the "virtual" array and ultimately defines the performance of the array layout. Finally, the broadside PSF (right) is generated through Fourier transform of the sampling function, representing the beam pattern of the virtual array. As such a narrow main lobe of high sensitivity (light color) is desired in the center, with low sensitivity (dark) elsewhere. Regularly repeating arrays such as the T- and Y-arrays have grating lobes which appear in the UV plane, however for an appropriate element spacing, these can be pushed outside the visible region (e.g. circle of radius 1 in the UV plane for element spacing $\lambda/2$).

5.4.2 94 GHz System Simulation

To qualitatively, and quantitatively judge imaging performance (usually application specific) and usability for a given application, a system simulation is developed. It takes an infrared thermal image as ground truth and simulates the effects of the EO camera system at 94GHz, including element pattern, sensitivity, bandwidth, sparse array layout, and noise figure. The processing flow is summarized as:

1. Read IR image
2. Map to UV coordinates at target range
3. Generate array PSF
4. Apply element pattern
5. Convolve IR image with PSF
6. Integrate over element bandwidth

7. Inject noise and attenuation

8. Re-map to image coordinates

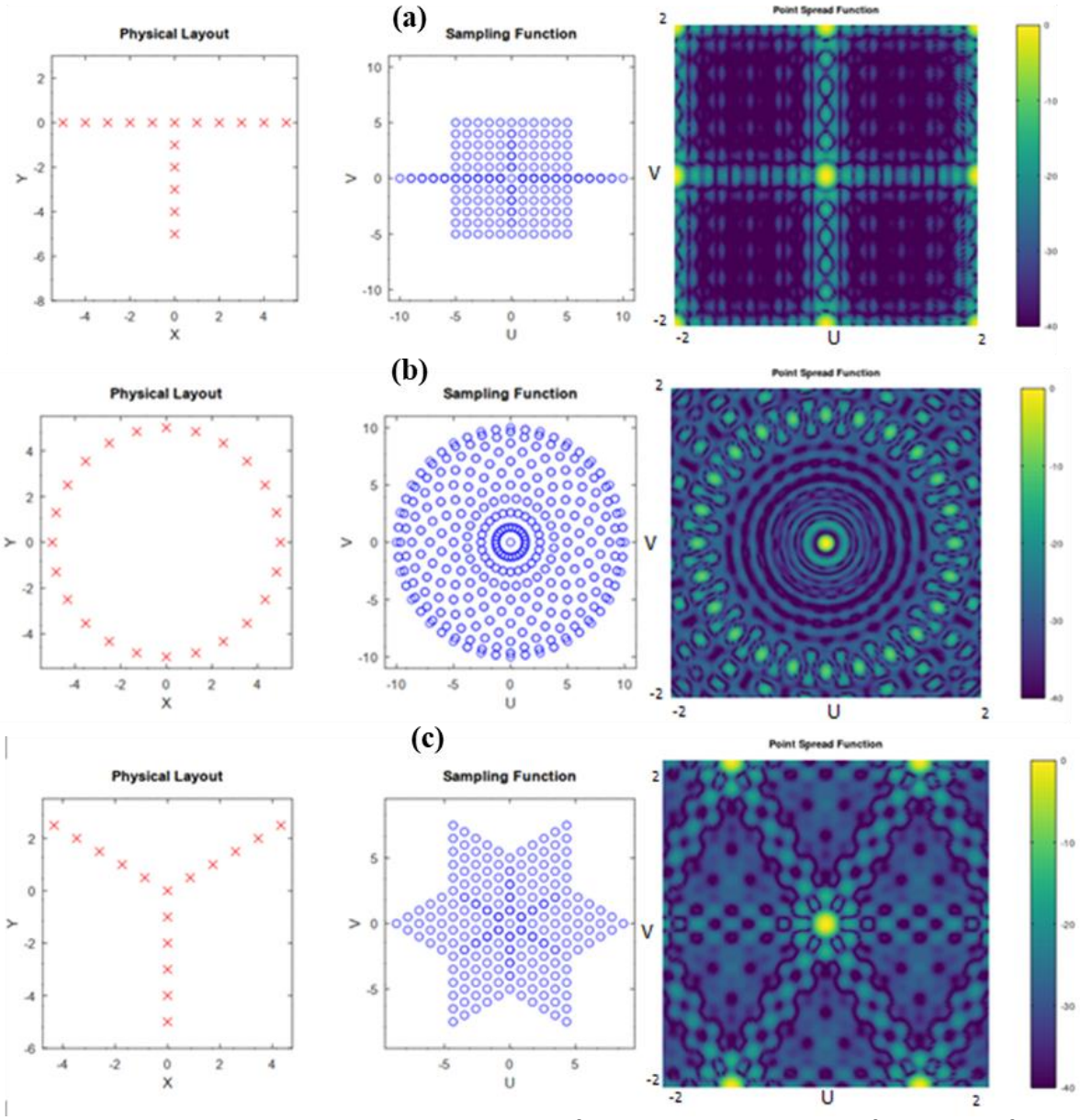

Figure 5-6. Physical antenna layout (left), spatial sampling function after autocorrelation (center), and resultant point spread function (right) of three canonical sparse array layouts. T-array (a), circle array (b), and Y-array (c) layouts are compared. PSF assumes λ/2 element spacing and is plotted beyond the visible region to include the first grating lobes.

The start and end points of the above simulation flow are shown in Figure 5-7. The simulation is modular, to allow measurement values to be inserted for any stage of processing.

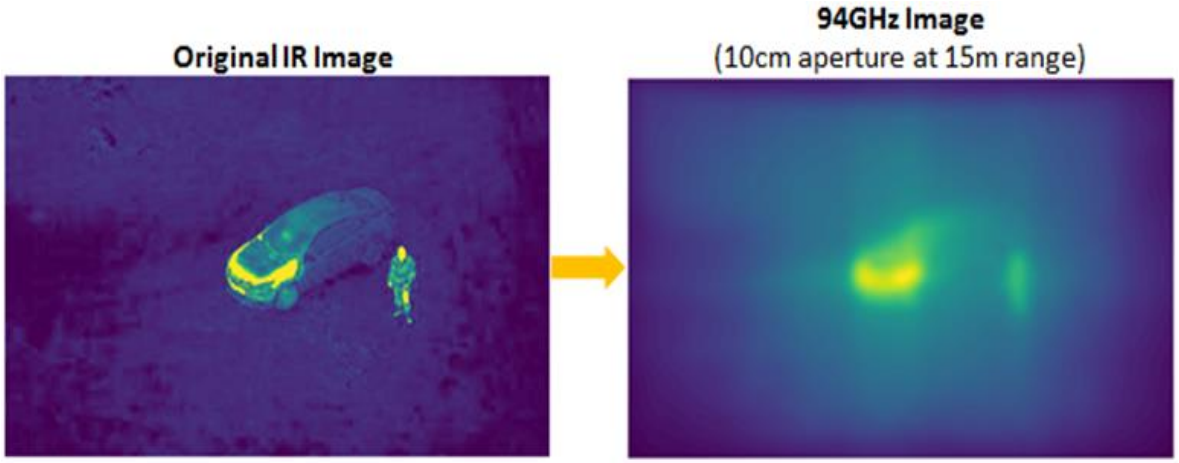

Figure 5-7. Infrared image (left) used as ground truth temperature data, and simulated 94GHz image of the same scene (right), based on a 10cm T-array at a 15m range from the scene. We note both shapes are detectable and distinguishable in the mm-Wave image.

Parametric analysis was carried out to determine the aperture size necessary to detect and/or distinguish objects in the scene at different ranges. 10 and 20 cm diameter apertures at 15 and 50m ranges are compared in Figure 5-9. Notably the 10cm aperture can detect 0.5m objects (approximate width of human target) out to 50m range, though distinction from other nearby objects or scene identification requires shorter range or the larger 20cm aperture, which shows good performance out to 50m.

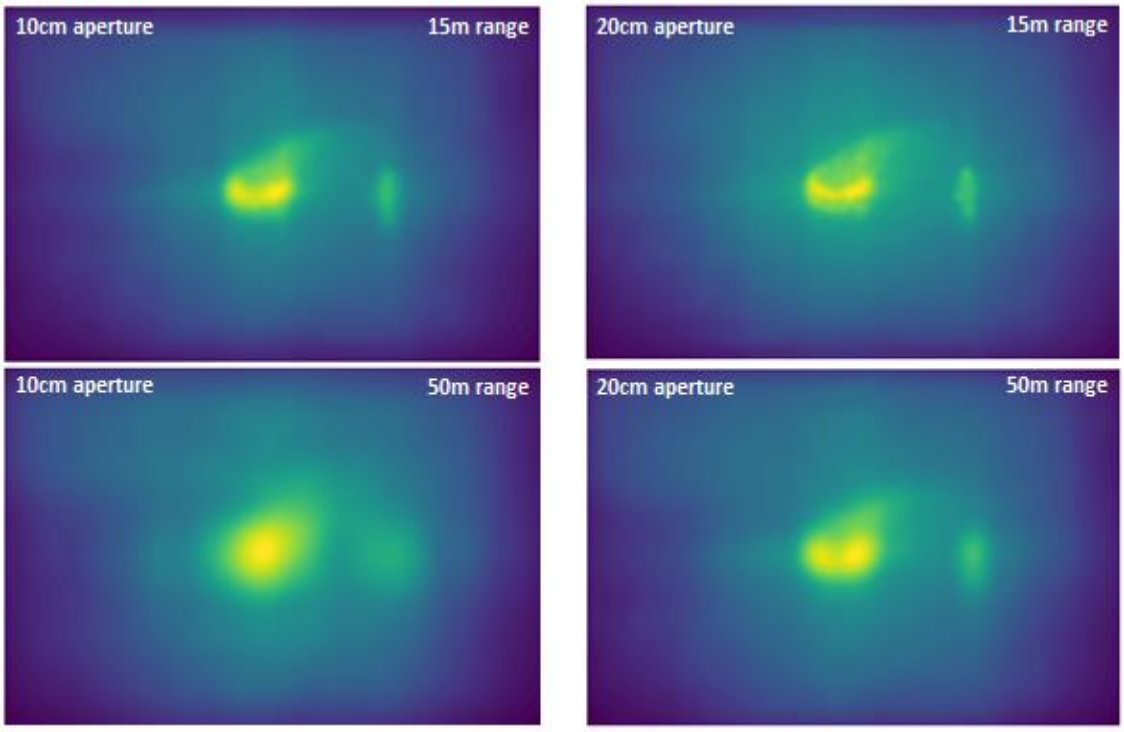

Figure 5-8. Comparison of simulated imaging performance of 10cm (left) and 20cm (right) sparse array apertures at 15m (top) and 50m (bottom) from the scene. The original temperature data is the same as Figure 5-7.

5.5 PMMW FEASIBILITY ANALYSIS & COMPUTATION

The EOM design and performance is of prime importance for PMWI systems using optical up-conversion, especially in the passive imaging configuration. The sensitivity of the system is set within the EOM by means of modulation efficiency and signal loss in the optical link. It is also the driving requirement that determines whether an amplification using a low noise amplifier is required. The analysis through evaluations by simulation and validation of the microfabrication process (described in chapter 4) of the detector unit cell shown in figure 5-9. This unit cell represents and will eventually perform as a single element of a sparsely distributed front-end, lens-less millimeter wave imaging system.

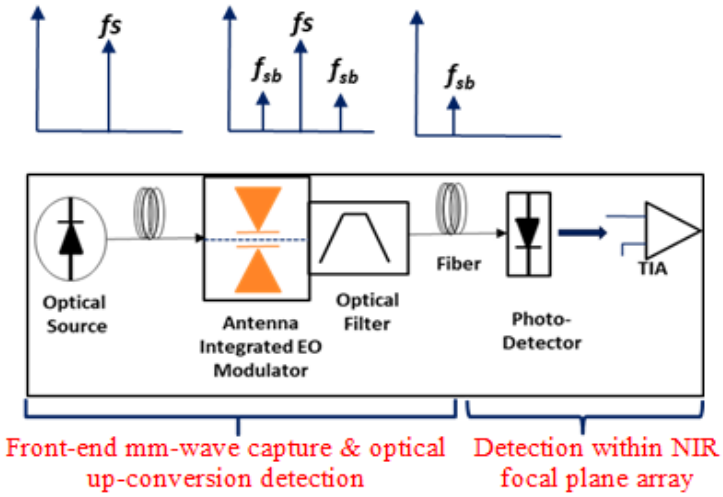

Figure 5-9. sparse array unit detector cell model functional diagram

As described earlier, its functionality is somewhat identical to the architecture used in all RF systems with the distinction that the radiated signals received by the antenna are up-converted and processed in the optical domain. For each unit cell of the array, blackbody (BB) radiation seen by the antenna modulates an optical signal source, such as a laser operating at one of the communication frequencies or at Near-Infrared (NIR). Here, a 1550nm optical source and 94 GHz antenna. The choice of 94 GHz is based on atmospheric absorption, increased thermal radiation power and most importantly the increased distance (in wavelength) from the carrier to side bands to alleviates the optical filter requirement.

The output of the modulator has the original optical signal source and sidebands offset from the optical carrier frequency by the antenna resonant frequency (e.g. $f_{opt} \pm f_{mmW}$). After modulation an optical filter is used to single out the optical sideband carrying the millimeter wave signal. This first sideband is then transmitted via an optical waveguide or fiber to a low noise and high-quality photodetector its relative intensity is measured.

Figure 5-9 illustrates the functional block diagram and frequency domain signal representation along the different stages of the signal path. The optical power in the immediate side band can be expressed as:

$$I_{SB} = I_{OP} I_{MM} \eta_{MOD} L_{OP} \tag{5.1}$$

Where, $I_{OP,}$ $I_{MM,}$ η_{MOD} and L_{OP} are power in the optical carrier, millimeter wave power, efficiency of the EOM and loss in the optical link, respectively. Also of interest is the signal current generated from the side band that can be expressed as:

$$i_s = I_{SB} L_T R = \eta DET I_{MM} \tag{5.2}$$

where R is the responsivity of the photo detector and η_{DET} is the efficiency of the photo detector. Note that, for our overall imaging system the detector and the transimpedance amplifier are an integral part of focal plane array and the read-out-circuit (ROIC). For our analysis we use values available for components that are off-the-shelf, discrete, and by no means state of the art components. The intensity in the optical side band is calculated based on the carrier to signal ratio (CRS), based on the modulation depth [9] m and the computed block body radiation from a 300° K source of radius 0.5m that is 33 feet away.

$$m = \frac{\pi\left(\sqrt{2ZP_D A_e}\right)}{V_\pi} \tag{5.3}$$

$$CSR = 4/m^2 \tag{5.4}$$

Where P_D, Z , A_e are the incident mm-Wave power, antenna impedance, and effective designed antenna area, respectively. The constant V_π is the designed EOM modulator efficiency, conservatively evaluated to be 13.9 V and is based on the electro-optic material properties and the physical dimensions of the antenna. Note that the antenna design is optimized to have an optimum field enhancement within the active modulator slot (factor 1000 is used in the computation) that that can be considered as an electrical field gain, which contributes to the modulation depth and efficiency. The computed black body radiation at the antenna mentioned above is for a bandwidth of 15GHz and is approximately $0.3\text{x}10^{-8}$ W. The evaluated modulation depth and the CSR is $0.3\text{x}10^{-8}$ and 76dB respectively. From equation (4) the intensity in the side band can now be evaluated for the incident radiation power and chosen laser source. Assuming a ~15 dBm laser power and a CSR of 76 dB, the power intensity in the side band is evaluated to be $0.8\text{x}10^{-9}$ Watts (-61dBm), and modulator efficiency of 1.1 W^{-1}. Table 5-1 and Figure 5-10 summarize the evaluated antenna integrated EOM.

Table 5-1. Evaluated EOM parameters

Var.	Val.	Description
I_{sb}	$8\text{x}10^{-10}$ Watts	Optical power in the side band
I_{mm}	$0.3\text{x}10^{-8}$ Watt	Incident mm-wave incident radiation
I_{op}	~$25\text{x}10^{-3}$ Watt	Incident mm-wave incident radiation
η_{mod}	1.1 /watt	Modulator Efficiency
CSR	76dB	Carrier to side band ratio

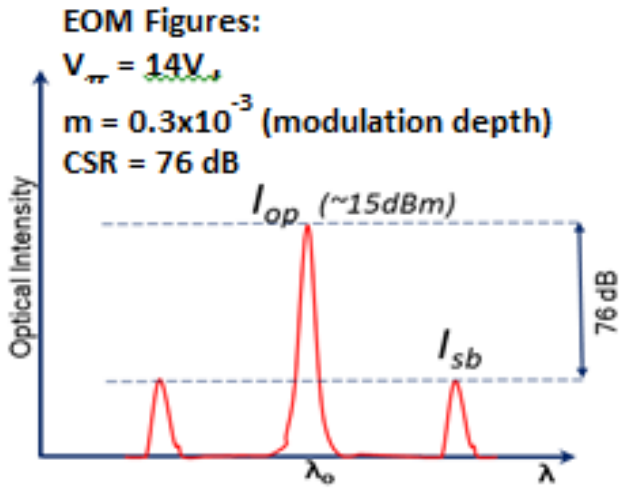

Figure 5-10. Predicted antenna integrated performance

The generated photo-current for a given photodetector can be readily evaluated using equation (5-2). Typical photodetectors for 1550 nm wavelength use InGaAs detectors. Typical standard off-the–shelf responsivity and dark current at room temperature for this type of detector is around 1 A/W and 1 nano-ampere respectively. To further improve their performance, they can be cooled thermoelectrically or cryogenically for even better performance. These values are by no means state of the art; SWIR FPA/ROIC cameras are mature technology and ultra-sensitive detectors are available. Nevertheless, for an input laser power of 15 dBm producing a side band power of 8x10^{-9} Watt, a standard NIR detector will generate a photo-current signal that is equal to ~9 nanoamps, which is beyond the dark current of the detector.

To further analyze our performance, we compute the Noise Equivalent Temperature Difference (NETD) of one cell (shown in Figure 5-9), to determine the necessary detector efficiency (when detection scheme within the FPA/ROIC is photodetector plus transimpedance amplifier). NETD is a measure for how well a thermal imaging detector is able to distinguish between very small differences in thermal radiation in the image. i.e.,

Thermal Contrast. NETD is evaluated based on the System SNR and NEP (Noise Equivalent Power). When the sensitivity limit is thermal noise limited, it is expressed as:

$$NETD = \sqrt{\frac{4TBW_d}{kG_{TIA}\,BW_r^2\eta_d^2}} \tag{5.4}$$

Table 5-2 lists the used the values used in the computation of NETD. Figure 5-11 shows the simulated 1° Kelvin NETD and required detector IR camera efficiency and bandwidth for two different sensor temperatures, 250 and 300 Kelvin. This computation is useful for the tradeoff of camera choice and the front-end performance. We note that off-the-shelf cameras with detection efficiency of ~0.05 are readily available; also available in the market are TE cooled cameras for low thermal noise and sensitivity.

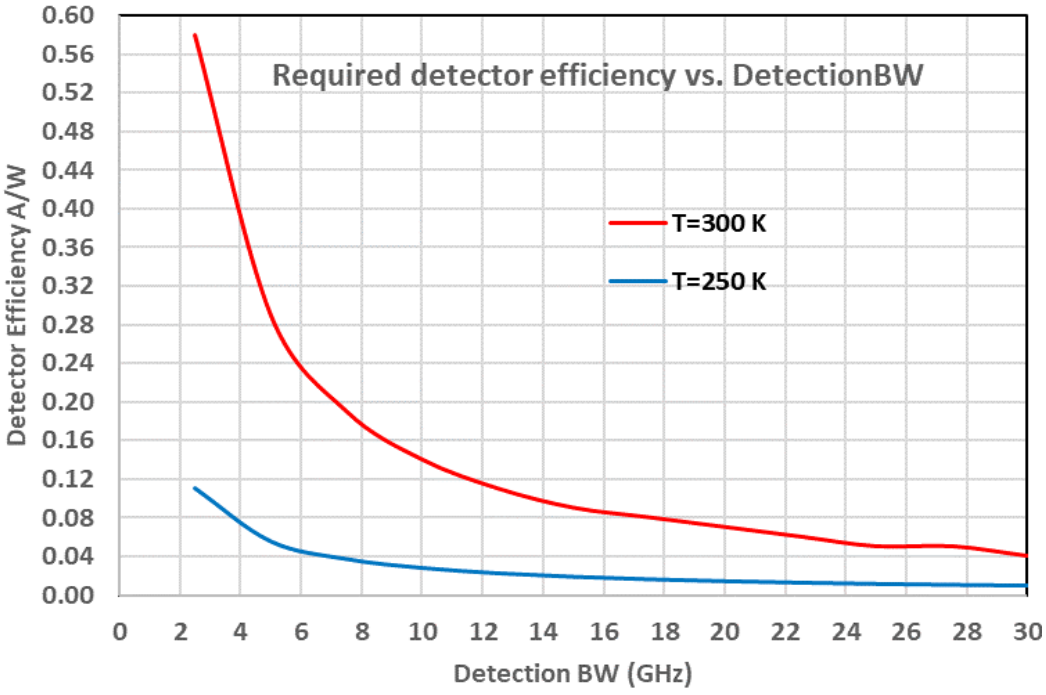

Figure 5-11. Computed required detection efficiency as a function of receiver bandwidth for 1 Kelvin NETD

Table 5-2. Used value for NETD computation

Temperature	300K	250K
Refresh rate	100Hz	100Hz
TIA gain	10G Ohms	10G Ohms
Receiver BW	15GHz	15GHz
FPA Det. Eff	0.095 A/W	0.009 A/W
Sensitivity limit	1K	1K

5.6 SUITABLE OPTICAL FILTER

The output of the antenna integrated phase modulator consists of the original optical source and its sidebands where the detected radiation is encoded. Extracting the desired signal at the output of the EO modulator for detection and imaging involves singling out one of the sidebands and suppressing the rest using an optical filter. For the type of imaging system considered here a bandpass design using micro-ring resonator can be used and integrated onto the photonic chip (EOM). One elegant design is an all-pass-sum-difference topology shown in Figure 5-12, where micro ring resonators are integrated into a Mach-

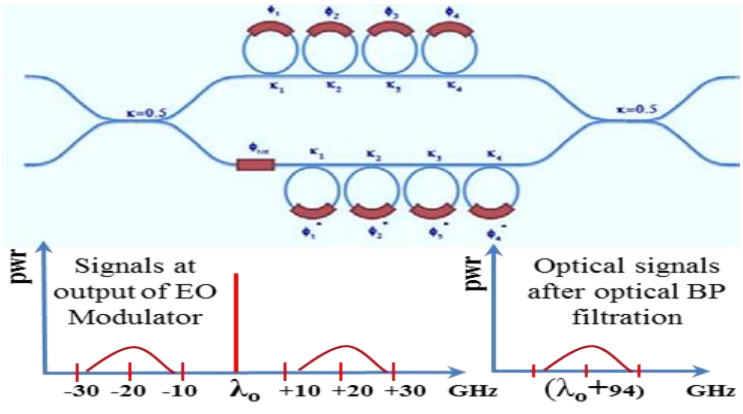

Figure 5-12. Optical filter using all-pass-sum-diff., micro ring resonators integrated into a MZ interferometer

Zehnder interferometer. The number of resonators used, and their size would depend on desired performance and the required suppression. This design of the bandpass filter could be integrated with optical modulator in a planar fashion on the same substrate.

Another way to get rid of the laser line is to use wavelength division multiplexing techniques (WDM). On-chip arrayed waveguide gratings (AWGs) or Echelle gratings are widely used for this purpose. Since AWGs are stronger in terms of resolution, using a high order AWG is a viable solution for filtering out the input laser [50] carrier. The AWGs are on chip devices and can be designed on specific waveguide structures.

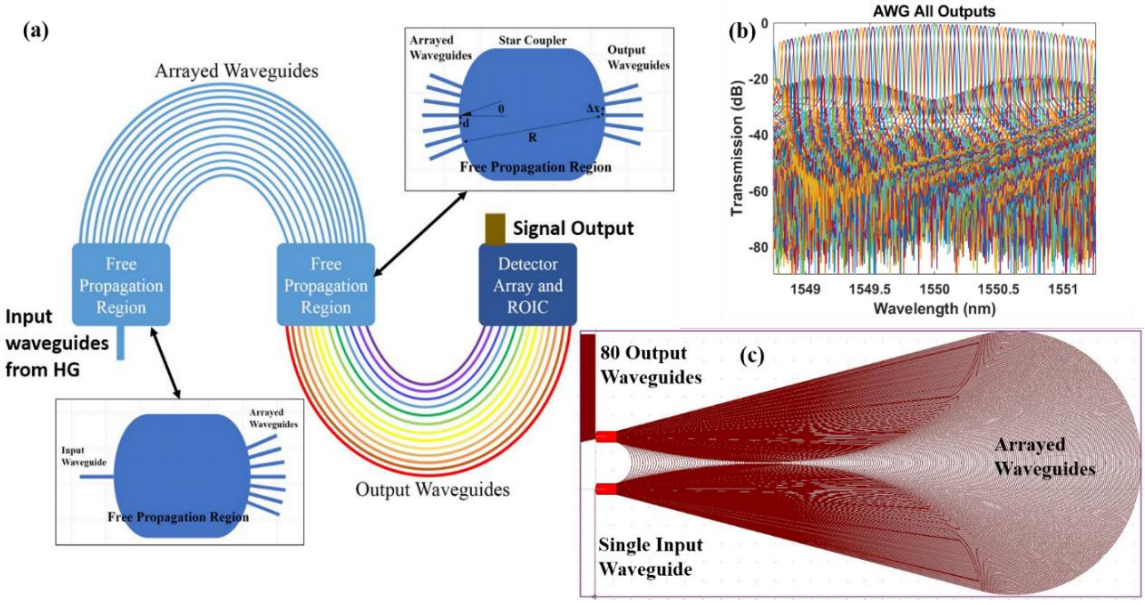

Figure 5-13. (a) The schematic of on-chip AWG. (b) Transmission of the AWG designed for the project with high resolution. (c) Layout image of the AWG

In AWG demultiplexers, phase difference is provided by individual waveguides carrying input light as seen in Figure 5-13. An AWG system consists of multiple photonic

integrated circuit (PIC) elements; input and output waveguides, two focusing slab waveguides (free propagation regions), and arrayed waveguides with a constantly changing optical path length difference ΔL between the adjacent waveguides. The operation of an AWG is as follows; light from an input waveguide diverges in the first free propagation region (FPR) and illuminates the input facets of an array of waveguides with a linearly increasing length. The phase difference at the output facets of adjacent array waveguides is an integer multiple of 2π for a central design wavelength λ_c. Since these facets are arranged on a circle, a cylindrical shape wavefront is formed at the beginning of the second FPR, which generates a focal spot at the central output waveguide. The phase shift caused by the length differences between the arrayed waveguides is linearly dependent on wavelength, the resulting wavelength dependent phase gradient implies a tilt of the cylindrical wavefront at the beginning of the second free propagation region, which causes the focal spot to shift to a different output waveguide with wavelength. The detailed list of design parameters of AWG spectrometers is given in [51].

$$m\,\lambda = n_s\,d\,\sin\theta_i + n_s\,d\,\sin\theta_d + n_c\,\Delta L \qquad (1)$$

where n_s is the effective refractive index of the slab region, n_c is the effective refractive index of the array waveguides, ΔL is the length difference between two adjacent waveguides in the grating, d is the separation between the array waveguides, Δx is the focal point deviation in the imaging plane from its central position (also known as the separation between output waveguides), R is the slab radius, m is the grating order, i and j are the number of the input and output waveguides, respectively, θ_i is the angle of the far-field diffracted light cone of the input waveguide, and is q_o the acceptance angle of one of the output waveguides, and λ is the wavelength.

To achieve filtering of the laser line, the AWG outputs designed for this purpose have to be removed. The design center wavelength of the AWG is the 1550 nm laser line. So, the center output waveguides will come across to the laser line. If the center output waveguides are removed, the laser will be transmitted from the FPR surface and couple to free space and leave the device. Meanwhile, the side outputs will coincide with the sidebands that are generated with the nonlinear process. This process is shown in Figure 5-14 with corresponding outputs and transmissions. Thus, filtering can be achieved by this method. The output sideband can be effectively combined with an MMI coupler to double the amount of the signal output of the device.

CHAPTER 6

CONCLUSION AND FUTURE WORK

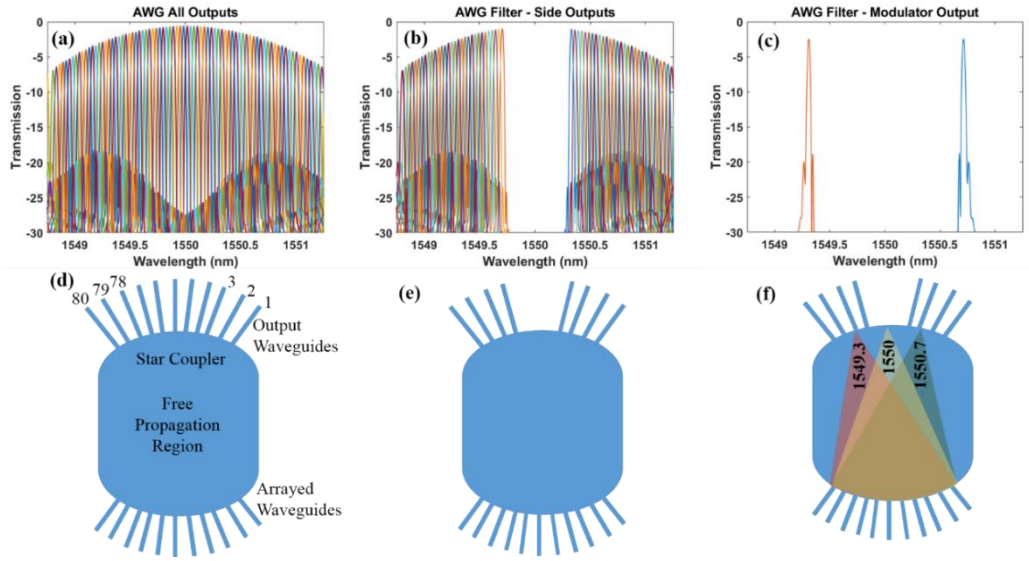

Figure 5-14. (a) Transmission of the designed AWG from all 80 outputs. (b) Transmission of the AWG from 25 on one side and 25 on the other side waveguides. (c) Transmission of the designed AWG from input signal carrying 3 wavelengths, laser line in the middle and 2 side bands. (d) Schematic of the output waveguides where all outputs are available. (e) Schematic of the output waveguides where only side outputs are available. (f) Schematic of the output waveguides where side outputs are available, and the input signal is in the device carrying 1549.3 nm, 1550nm and 1550.7 nm.

6.1 CONCLUDING SUMMARY

Millimeter-waves (mm-Wave) have the unique property to penetrate dielectrics, clothing, thin walls, and to overcome atmospheric obscuration such as dust, fog, and rain. Therefore, imaging at the millimeter wave frequencies is attractive, if not an essential modality for public security and intelligence gathering applications, and a host of other applications in the medical and scientific fields.

The research presented herein is multi-disciplinary; it involved many areas of science and engineering. These areas are mainly:

The research presented herein is multi-disciplinary; it involved many areas of science and engineering. These areas are mainly:

- Optical and Electro-optic devices engineering
- Millimeter-wave antenna design
- Organic polymer chemical engineering and associated microfabrication processes and characterization
- Radiometric detection and imaging system modeling, analysis, integration, and characterization
- Beamforming and sparse array interferometric imaging.

This effort focused on the successful integration of novel apertures, sensors, and imaging technologies to achieve a new class of remote and passive sensing at millimeter waves (94 GHz). It provides a broadly needed sensor system that has the potential to replace bulky millimeter wave imaging systems such as the one encountered at airports and other security checkpoints. In essence, the proposed imaging camera system will sense passive mm-Wave radiation from the body, encode it onto an optical signal for prost-processing,

and for subsequent image capture as done by IR or optical cameras. For the front-end of the proposed camera, we propose a unique design and architecture that introduces an antenna integrated photonic chip to encode and up-convert mm-Wave radiation to the optical regime. An array of these mm-Wave sensors is strategically spaced to form a staring configuration and form an interferometric sparse array as in Figure 6-1. The back end of the mm-Wave array makes use of an off-the-self Near-IR camera. This innovative passive mmWave imaging camera is expected to have an unprecedented low form factor, very high spatial contrast, high sensitivity, and functions at real time video rate.

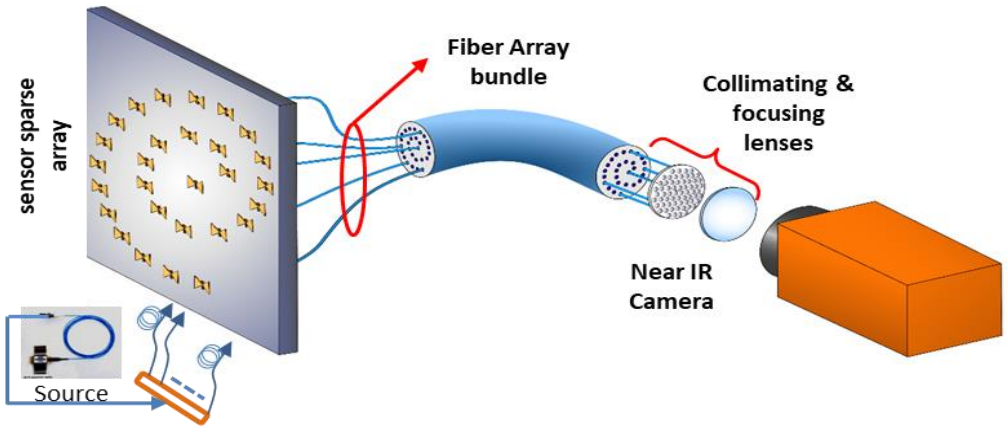

Figure 6-1. Schematic of the envisioned sparse optical up-conversion and sensing

The effort in this dissertation focused on the successful integration of aperture sensors and imaging technologies to achieve remote and passive sensing at millimeter waves (94 GHz) using a small form factor camera. Already, we have made several design and fabrication steps to remove potential risks in realizing the proposed imaging camera system.

The subject passive mm-Wave radiation from the body or target will be encoded onto an optical signal for post-processing, followed by image capture as done by IR cameras. At the front-end of the proposed camera system, is a unique architecture that introduces an integrated photonic chip to encode and up-convert the received mm-Wave radiation onto the optical regime. As shown, a small array of these mm-Wave sensors will be strategically spaced to form a staring configuration as in Figure 6-1.. The back end of the mm-Wave array of sensors makes use of an off-the-self Near-IR (NIR) camera. This innovative passive mm-Wave imaging camera is expected to have an unprecedented low form factor, very high spatial contrast, high sensitivity, and functions at video rate.

Notably, past efforts to realize this class of small-factor mm-Wave cameras have failed due to low efficiency antenna to optical/IR signal transition. By contrast, recent innovations by the proposers have allowed for 1000-fold efficiency improvements (see Figure 6-2). As such, the proposed mm-Wave camera can operate in passive mode, viz. no active millimeter wave illumination is needed, and without a need for LNAs to amplify the received millimeter wave signals. Another important development brought forward is the newly available electro-optical modulator (EOM) nonlinear polymer material. This material is crucial for transitioning the millimeter wave/RF signal into optical form for projection onto a standard IR camera. In the past, Lithium Niobate was used for EOM devices, but these were limited to 40 GHz operation at best. Herewith, we propose a new class of electrooptical polymers with a 10-times larger electro-optic coefficient and operation at frequencies surpassing 110 GHz. The operational design frequency is 94 GHz (available and approved FCC band).

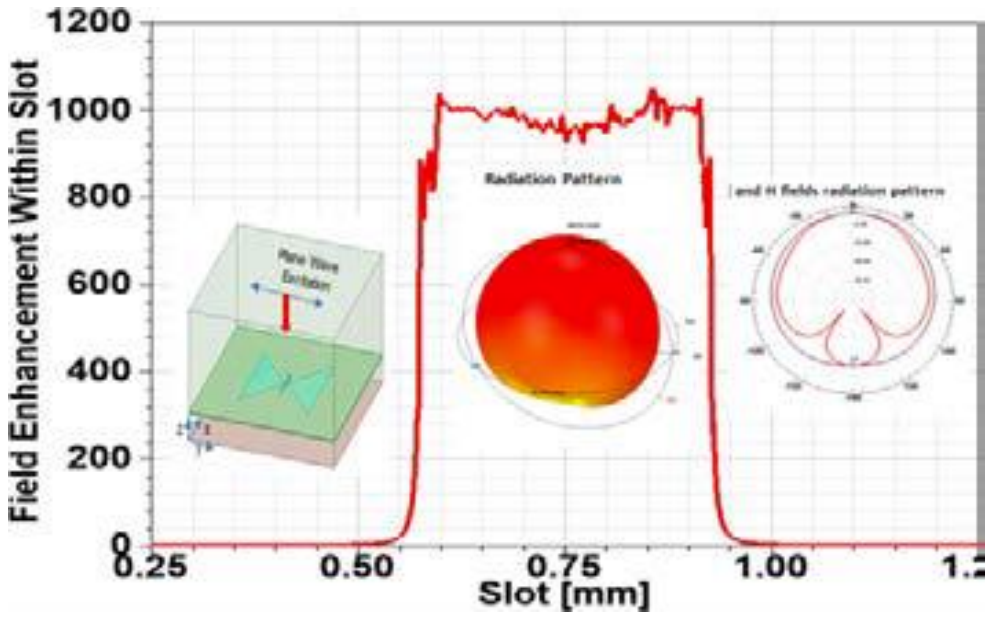

Figure 6-2. 1000-fold higher field enhancement strength in received millimeter wave signal. This is key to the realization of the passive mm-Wave camera without LNAs and in a small form factor.

As noted above, the scope of this research effort is to mitigate and overcome existing issues of passive millimeter wave imaging systems using optical up-conversion. Issues that are addressed include acceptable performance for passive operation, form factor, and cost. Solving these issues will bring forward a remarkable innovation needed to exploit the high utility and potential of mm-Wave cameras at all sorts of security applications and venues, scientific, communication, and medical applications. Figure 6-3 depicts an analysis and the expanded camera system. The analysis confidently shows that the achieved 1000-fold field enhancement at the antenna stage with the integrated EOM, would yield 10-times higher value than the minimum needed currents to drive a standard NIR detector. This implies a reliable operation of the integrated near-IR imaging camera.

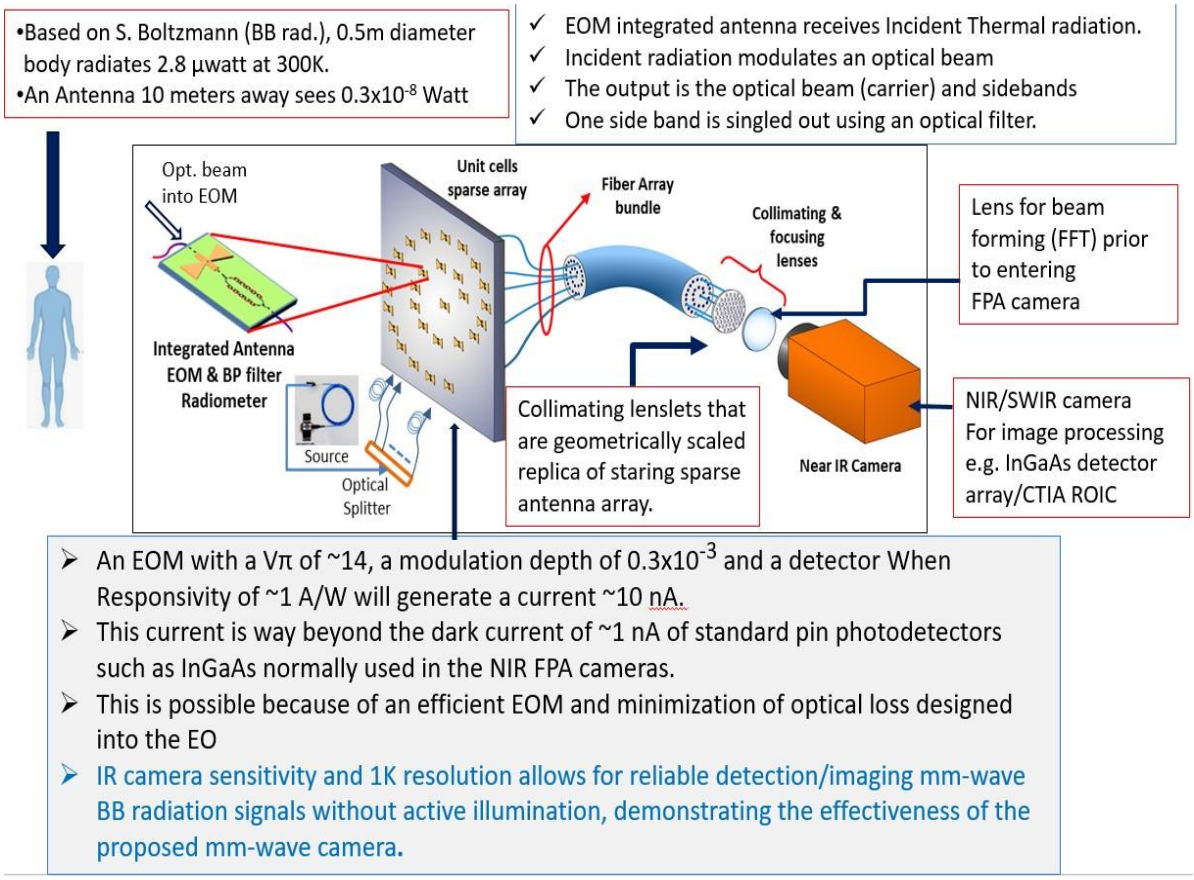

Figure 6-3. Schematic depiction of the mm-Wave camera operation with associated detection analysis

Figure 6-3 depict the schematic diagram of the proposed camera system. It integrates 3 different major components: 1) high gain antenna elements to form a starring array for passive millimeter wave collection; 2) integrated EOM to efficiently transition the millimeter wave/RF fields into optical/IR signals. The combined antenna and EOM with optical transitions will form the on-chip realization of the antenna array elements; 3) back-end collimation of the optical fields to project them onto the low cost Near-IR camera.

Several key challenges have already been carried in realizing the proposed mm-Wave camera, that include:

- Development of optimal antenna design and determined the EOM topology/architecture for a realizable microfabrication process. Also, new EO materials were identified. Specifically, Epocore and Epoclad will be used for the core polymer region and cladding, respectively, to realize the necessary Pockels effect needed to efficiently transition the RF signal to optical.
- Reduced noise at the back end, using low loss optical fibers and dispersion-free routing of the up-converted image to the near-IR optical lens and camera.
- Carried out overall system performance analysis and demonstrated operation of the proposed mm-Wave camera system with 10-fold margin at the passive operational mode.
- Design and establishment of the microfabrication process for on-Chip antenna using several standard lithography steps.

6.1 FUTURE WORK

The critical portion of the PMMW imaging camera system described in this is mainly the front-end single unit radiometric detector. Namely the photonic antenna integrated electro-optic modulator performing the optical up-conversion. As it determines the sensitivity performance of the overall system. Although, the rest of the system is not without challenges, these are engineering addressable hurtles. Passive and active polymeric optical devices have been proven to have high speed, low dielectric dispersion, and high electro-optic coefficients, nonlinear polymers designed for active devices such as EO modulators have several drawbacks that will influence the sensitivity of the proposed imaging system: they have inherently higher optical propagation loss, larger coupling losses

between optical fiber and waveguide due to mode overlap factor, and can be susceptible to photochemical reactions that may reduce stability. To address these limitations, optimize sensitivity, and take full advantage of the electro-optical properties of EO polymers, we will use a sol-gel silica/polymer hybrid approach, where sol-gel silica is utilized for all passive optical wave guides and devices and the surrounding claddings, and the nonlinear EO polymer is used only in the active portions of the EO modulator. The fabrication process requires the development of the materials processing for the system to ensure proper materials properties, integration capabilities of different materials, and fabrication flexibility to accommodate changes in design can be improved to further the sensitivity, speed, and cost. The three classes of materials that could be used are the sol-gel silica system for the optical transmission components, the patterned gold deposition for the antenna electrodes, and the EO polymer patterning and poling for the modulator.

Future work for potential performance improvement could address the fabrication of the integrated antenna/EO modulator/ filter front-end system for the camera will consist of the passive optical sol-gel silica component fabrication, 3D patterning of the EO polymer, deposition of the antenna metal, encapsulating the EO polymer and antenna in the cladding sol-gel silica, and poling the EO polymer. All the materials processing should occur at relatively low temperatures (all <160 ˚C) and relatively benign chemical conditions that will not damage previously deposited materials. Patterning of both the EO polymer and the silica waveguide core could be done using microstamping. Microstamping provides 3D patterns with sidewalls as smooth as the mold used, either photolithographically defined patterns or micromachined polymers, which can be further smoothed via thermal softening prior to molding if needed..

Both the sol-gel silica waveguide core and the EO polymer should be patterned using micro-molding. The desired 3D micro-geometry will be patterned using standard UV photolithography or micro-milling for 3D features. A glass substrate can be coated with a thin layer of the cladding sol-gel silica by spin coating. The core sol-gel silica would be patterned on this cladding layer using micro-molding. A layer of cladding silica will be deposited around the core silica via spin-coating, and any film over the core will be removed using a fluorine-based plasma etch, followed by a hard bake for all the deposited layers. A titanium (20 nm)/ gold (50 nm) seed layer can be deposited using lift-off patterning and sputter coating.

The EO polymer can then be deposited using micro-molding over the core silica in just the active area of the pixel. The electrode seed layer will then be connected to electrodes and used to electrodeposit the gold antenna pattern, which also acts as the electrode for poling the EO polymer. The antenna should be characterized to ensure smooth, dense gold deposition in the desired pattern. Another layer of cladding silica is deposited to encapsulate the EO polymer and can be planarized with fluorine plasma down to the electrodes for an electrical connection for poling.

BIBLIOGRAPHY

[1] L. Yujiri, M. Shoucri and P. Moffa, "Passive millimeter wave imaging," in IEEE Microwave Magazine, vol. 4, no. 3, pp. 39-50, Sept. 2003

[2] J. Preissner, “The influence of the atmosphere on passive radiometric measurements,” Symp. Millimeter Submillimeter Wave Propag. Circuits: AGARD Conf. Proc., no. 245, pp. 48/1-48/13.

[3] Appleby, Roger & Robertson, Duncan & Wikner, David. (2017). Millimeter wave imaging: a historical review. 1018902. 10.1117/12.2262476.

[4] Stephan Dill, Markus Peichl, Helmut Süß, "Study of passive MMW personnel imaging with respect to suspicious and common concealed objects for security applications," Proc. SPIE 7117, Millimetre Wave and Terahertz Sensors and Technology, 71170C (2 October 2008)

[5] S. S. Ahmed, A. Schiessl and L. -P. Schmidt, "A Novel Fully Electronic Active Real-Time Imager Based on a Planar Multistatic Sparse Array," in IEEE Transactions on Microwave Theory and Techniques, vol. 59, no. 12, pp. 3567-3576, Dec. 2011

[6] D. M. Sheen, D. L. McMakin, T. E. Hall and R. H. Severtsen, "Active millimeter-wave standoff and portal imaging techniques for personnel screening," 2009 IEEE Conference on Technologies for Homeland Security, Waltham, MA, USA, 2009, pp. 440-447

[7] F.T. Ulaby and K.R. Carver, “Passive microwave radiometry,” in Manual of Remote Sensing, R.N. Colwell, Ed. Falls Church, VA: American Society of Photogrammetry, 1983, ch. 11, pp. 475-516.

[8] P. Bhartia and I.J. Bahl, Millimeter Wave Engineering and Applications. New York: Wiley, 1984, pp.

[9] D.D. King, “Passive detection,” in Radar Handbook, M.I. Skolnik, Ed. New York: McGraw-Hill, 1970, ch. 39, pp. 39-1 to 39-36.

[10] Lei Zhou; Chun-Cheng Wang; Zhiming Chen; Heydari, P., "A W-band CMOS Receiver Chipset for Millimeter-Wave Radiometer Systems," Solid-State Circuits, IEEE Journal of , vol.46, no.2, pp.378,391, Feb. 2011

[11] Dacquay, E.; Tomkins, A.; Yau, K.H.K.; Laskin, E.; Chevalier, P.; Chantre, A.; Sautreuil, B.; Voinigescu, S.P., " D -Band Total Power Radiometer Performance Optimization in an SiGe HBT Technology," Microwave Theory and Techniques, IEEE Transactions on , vol.60, no.3, pp.813,826, March 2012

[12] Ojefors, E.; Pfeiffer, U., "A 94-GHz Monolithic Front-End for Imaging Arrays in SiGe:C Technology," Microwave Integrated Circuit Conference, 2008. EuMIC 2008. European, vol., no., pp.422,425, 27-28 Oct. 2008

[12] Gilreath, L.; Jain, V.; Heydari, P., "Design and Analysis of a W-Band SiGe Direct-Detection-Based Passive Imaging Receiver," Solid-State Circuits, IEEE Journal of , vol.46, no.10, pp.2240,2252, Oct. 2011

[14] Macario, J.; Peng Yao; Shireen, R.; Schuetz, C.A.; Shouyuan Shi; Prather, D.W., "Development of Electro-Optic Phase Modulator for 94 GHz Imaging system," Lightwave Technology, Journal of , vol.27, no.24, pp.5698,5703, Dec.15, 2009

[15] C. A. Schuetz, J. Murakowski, G. J. Schneider, and D. W. Prather, "Radiometric millimeter-wave detection via optical upconversion and carrier suppression," IEEE Trans. Microw. Theory Tech., vol. 53, no. 5, pp. 1732–1738, May 2005.

[16] C. A. Schuetz, C. Huang, R. Shireen, T. H. Hwang, G. J. Schneider, J. Murakowski, and D. W. Prather, "Electro-optic modulator optimization for optically-based passive millimeter-wave detection," in Terahertz Gigahertz Electron. Photon. V, Proc. SPIE. Bellingham, WA: International Society for Optical Engineering, Jan. 25–26, 2006, vol. 6120, pp. 612007-1–612007-10.

[17] C. J. Huang, C. A. Schuetz, R. Shireen, S. Shi, and D. W. Prather, "LiNbO3 optical modulator for MMW sensing and imaging," in Proc. SPIE. DSS, 2007, art. 65480I.

[18] C. A. Schuetz and D. W. Prather, , R. Appleby, J.M. Chamberlain, and K. A. Krapels, Eds., "Optical upconversion techniques for high sensitivity millimeter-wave detection," in Passive Millimeter-Wave Terahertz Imaging Technol. SPIE, London, England: , 2004, vol. 5619, pp. 166–174.

[19] J. P. Samluk, C. A. Schuetz, E. L. Stein Jr., A. Robbins, D. G. Mackrides, R. D. Martin, C. Chen, and D. W. Prather, "Far field millimeter-wave imaging via optical upconversion," in Proc. SPIE, 2008, vol. 6948, pp. 694804-1–694804-10.

[20] J. P. Samluk, C. A. Schuetz, R. D. Martin, E. L. Stein Jr., D. G. Mackrides, C. Chen, P. Yao, R. Shireen, J. Macario, and D. W. Prather, "94 GHz millimeter-wave imaging system implementing optical upconversion," in Proc. SPIE, 2008, vol. 7117, p. 711729.

[21] Macario, J.; Peng Yao; Shireen, R.; Schuetz, C.A.; Shouyuan Shi; Prather, D.W., "Development of Electro-Optic Phase Modulator for 94 GHz Imaging system," Lightwave Technology, Journal of , vol.27, no.24, pp.5698,5703, Dec.15, 2009

[22] Mallari, J.; Cailin Wei; Dan Jin; Guomin Yu; Barklund, A.; Miller, E.; O'Mathuna, P.; Dinu, R.; Motafakker-Fard, A.; Jalali, B., "100Gbps EO polymer modulator product and its characterization using a real-time digitizer," Optical Fiber Communication (OFC), collocated National Fiber Optic Engineers Conference, 2010 Conference on (OFC/NFOEC) , vol., no., pp.1,3, 21-25 March 2010

[23] S.K. Kim; H. Zhang; D.H. Chang; C. Zhang; C. Wang; W.H. Steier; H.R. Fetterman, "Electrooptic polymer modulators with an inverted-rib waveguide structure, " IEEE Photonics Technology Letters, Vol. 15, Issue 2, 2003, Pages 218 – 220

[24] R. Dinu, D. Jin; G. Yu; B. Chen; D. Huang; H. Chen, A. Barklund, E. Miller, C. Wei, J. Vemagiri, "Environmental Stress Testing of Electro-Optic Polymer Modulators, " Lightwave Technology, Vol 27, Issue 11, 2009, pp 1527-1532

[25] A. Willner and S. R. Nuccio, "Electro-Optic Polymer Modulators," in Optical Fiber Communication Conference, OSA Technical Digest (Optical Society of America, 2012), paper OW4F.1.

[26] David L. K. Eng ; Stephen Kozacik ; Benjamin C. Olbricht ; Shouyuan Shi ; Dennis W. Prather; Broadband low-drive voltage polymer electro-optic modulator. Proc. SPIE 8259, RF and Millimeter-Wave Photonics II, 82590C (February 23, 2012)

[27] Sébastien Michel ; Joseph Zyss ; Isabelle Ledoux-Rak ; Chi Thanh Nguyen; High-performance electro-optic modulators realized with a commercial side-chain DR1-PMMA electro-optic copolymer. Proc. SPIE 7599, Organic Photonic Materials and Devices XII, 75990I (March 01, 2010).

[28] Dillon, Thomas & Schuetz, Christopher & Martin, Richard & Shi, Shuoyuan & Mackrides, Daniel & Prather, Dennis. (2010). Passive Millimeter Wave Imaging Using a Distributed Aperture and Optical Upconversion. Proceedings of SPIE - The International Society for Optical Engineering. 7837. 10.1117/12.865081.

[29] Samluk, Jesse & Schuetz, Christopher & Stein, E. & Robbins, Andrew & Martin, Richard & Chen, Caihua & Prather, Dennis. (2008). Far field millimeter-wave imaging via optical upconversion. Proceedings of SPIE - The International Society for Optical Engineering. 10.1117/12.778336.

[30] F. T. Sheehy, W. B. Bridges, and J. H. Schaffner, “60 GHz and 94 GHz antenna coupled LiNbO3 electrooptic modulators,” IEEE Photon. Technol. Lett., vol. 5, no. 3, pp. 307–310, Mar. 1993.

[31] W. B. Bridges, F. T. Sheehy, and J. H. Schaffner, “Wave-coupled LiNbO3 modulator for microwave and millimeter-wave modulation,” IEEE Photon. Technol. Lett., vol. 3, no. 2, pp. 133–135, Feb. 1991.

[32] H. Murata, R. Miyanaka, and Y. Okamura, “Wireless space-divisionmultiplexed signal discrimination device using electro-optic modulator with antenna-coupled electrodes and polarization-reversed structures,” Int. J. Microw. Wireless Technol., vol. 4, pp. 399–405, Apr. 2012.

[33] Y. N. Wijayanto, H. Murata, and Y. Okamura, “Electro-optic wireless millimeter-wave-lightwave signal converters using planar Yagi-Uda array antennas coupled to resonant electrodes,” presented at the Opto-Electron. Commun. Conf., Busan, Korea, Jul. 2012, Paper 5E1-2.

[34] N. Kohmu, H. Murata, and Y. Okamura, “Electro-optic modulators using double antenna-coupled electrodes for radio-over-fiber systems,” IEICE Trans. Electron., vol. E96-C, no. 2, pp. 204–211, Feb. 2013.

[35] A. Yariv, Optical electronics in modern communications, 5th ed. New York: Oxford University Press, 1997.

[36] C. A. Balanis, Antenna Theory, 3rd ed. (Wiley-Interscience, 2005)

[37] EOSPACE Inc. http://www.eospace.com/phase modulator.htm

[38] D. H. Park, V. R. Pagán, T. E. Murphy, J. Luo, A. K.-Y. Jen, and W. N. Herman, "Free space millimeter wave-coupled electro-optic high speed nonlinear polymer phase modulator with in-plane slotted patch antennas," Opt. Express 23, 9464-9476 (2015)

[39] F. T. Sheehy, W. B. Bridges, and J. H. Schaffner, “60 GHz and 94 GHz Antenna-Coupled LiNbO3 Electrooptic Modulators,” IEEE Photon. Technol. Lett. 5(3), 307–310 (1993).

[40] V. R. Pagán, B. M. Haas, and T. E. Murphy, "Linearized electrooptic microwave downconversion using phase modulation and optical filtering," Opt. Express 19(2), 883-895 (2011).

[41] Dan Jin ; Hui Chen ; Anna Barklund ; Jonathan Mallari ; Guomin Yu ; Eric Miller ; Raluca Dinu; EO polymer modulators reliability study. Proc. SPIE 7599, Organic Photonic Materials and Devices XII, 75990H (March 01, 2010)

[42] Dinu, R.; Dan Jin; Guomin Yu; Baoquan Chen; Diyun Huang; Hui Chen; Barklund, A.; Miller, E.; Wei, C.; Vemagiri, J., "Environmental Stress Testing of Electro–Optic Polymer Modulators," *Lightwave Technology, Journal of*, vol.27, no.11, pp.1527,1532, June1, 2009

[43] “Demonstration of 110 GHz electro-optic polymer modulators” Chen, Datong and Fetterman, Harold R. and Chen, Antao and Steier, William H. and Dalton, Larry R.

and Wang, Wenshen and Shi, Yongqiang, Applied Physics Letters, 70, 3335-3337 (1997),

[44] Hybrid cross-linkable polymer/sol-gel waveguide modulators with 0.65V half wave voltage at 1550nm Enami, Y. and Mathine, D. and DeRose, C. T. and Norwood, R. A. and Luo, J. and Jen, A. K.-Y. and Peyghambarian, N., Applied Physics Letters, 91, 093505 (2007)

[45] Richard Martin ; Christopher A. Schuetz ; Thomas E. Dillon ; Caihua Chen ; Jesse Samluk; E. Lee Stein, Jr. ; Mark Mirotznik ; Dennis W. Prather; Design and performance of a distributed aperture millimeter-wave imaging system using optical upconversion. Proc. SPIE 7309, Passive Millimeter-Wave Imaging Technology XII, 730908 (May 05, 2009)

[46] A. Willner and S. R. Nuccio, "Electro-Optic Polymer Modulators," in Optical Fiber Communication Conference, OSA Technical Digest (Optical Society of America, 2012), paper OW4F.1

[47] R. Dinu, D. Jin; et al, "Environmental Stress Testing of Electro-Optic Polymer Modulators," *Lightwave Technology*, Vol 27, Issue 11, 2009, pp 1527-1532.

[48] A.R. Thompson, J.M. Moran & G.W. Swenson, 2001. Interferometry and Synthesis in Radio Astronomy. New York: John Wiley & Sons.

[49] Jian Dong and Qingxia Li (2010). “Antenna Array Design in Aperture Synthesis Radiometers, Microwave and Millimeter Wave Technologies” *Modern UWB antennas and equipment*, Igor Mini (Ed.), InTech,

[50] Pathak, Shibnath, Pieter Dumon, Dries Van Thourhout, and Wim Bogaerts. "Comparison of AWGs and echelle gratings for wavelength division multiplexing on silicon-on-insulator." *IEEE Photonics Journal* 6, no. 5 (2014): 1-9.

[51] Smit, Meint K., and Cor Van Dam. "PHASAR-based WDM-devices: Principles, design and applications." IEEE Journal of selected topics in quantum electronics 2, no. 2 (1996): 236-250.

VITA
ABE AKHIYAT

Born in Agadir, Morocco

2002	MS, Electrical Engineering Florida International University Miami, FL
2019-2023	PhD, Electrical and Computer Engineering Florida International University Miami, FL

PUBLICATIONS AND PRESENTATIONS

A. Akhiyat, Mustafa Karabiyik, and John L.Volakis, “Passive Millimeter-Wave Imaging Toward 1K Resolution,” 2020 IEEE International Symposium on Antennas and Propagation and USNC-URSI Radio Science Meeting, Montreal, CA, 4-10 July 2020 (remotely conducted conference); 2pp page summary.A. Akhiyat and J. L. Volakis, "Planar Millimeter Wave Antenna Design for On-Chip Electro-Optical Sensing Devises” 2021 USNC/URSI National Radio Science Meeting, Virtual, Jan 4-9, 2021.

Abe Akhiyat, Mustafa Karabiyat, and John L.Volakis,“Integrated Planar Antenna with High Field Enhancement for On-Chip Electro-Optical Modulator Design,” 2020 IEEE International Symposium on Antennas and Propagation and USNC-URSI Radio Science Meeting, Montreal, CA, 4-10 July 2020 (remotely conducted conference).

Akhiyat and J.L. Volakis, “High Efficiency Antenna Integrated Electro-Optic modulator for Sensing Applications,” 2021 IEEE International Symposium on Antennas and Propagation and USNC-URSI Radio Science Meeting, Singapore

M. O. Anastasiadis, A. A. Akhiyat, B. Grisafe, D. Pavlidis and J. L. Volakis, "GaN/AlGaN Solid-State Traveling-Wave Amplifier (SSTWA) Operating at W -Band," in IEEE Microwave and Wireless Technology Letters, doi: 10.1109/LMWT.2023.3265353.

Maxence Carvalho, Abe Akhiyat, Elias A. Alwan, John L. Volakis, “Directivity Improvement of a 94GHz LTCC Integrated Pyramidal Horn Antenna Using EBG Structure” 2019 International Workshop on Antenna Technology (iWAT), Miami, FL, Mar. 04, 2019.

S. Bojja Venkatakrishnan; A. Akhiyat; E. A. Alwan; J. L. Volakis, "Multi-band and Multi-beam Direction of Arrival Estimation using On-Site Coding Digital Beamformer," in *IEEE Antennas and Wireless Propagation Letters* ,2017, vol.PP, no.99

E. A. Alwan, A. A. Akhiyat, W. Khalil, and J. L. Volakis, Analytical and Experimental Evaluation of a Novel Wideband Digital Beamformer with On-Site Coding, Journal of Electromagnetic Waves and Applications, vol. 28, no. 12, pp. 14011429, Aug. 2014.

E. A. Alwan, S.B. Venkatakrishnan, A. A. Akhiyat, W. Khalil, J.L. Volakis, Phase Error Evaluation in a Two-Path Receiver Front-End With On-Site Coding, IEEE Access, vol.3, no., pp.55,63, 2015

Elias A. Alwan, Abe A. Akhiyat, Waleed Khalil, John L. Volakis, Analytical and Experimental Evaluation of a Novel Wideband Transceiver with On-Site Coding, 2014 National Radio Science Meeting (USNC/URSI), Boulder, Co, Jan. 2013

Satheesh Bojja Venkatakrishnan, Abe A. Akhiyat, Elias A. Alwan, Waleed Khalil, John L. Volakis, Realization of a Novel On-site Coding Digital Beamformer using FPGAs , 2014 IEEE International Symposium on Antennas and Propagation and USNC-URSI National Radio Science Meeting, July 2014, Memphis, Tennessee

Elias A. Alwan, Abe. A. Akhiyat, Waleed Khalil, John L. Volakis, Phase Characterization of a 2-Path On-site Coding Digital Beamformer, 2014 IEEE International Symposium on Antennas and Propagation and USNC-URSI National Radio Science Meeting, July 2014, Memphis, Tennessee

Kiourti, A.; Lee, C.; Akhiyat, A.; Volakis, J.L.; Schwerdt, H.; Chae, J., "Passive, on chip and in situ detection of neuropotentials," *Antennas and Propagation Society International Symposium (APSURSI), 2014 IEEE* , vol., no., pp.1923,1923, 6-11 July 2014

R. Berenguer, G. Liu, A. Akhiyat, K. Kamtikar, Y. Xu, "Optimization and macromodeling of single-ended sub-nH MCPW based inductors for a 77GHz LNA in 65nm CMOS," in *Design of Circuits and Integrated Systems (DCIS) Conference,* Lanzarote, Spain, Nov. 2010.

R. Berenguer, G. Liu, A. Akhiyat, K. Kamtikar, Y. Xu, "A 43.5mW 77GHz Receiver Front-End in 65nm CMOS suitable for FM-CW Automotive Radar," in *Proc. IEEE Int. Custom Integrated Circuits Conf. (CICC)*, 2010.

R. Berenguer, G. Liu, A. Akhiyat, K. Kamtikar, Y. Xu, "A 117mW 77GHz Receiver Front End in 65nm CMOS with Ladder Structured Tunable VCO," in Proc. Eur. Solid-State Circuits Conf. (ESSCIRC), Sep. 2010, pp. 494-497.

G. Liu, R. Berenguer, A. Akhiyat, K. Kamtikar, Y. Xu, "Configurable MCPW Based Inductor for mm-Wave Circuits and Systems," in Proc. IEEE Int. Symp. Circuits Systems (ISCAS), May, 2010, pp. 1113-1116.